
Extreme, long duration, lower tropospheric
wintertime temperature anomalies over Eastern
China and their relationship to the large-scale
circulation

by

Simran Kaur Raju

A thesis submitted in partial fulfilment of
the requirements for the degree of

MASTER OF SCIENCE

(Atmospheric and Oceanic Sciences)

at the

UNIVERSITY OF WISCONSIN-MADISON

2017

Thesis Declaration and Approval

I, Simran K. Raju, declare that this thesis titled ‘Extreme, long duration, lower tropospheric wintertime temperature anomalies over Eastern China and their relationship to the large-scale circulation’ and the work presented in it are my own.

Simran K. Raju

Author

Signature

Date

I hereby approve and recommend for acceptance this work in partial fulfillment of the requirements for the degree of Master of Science:

Jonathan E. Martin

Committee Chair

Signature

Date

Michael Morgan

Committee Member

Signature

Date

Daniel Vimont

Committee Member

Signature

Date

Abstract

A recent analysis of wintertime lower tropospheric temperatures from reanalysis data has revealed a systematic shrinking of the areal extent of air colder than -5°C at 850-hPa over the Northern Hemisphere (Martin 2015). A component of that analysis considered the relationship between the time series of the hemispheric extent of the cold pool and the 850-hPa temperature at all grid points in the Northern Hemisphere. Throughout the winter (DJF), these correlations were largest in eastern China suggesting a relationship exists between cold surges of the East Asian Winter Monsoon (EAWM) and the hemispheric extent of the cold air.

In order to further investigate this apparent connection, the present analysis considers two new indices representative of EAWM; temperatures in eastern China and the Siberian-Mongolian High. In particular, the time series of 850-hPa daily temperature anomalies in eastern China (25°N , 102.5°E to 45°N , 122.5°E) (CI index) and the areal extent anomalies of the 256 meter 1000-hPa height (1032mb equivalent) (SMH index) over 65 winter seasons (NDJFM, 1948/49 – 2012/13) using the NCEP-NCAR Reanalysis data are examined. From the CI index, 1.5σ cold and warm days are identified which further allowed for the identification of long duration, extreme EAWM events. Composites of the onset and decay period for 29 and 34 long duration extreme cold and warm events, respectively, are made from three indices (HCP, SMH, CI) and anomalies of four atmospheric variables (200-hPa zonal wind, 500-hPa geopotential heights, sea-level pressure, 850-hPa temperatures) in order to reveal characteristic structures and synoptic evolutions associated with each.

The analysis reveals significant daily correlations (CI & SMH: -0.42; CI & HCP: -0.51; SMH & HCP: 0.46) and seasonal correlations (CI & SMH: -0.62; CI & HCP: -0.75; SMH &

HCP: 0.59) between all three indices with the CI and HCP having the strongest relationship; suggesting, as in Martin (2015), that eastern China's winter temperatures bear an unusually intimate relationship to the areal extent of the HCP. The spatial composites display distinctive synoptic structures. During the onset of cold events, the East Asian Jet (EAJ) has a tendency to retract toward eastern China, the 500-hPa height anomalies reveal a positive Eurasian pattern (EU), a shift and strengthening of the SMH is seen over eastern Asia, and as a result, a strong cold anomaly migrates into eastern China. During the decay of cold events, the East Asian Jet (EAJ) has a tendency to extend back toward the central Pacific while every other variable relaxes back to average. During the onset of warm events, the East Asian Jet (EAJ) has a tendency to extend toward the central Pacific, the 500-hPa height anomalies reveal a negative Eurasian pattern (EU), negative SLP anomalies indicate a weakened SMH, and a warm anomaly is present in eastern China. The decay of warm events is characterized by a relaxation to average in all four atmospheric variables over Asia.

“Science is more than a body of knowledge. It’s a way of thinking, a way of skeptically interrogating the universe with a fine understanding of human fallibility.”

Carl Sagan (1996)

Acknowledgment

I would like to first thank my undergraduate advisor, Eric Snodgrass from the University of Illinois at Urbana-Champaign, for encouraging me to pursue a master's degree in Atmospheric Sciences. When I was confused as to what path I should take after my bachelor's, he was able to sit down with me and encourage me to push forward with another degree. He always had a way in easing one's stress and confusion. I couldn't have asked for a better undergraduate advisor. From there, I was confident, happy, and excited to continue my education at the University of Wisconsin-Madison.

At UW-Madison, I was fortunate to work with yet another great advisor, Dr. Jonathan Martin. His enthusiasm about weather, climate, research, and teaching is one of a kind and I always had a strong interest in working with him. He has a way of instilling continuous scholarly passion for Atmospheric & Oceanic Sciences. As a teaching assistant under Dr. Jonathan Martin, I was astounded with the way he taught the introduction to weather and climate course. He always has a way of capturing student's attention and making the subject exciting to learn. From there, I continued to grow a strong interest in teaching. Throughout these two years, he has given countless support, invaluable guidance, and ensured my work is at its highest quality. No matter what I chose to do in the future, he was there to listen, support, and encourage my choice. He has taught me many things here and I will always look up to him. I can't thank him enough for his time and giving me the opportunity to work with him.

I would like to express my sincere gratitude to Dr. Daniel Vimont for teaching me everything about statistical analysis and giving me assistance in my research. On top of this, I had a great opportunity to work under him as a teaching assistant. Thank you for all your support

and time. I would also like to thank Dr. Michael Morgan for giving me great ideas with my work and critiquing in order to ensure the best quality. I have learned a great deal from your research and research group.

Teaching has been a big part of my life here at UW-Madison. On top of teaching the Weather and Climate course, I had the honor to work with Margaret Mooney and Steve Ackerman as a teaching assistant for an online course called Climate and Climate Change. I would like to thank them for allowing me this opportunity.

My life at UW-Madison would not be the same without my colleagues and friends in the Department of Atmospheric & Oceanic Sciences. They have always supported my efforts and encouraged my work and plans. Thank you Zachary Handlos, Kyle Griffin, and Melissa Breiden for being enthusiastic with my research, providing me with endless research ideas, helping with code, and supporting my future plans. I would also like to thank my graduate class, especially, Martin's research group, Jessica Taheri, Maria Madsen, and Connor Dacey. We fought through difficult courses together and always supported one another. I couldn't have asked for a better research group and graduate class. I would also like to thank my friends outside of the department and my boyfriend, Harmanjit Singh who has constantly supported me throughout this journey.

Lastly, I would like to dedicate this work to my parents, Baldev and Amrit, and my brothers, Malkeet and Gurveer. Mom and Dad, thank you for never doubting my path to becoming an Atmospheric Scientist and always believing in me. You have taught me that no matter how hard life can get, you have to be strong, patient, and strive for your goals with determination. You both have worked so hard coming to America and to see your children succeed. I can't stress how happy I am to see your proud faces. Your never ending support has

allowed me to achieve my goals and prove to the world that first generations can achieve anything as long as they work hard. Malkeet and Gurveer, thank you for always being excited about my accomplishments and always lifting my spirit. I would not be here without your help and loving support. Having two older brothers isn't bad after all. On top of this, thank you to all my aunts, uncles, and cousins who always supported my path in Atmospheric Sciences and shown me the valuable lessons of life.

Table of Contents

Abstract.....	i
Acknowledgement.....	iii
Table of Contents.....	vii
Abbreviations.....	ix
List of Figures.....	x
List of Tables.....	xvi
1. Introduction.....	1
1.1. Review of Surface and Tropospheric Temperature Trends.....	2
1.2. The Areal Extent of the Wintertime Cold Pool.....	4
1.3. Review of the East Asian Winter Monsoon.....	7
1.3.1. Definition of East Asian Winter Monsoon.....	7
1.3.2. Measuring & Defining East Asian Winter Monsoon.....	8
1.3.3. Variability in East Asian Winter Monsoon.....	10
1.4. Importance of Study.....	13
2. Data and Methodology.....	15
2.1. Data.....	15
2.2. Methodology.....	15
2.2.1. Hemispheric Cold Pool Index.....	15
2.2.2. Cold Intensity Index.....	16
a. Measuring and Defining CI Index.....	16
b. Identifying Extreme Events.....	17
c. Identifying Extended Events.....	18
d. Defining Onset and Decay of Events.....	18
2.2.3. Siberian-Mongolian High Index.....	19
2.2.4. Composite.....	20
3. Results.....	22
3.1. Data & Time Series Analysis of Indices.....	22
3.1.1. Hemispheric Cold Pool Index.....	23
3.1.2. Siberian-Mongolian High Index.....	24
3.1.3. Cold Intensity Index.....	25

3.1.4. Comparison of Indices.....	27
3.2. Extreme & Extended Events.....	30
3.2.1. Extreme & Extended Warm Events.....	31
3.2.2. Extreme & Extended Cold Events.....	32
3.3. Composite Analysis.....	32
3.3.1. Composite: Data Analysis of Cold Events.....	33
a. Onset & Decay of CI Index.....	33
b. Onset & Decay of SMH Index.....	35
c. Onset & Decay of HCP Index.....	37
d. Data Analysis Summary.....	39
3.3.2. Composite: Spatial Analysis of Cold Events.....	40
a. Onset & Decay of U'_{200}	40
b. Onset & Decay of Φ'_{500}	42
c. Onset & Decay of SLP'.....	45
d. Onset & Decay of T'_{850}	46
e. Spatial Analysis Summary.....	47
3.3.3. Composite: Data Analysis of Warm Events.....	48
a. Onset & Decay of CI Index.....	48
b. Onset & Decay of SMH Index.....	50
c. Onset & Decay of HCP Index.....	52
d. Data Analysis Summary.....	53
3.3.4. Composite: Spatial Analysis of Warm Events.....	55
a. Onset & Decay of U'_{200}	55
b. Onset & Decay of Φ'_{500}	57
c. Onset & Decay of SLP'.....	58
d. Onset & Decay of T'_{850}	60
e. Spatial Analysis Summary.....	61
4. Conclusion & Future Work.....	63
5. References.....	67

Abbreviations

HCP	Hemispheric Cold Pool
SMH	Siberian-Mongolian High
CI	Cold Intensity
NCEP–NCAR	National Centers for Environmental Prediction–National Center for Atmospheric Research
EAWM	East Asian Winter Monsoon
AL	Aleutian Low
ENSO	El Nino-Southern Oscillation
AO	Arctic Oscillation
EU	Eurasian Pattern
EAJ	East Asian Jet
EAT	East Asian Trough

List of Figures

Figure 1: Figure 1: Time series of globally averaged tropospheric temperature ($T_{(850-300)}$) for RATPAC (violet) and HadAT2 (green) radiosonde datasets. All time series are 7-month running averages of original monthly data, which were expressed as a departure ($^{\circ}\text{C}$) from the 1979-97 average. (From Karl et al. 2006)

Figure 2: (a) Time series of globally averaged lower tropospheric temperature (T_{2LT}) as follows: UAH (blue) and RSS (red) satellite datasets, and HadAT2 (green) radiosonde data. All time series are 7-month running averages (used as a smoother) of original monthly data, which were expressed as a departure ($^{\circ}\text{C}$) from the 1979-97 average. (b) Same as in (a), but for middle tropospheric temperature (T^*_G). (c) Time series of globally averaged upper tropospheric temperature (T_2) as follows: UAH (blue), RSS (red), and UMd (black) satellite datasets, and HadAT2 (green) radiosonde data. All time series are 7-month running averages (used as a smoother) of original monthly data, which were expressed as a departure ($^{\circ}\text{C}$) from the 1979-97 average. (From Karl et al. 2006)

Figure 3: Smoothed global-mean temperature anomalies from 1958-2009 based on radiosonde and MSU datasets for two layers (top MT; bottom LT). In each panel, the bottom trace is the average of five radiosonde datasets (HadAT, RATPAC, IUK, RAOBCORE, and RICH), and above are differences for individual datasets. Modified from State of the Climate in 2008¹⁹⁴ and courtesy of Carl Mears, Remote Sensing Systems.

Figure 4: Time series of seasonally averaged areal extent of 850-hPa cold pool at five indicated threshold temperatures. Black line with black dots is the 66-yr time series derived from the NCEP reanalysis data. Blue line with blue dots is the 44-yr time series derived from the ERA-40 data. Green line with green dots is the 30-yr time series derived from the NCEP CFSR data. Red lines represent the trend lines (significant at the 99.9% level) calculated using the NCEP reanalysis time series. Orange line with squares is the 30-yr time series of February sea ice extent with magenta line indicating the trend (significant at the 99.9% level). (From Martin 2015)

Figure 5: (a) Blue lines are daily averaged -5°C isotherm on 12 select December days (see text for explanation) when the areal extent of -5°C air was $>2\sigma$ above the 66-yr mean for that day. Thick red lines are the 66-yr daily average -5°C isotherms for those calendar days. (b) As in (a), but for the 11 select days in January. (c) As in (a), but for the 11 select days in February. (From Martin 2015)

Figure 6: (a) Map of correlation between the daily average, December, 850-hPa temperature at each grid point (from 1948 to 2013) in the NCEP reanalysis data to the daily time series of normalized Northern Hemisphere cold pool area for each December day in that interval. Magnitudes of correlations significant at the 95% level are contoured and blue shaded every 0.05 beginning at 0.20. (b) As in (a), but for January days from 1948 to 2014. (c) As in (a), but for February days from 1948 to 2014. (From Martin 2015)

Figure 7: (Top) The 500 hPa geopotential height anomaly field for positive EU phase at lag -6 days (a), lag -5 days (b), lag -3 days (c), lag -2 days (d), lag 0 days (e), lag $+2$ days (f), lag $+3$ days (g), lag $+5$ days (h) and lag $+6$ days (i). *Solid contours* are positive and *dashed contours* are negative. The contour interval is 30 m. *Light* and *heavy shadings* indicate significant variation above 95 and 99 % confidence level, respectively. (From Wang and Zhang 2015)

Figure 8: The 500 hPa geopotential height anomaly field for negative EU phase at lag -6 days (a), lag -5 days (b), lag -3 days (c), lag -2 days (d), lag 0 days (e), lag $+2$ days (f), lag $+3$ days (g), lag $+5$ days (h) and lag $+6$ days (i). *Solid contours* are positive and *dashed contours* are negative. The contour interval is 30 m. *Light* and *heavy shadings* indicate significant variation above 95 and 99 % confidence level, respectively. (From Wang and Zhang 2015)

Figure 9: Highlighted in blue is the SMH index area. ‘H’ illustrates the SMH with each threshold pressure on 12Z - Jan. 8th, 1955. Highlighted in pink is the CI index area.

Figure 10: Cumulative distribution function of the duration of extreme warm (red) and cold (blue) events. Black line is drawn to indicate the chosen length criteria of 4 days or greater which represent the 66th (57th) percentile of extreme cold (warm) days.

Figure 11: Data distribution of daily standardized anomalies for the HCP index from Nov. 1948 – Mar. 2013. See text for boxplot explanation.

Figure 12: Time series of seasonal averaged HCP anomalies from Nov. 1948 – Mar. 2013. Dashed orange lines represent ± 1.5 standard deviations from the average. Black dashed line represents the linear trend of the time series.

Figure 13: Data distribution of daily standardized anomalies for the SMH index from Nov. 1948 – Mar. 2013. See text for boxplot explanation.

Figure 14: Time series of seasonal averaged SMH anomalies from Nov. 1948 – Mar. 2013. Dashed orange lines represent ± 1.5 standard deviations from the average. Black dashed line represents the linear trend of the time series.

Figure 15: Data distribution of daily standardized anomalies for the CI index from Nov. 1948 – Mar. 2013. See text for boxplot explanation.

Figure 16: Time series of seasonal averaged CI anomalies from Nov. 1948 – Mar. 2013. Dashed orange lines represent ± 1.5 standard deviations from the average. Black dashed line represents the linear trend of the time series.

Figure 17: Scatterplot of daily standardized anomalies for the SMH and CI indices.

Figure 18: Scatterplot of daily standardized anomalies for the HCP and CI indices.

Figure 19: Scatterplot of daily standardized anomalies for the SMH and HCP indices.

Figure 20: Time series of seasonal averaged CI (blue) and SMH (red) anomalies from Nov. 1948 – Mar. 2013. Correlation coefficient is indicated in italicized black (significant at the 99% confidence level).

Figure 21: Time series of seasonal averaged CI (blue) and HCP (green) anomalies from Nov. 1948 – Mar. 2013. Correlation coefficient is indicated in italicized black (significant at the 99% confidence level).

Figure 22: Time series of seasonal averaged HCP (green) and SMH (red) anomalies from Nov. 1948 – Mar. 2013. Correlation coefficient is indicated in italicized black (significant at the 99% confidence level).

Figure 23: Composite of 29 extreme and extended cold events. (a) Data distribution of the onset period for the CI index. (b) As for Fig. 23a, but for the decay period.

Figure 24: Composite of 29 extreme and extended cold events. (a) Time series of the onset period for the CI index. (b) As for Fig. 24a but for the decay period.

Figure 25: Composite of 29 extreme and extended cold events. (a) Data distribution of the onset period for the SMH index. (b) As for Fig. 25a but for the decay period.

Figure 26: Composite of 29 extreme and extended cold events. (a) Time series of the onset period for the SMH index. (b) As for Fig. 26a but for the decay period.

Figure 27: Composite of 29 extreme and extended cold events. (a) Data distribution of the onset period for the HCP index. (b) As for Fig. 27a but for the decay period.

Figure 28: Composite of 29 extreme and extended cold events. (a) Time series of the onset period for the HCP index. (b) As for Fig. 28a but for the decay period.

Figure 29: (a-g) Composite of 200-hPa zonal wind anomalies for each day of the onset period of 29 extreme and extended cold events. (h) Change in magnitude of zonal wind anomalies from day -5 to day 0. Red contours represent the 95% confidence level.

Figure 30: (a-g) Composite of 200-hPa zonal wind anomalies for each day of the decay period of 29 extreme and extended cold events. (h) Change in magnitude of zonal wind anomalies from day 0 to day +5. Red contours represent the 95% confidence level.

Figure 31: As for Fig. 29, but for composite of 500-hPa height anomalies.

Figure 32: As for Fig. 30, but for composite of 500-hPa height anomalies.

Figure 33: As for Fig. 29, but for composite of sea-level pressure anomalies.

Figure 34: As for Fig. 30, but for composite of sea-level pressure anomalies.

Figure 35: As for Fig. 29, but for composite 850-hPa temperature anomalies.

Figure 36: As for Fig. 30, but for composite of 850-hPa temperature anomalies.

Figure 37: Composite of 34 extreme and extended warm events. (a) Data distribution of the onset period for the CI index. (b) As for Fig. 37a, but for the decay period.

Figure 38: Composite of 34 extreme and extended warm events. (a) Time series of the onset period for the CI index. (b) As for Fig. 38a but for the decay period.

Figure 39: Composite of 34 extreme and extended warm events. (a) Data distribution of the onset period for the SMH index. (b) As for Fig. 39a, but for the decay period.

Figure 40: Composite of 34 extreme and extended warm events. (a) Time series of the onset period for the SMH index. (b) As for Fig. 40a but for the decay period.

Figure 41: Composite of 34 extreme and extended warm events. (a) Data distribution of the onset period for the HCP index. (b) As for Fig. 41a, but for the decay period.

Figure 42: Composite of 34 extreme and extended warm events. (a) Time series of the onset period for the HCP index. (b) As for Fig. 42a but for the decay period.

Figure 43: (a-g) Composite of 200-hPa zonal wind anomalies for each day of the onset period of 34 extreme and extended warm events. (h) Change in magnitude of zonal wind anomalies from day -5 to day 0. Red contours represent the 95% confidence level.

Figure 44: (a-g) Composite of 200-hPa zonal wind anomalies for each day of the decay period of 34 extreme and extended warm events. (h) Change in magnitude of zonal wind anomalies from day 0 to day +5. Red contours represent the 95% confidence level.

Figure 45: As for Fig. 43, but for composite of 500-hPa height anomalies.

Figure 46: As for Fig. 44, but for composite of 500-hPa height anomalies.

Figure 47: As for Fig. 43, but for composite of sea-level pressure anomalies.

Figure 48: As for Fig. 44, but for composite of sea-level pressure anomalies.

Figure 49: As for Fig. 43, but for composite of 850-hPa temperature anomalies.

Figure 50: As for Fig. 44, but for composite of 850-hPa temperature anomalies.

List of Tables

Table 1: Statistical data distribution of daily standardized anomalies from Nov. 1948 – Mar. 2013 for all three daily indices (HCP, SMH, CI).

Table 2: Statistical data distribution of seasonal averaged standardized anomalies from Nov. 1948 – Mar. 2013 (65 winter seasons) for all three daily indices (HCP, SMH, CI).

Table 3: (a) List of extremely strong EAWM ($+1.5\sigma$) seasons for all three indices (HCP, SMH, CI) as seen from the seasonal averaged time series. (b) List of extremely weak EAWM (-1.5σ) seasons for all three indices (HCP, SMH, CI) as seen from the seasonal averaged time series.

Table 4: Correlation coefficients of daily standardized anomalies from Nov. 1948 – Mar. 2013 for all three indices (HCP, SMH, CI), significant at the 99% confidence level.

Table 5: List of 1.5σ cold events lasting ≥ 4 days. First, second, and third column list their date, length of event, and maximum CI index value, respectively. Highlighted in light blue are the events that had the longest duration of 7 days. Highlighted in dark blue is the event that had the most maximum CI index value (coldest day).

Table 6: Frequency of 1.5σ cold events lasting ≥ 4 days.

Table 7: List of 1.5σ warm events lasting ≥ 4 days. First, second, and third column list their date, length of event, and maximum CI index value, respectively. Highlighted in light red is the event that had the longest duration of 16 days. Highlighted in dark red is the event that had the most maximum CI index value (warmest day).

Table 8: Frequency of 1.5σ warm events lasting ≥ 4 days.

1. Introduction

Interest in climate and climate change began two centuries ago when a French scientist, Joseph Fourier, questioned a rather new theory regarding the physical factors that determine the average temperature of a planet. This deceptively simple question led to speculation concerning the means by which atmospheric composition could affect climate. In 1824, Fourier reasoned that Earth would be significantly colder if it lacked an atmosphere by virtue of the fact that Earth's atmosphere retains heat in the form of radiation (Fourier, 1824). Despite a dearth of well-developed theory at the time, his physical intuition led scientists to further investigate the proposed theory.

In 1859, the English scientist John Tyndall discovered that certain gases in the atmosphere emit and absorb different amounts of longwave infrared radiation which led him to propose that changes in the concentration of these gases could lead to climate change (Tyndall, 1859). This suggestion intrigued a Swedish scientist, Svante Arrhenius, who performed experiments related to Tyndall's proposed theory. Near the turn of the century, he was the first to publish calculations on global warming induced by human emissions of carbon dioxide (CO₂) (Arrhenius, 1896). Though his work was largely ignored by his contemporaries, it was the first spark in a long, smoldering, modern day scientific controversy.

In the 1930s, modern day temperature measurements from stations across eastern North America and western Europe revealed that the global averaged temperatures had increased since the late 19th century. Among those contributing to this conclusion was the English steam engineer, Guy Callendar, whose observations at 200 modern day meteorological stations, led him to suggest the world temperature had increased at an average rate of 0.25°C over the past half century (Callendar, 1938). This claim provoked scientists to look into the question of climate

fluctuations with far better techniques and calculations. With its use of temperature measurements from the meteorological stations across the globe, this study represented one of the first analyses of surface temperature trends that pointed toward a warming Earth. However, questions regarding the reliability of temperature trends detected using *in situ* data led to further increase in research directed at understanding climate variability.

1.1. Review of Surface and Tropospheric Temperature Trends

Analysis of temperature trends has been problematic for nearly a century as a consequence of varying technologies involved in recording observations ranging from surface, radiosonde, and satellite observations as well as reanalysis datasets. Initially, many temperature trends were analyzed by using surface weather station data deployed across the world as stated above. From here, the invention of radiosondes in the early 20th century led to another *in situ* measurement system. It wasn't until the 1970s that satellites began to provide routine remotely sensed observations of atmospheric variables. Although remote sensing is an increasingly important source of atmospheric data, radiosonde observations remain essential to modern meteorology due to their vertical resolution and altitude coverage that cannot be matched by most remote sensing systems. The most recently added long-term data source is objective reanalysis data from numerical weather prediction models. These data are not derived from separate observing systems, but are mathematically blended products produced by combining observations and numerical model output and are invaluable in examining climate and weather statistics (Kalnay et al., 1996). Though concerns about reanalysis data arise due to the occasional unreliability of observed measurements, they, nonetheless, represent a particularly powerful product that can address questions related to the variability of climate and climate change (Karl et al., 2006).

Analyses of the *in situ* and remote measurements from all primary atmospheric datasets, has pointed to a general warming of the planet at the surface and in the lower troposphere (Stocker et al., 2014; Hansen et al., 2001; Lugina et al., 2005; Smith and Reynolds, 2005; Smith et al., 2005; Brohan et al., 2006; Hansen et al., 2010). This conclusion has met with uncertainty as discrepancies between the amount of warming in the upper atmosphere and near the surface has generated skepticism regarding the extent of human induced global warming (Karl et al., 2006). Earlier radiosonde and satellite data indicated little to no warming near the surface while the upper atmosphere showed warming. With advances in historic radiosonde analysis and satellite data, modern reanalysis datasets have revealed a continuous warming of the surface and lower troposphere. Although adjustments to the raw data are complicated and dependent upon expert judgment, it is considered very likely that these estimates give reliable indications of the direction of lower-tropospheric temperature change over the last half-century (Martin, 2015).

In Karl et al. (2006), the temperature trends of the surface, troposphere, and stratosphere were illustrated using four primary datasets: surface, radiosonde, satellites, and reanalysis. In Fig. 1, Karl et al. (2006) illustrated the global averaged tropospheric temperature trend from two radiosonde datasets. It is clear there is an upward trend in the tropospheric temperatures, indicating global warming. When observing the temperature trend using satellite data, similar results were shown. Figure 2 shows the time series of globally averaged temperature trends for lower troposphere, troposphere, and mid-troposphere to lower stratosphere using two satellite datasets. It is seen that in all three of these atmospheric levels there is a general increase in temperatures along with a lot of variability. These datasets demonstrate substantial agreement with temperature trends across the globe since the radiosonde and satellite era (Karl et al., 2006).

Thorne et al. (2010) also reviewed the history of tropospheric temperature trends considering all of the datasets. With multiple dataset revisions and constructing methodologies for new datasets, a more accurate depiction of the lower and mid-tropospheric temperature trend was displayed (Fig. 3). This figure displays the global mean temperature anomalies from 1958 to 2009. It is shown that both the lower and mid-troposphere are warming over time with the lower troposphere warming at a somewhat faster rate. Due to uncertainties in tropospheric data, there is continuous ongoing research to determine which parts of the troposphere and surface have warmed the most. It is evident from previous studies that there is a clear agreement on the warming trend of the surface and troposphere. Studies in the past analyzed numerous *in situ* and satellite datasets to understand the temperature trend, but since the development of reanalysis datasets and with continuous advancements in the products, there have been but a few analyses on temperature trends.

A more recent study by Simmons et al. (2016), along with previous work by Simmons et al. (2014), contributed considerably to the understanding of global averaged temperature trends with the use of two reanalysis datasets. Both of these reanalysis datasets, ERA-Interim and JRA-55, illustrate a global averaged warming trend since 1981. These rather new datasets agree with previous datasets in their depiction of the warming as shown in Simmons et al. (2016). Overall, this study demonstrated that reanalysis datasets are trustworthy tools despite the somewhat complicated manner by which they are constructed.

1.2. The Areal Extent of the Wintertime Cold Pool

This broad warming trend was also revealed in a recent novel analysis of tropospheric temperatures. Employing various reanalysis datasets, Martin (2015) focused on the areal extent of wintertime (December-February) lower tropospheric (850-hPa) air temperatures below a

series of thresholds over the Northern Hemisphere. Next, he constructed daily and seasonal (DJF) averages of these areal extents in order to consider time series of the trends at all thresholds. Figure 4 displays the 66-season time series of the 850-hPa areal extent of five threshold temperatures (-5°C to -25°C at 5°C intervals). The first notable feature in this analysis is that the areal extent of the wintertime cold pool is systematically decreasing at all five threshold temperatures. Essentially, this means that lower tropospheric cold air production is becoming less prolific in the Northern Hemisphere during winter – a clear indication that hemispheric warming is occurring.

Focusing on the -5°C threshold and considering the daily averaged areal extent, Martin (2015) examined aspects of the intra-seasonal variability of the 850-hPa cold pool or the hemispheric cold pool (HCP). By calculating calendar day averages, unusually large and small areal extents of the cold pool (2σ above or below the daily average, respectively) were identified. In order to determine the nature of the HCP that characterizes extreme winter days, an examination of the geographic distribution of -5°C air on extreme cold and warm days was considered. Despite considerable variability, some notably common features are evident in Fig. 5. When the hemisphere is in a 2σ cold event, there is a cold surge in central to eastern China suggesting some sort of relationship between the East Asian Winter Monsoon (EAWM) and hemispheric extreme cold events.

The ubiquity of the central/southern China cold surge, that appears to characterize 2σ cold events in the hemisphere, motivated further analysis (Martin, 2015). Figure 6 shows the correlation maps between the daily average December, January, and February 850-hPa temperature at each grid point (from 20° to 90°N) in the NCEP reanalysis data with the daily time series of standardized Northern Hemisphere 850-hPa -5°C cold pool area. Contoured and

shaded regions show correlations significant at the 95% level (Martin, 2015). The analysis revealed that cold temperatures in central to eastern China are correlated with larger than normal areal extent of the HCP. In other words, when China has cold temperatures, the areal extent of the HCP over the entire Northern Hemisphere tends to be much more larger than normal. The relationship becomes more robust in January and even more so in February. Thus, it is clear there appears to be some relationship between the local temperatures in China and the expansion and contraction of the HCP. It is this result that provides the central motivation for the present work.

Further investigation of this connection is undertaken to examine the physical processes that might underlie a relationship between the temperatures in eastern China and the areal extent of the hemispheric cold pool. It is crucial to get a better understanding of this relationship especially since it exemplifies a possible connection between a large scale phenomenon, HCP, and a rather regional phenomenon, temperatures in eastern China. Several research questions arise for this present study. Why are conditions in eastern China so sensitive to the character of the hemisphere and/or vice versa? What might be learned by examining the synoptic-scale controls on the evolution of lower tropospheric temperatures and other variables in that region? What are the primary physical processes influencing the expansion and contraction of the HCP? Are there both extreme cold and extreme warm events in eastern China during winter and do these events have characteristic persistence? What are the large-scale flow characteristics that lead to extended warm and cold spells in eastern China? Do the characteristics of such events suggest anything about their predictability?

During winter, eastern China's temperatures are dominated by a phenomenon known as the East Asian Winter Monsoon (EAWM); therefore, it is essential to understand the operation of this global-scale circulation feature before diving into its possible connections with other

patterns. Consequently, The East Asian Winter Monsoon (EAWM) is further described in the next section.

1.3. Review of the East Asian Winter Monsoon

The term, “monsoon”, was first used in English during British India, but it has been used in some way for thousands of years. It was mainly used to describe the seasonal reversal of winds and its corresponding precipitation. Research conducted in the past century now refers to the term “monsoon” to describe seasonal changes in atmospheric circulation and precipitation due to difference in heating between the land and sea. Though there are many monsoon systems across the globe, the East Asian Monsoon is a unique and complicated system due to its subtropical location in comparison to all other monsoons which are located in the tropics (Ha et al., 2012). The East Asian Monsoon is thus affected by mid-latitude disturbances. Moreover, the East Asian Winter Monsoon (EAWM) is one of the most active phenomena in the global climate system.

1.3.1. Definition of East Asian Winter Monsoon

During boreal winter, differential heating and the resultant thermally direct circulation are responsible for the EAWM circulation. The maximum heating moves from its boreal summer location over south Asia to the Maritime Continent-northern Australian region. The EAWM has a very large meridional domain. The planetary scale circulation including the East Asian jet Stream (EAJ), East Asian trough (EAT), Siberian-Mongolian High (SMH), Aleutian Low (AL), and convection over the equatorial western Pacific characterizes the three-dimensional winter monsoon circulation (Ha et al., 2012). More specifically, at the heart of the EAWM is the powerful cold-core Siberian-Mongolian high (SMH) typically centered over Lake Baikal in Siberia. The SMH is initially present due to strong radiative cooling induced by the Eurasian

continental snow cover. The SMH generates strong northerly to northwesterly winds, transporting cold air from Siberia into eastern China, the western Pacific, and even the deep tropics. The meridional transport of this cold air is periodic and is commonly referred to as a cold surge. The initiation of a cold surge begins with the intensification of the SMH. A polar jet streak passes west of Lake Balkhash and migrates northeastward over the SMH. The co-location of the entrance region of the jet and the center of the SMH ultimately intensifies the cold-core high at the surface (Chang et al., 2004). With an intensified anticyclone over Siberia and a strong wintertime stationary cyclone in the central North Pacific known as the Aleutian Low (AL), cold air from high-latitude is easily transported to the low-latitudes via meridional winds. These cold surges, as part of the EAWM, can bring drastic temperature drops and explosive cyclones near eastern China due to the temperature contrast between the sea and land. If the intensity of the cold surge is strong enough, it can easily penetrate into the deep tropics affecting maritime convection (Chang and Lau, 1980). With enhanced convection, there is an upper tropospheric meridional return flow which completes the Hadley Cell. Previous studies have found that strong cold surges can lead to an intensification of the Hadley circulation over East Asia (Chang and Lau, 1980; Handlos and Martin, 2016). Given the meridional extent of the EAWM circulation, it is clear that the baroclinic structure of the mid-to-high latitudes can have a strong influence on tropical regions during winter (Chang et al., 2006). A large scale phenomenon like the EAWM can greatly influence other large scale patterns across the globe through its transport of heat, momentum, and water. Due to its importance in the planetary scale circulation, it is vital to assess its connection with other teleconnection patterns in order to assess its possible connection with the hemispheric cold pool.

1.3.2. Measuring & Defining East Asian Winter Monsoon

With such a conspicuous impact on the climate system, it is desirable to quantify the strength of the EAWM and its variability with an appropriate and simple index. Such an index could help to delineate the intra- and inter- annual variability, point toward identifying mechanisms of the EAWM, as well as contribute to monitoring and predicting it in operational climate centers (Wang and Chen, 2013). However, defining the intensity of the EAWM with a simple index has been a difficult task. Wang and Chen (2010) reviewed 18 indices that defined the EAWM in order to assess how well these existing indices represent the phenomenon. They classified the indices into four categories: low-level wind indices (e.g., Wen et al., 2000), upper zonal wind shear indices (e.g., Jhun and Lee, 2004), east–west pressure contrast indices (e.g., Wu and Wang, 2002), and East Asian trough indices (e.g., Sun and Li, 1997) (Wang and Chen, 2013). Many previous indices defined the EAWM using seasonal time scales, entirely inappropriate for the problem to be addressed in this thesis because the heart of the EAWM is the semi-permanent, pulsing SMH, an inherently synoptic feature, which fluctuates from day to day. Therefore, in order to assess the strength of the EAWM, a daily perspective is needed. On top of this, mostly all indices used dynamical variables instead of thermal variables. It has been argued that temperature, though the most impactful meteorological variable in the EAWM does not accurately portray the monsoons comprehensive influence on the climate system due to its inhomogeneous trends over different regions of East Asia (Wang and Ye, 1993; Chen et al., 1991). Therefore, many EAWM investigators have used circulation parameters instead of temperature (Wang and Chen, 2010).

All in all, the use of seasonal indices and dynamical variables to define the EAWM has provided understanding of the circulation. Nonetheless, there has only been one brief study on the daily evolution of the EAWM by examining a case study (Chang et al., 2006) and there has

not been a single EAWM index that strictly uses temperature or temperature anomalies alone to identify the strength of the EAWM. Though there have been several time series of temperature anomalies constructed for China in the 20th century by different groups (Li et al., 2009; Li et al., 2010; Lin et al., 1995; Tang and Ren, 2005; Wang, 1990; Wang et al., 1998; Zhao et al., 2005; Wang et al., 2014), these time series were primarily used to understand the trend of temperature in the past century. Due to a lack of daily temperature indices for the EAWM, this study will primarily focus on a new index using daily temperature anomalies over eastern China in order to estimate the strength of the EAWM. With a daily temperature index defining the EAWM, it is hoped that a better understanding of the relationship between eastern China's temperatures and the HCP can be considered.

1.3.3. Variability in East Asian Winter Monsoon

The EAWM exhibits significant intra-seasonal, inter-annual and inter-decadal variability. Many studies have analyzed and illustrated connections to teleconnection patterns with the above time scales. The inter-annual variability in the EAWM depends on the behavior of the SMH, AL, and the EAJ also known as the subtropical westerly jet. Sakai and Kawamura (2009) demonstrated that atmospheric teleconnection phenomena such as the Pacific/North American (PNA), western Pacific (WP) and Eurasian (EU) patterns may have an important influence on the inter-annual variability in the EAWM, whereas the AO and ENSO may also have an important influence on EAWM behavior. It is widely known that the Arctic Oscillation (AO) has a close relationship with the EAWM intensity on the decadal time scale (Ha et al., 2012). However, it was reported that the intra-seasonal variability in the AO has a significant impact on the EAWM as well (Gong and Ho, 2004).

One particular study by Gong and Ho (2004) showed the intra-seasonal variability of wintertime temperatures has been generally decreasing in northeastern China, implying that the

daily temperatures are not only warming, but are also becoming less variable. It was shown that the intra-seasonal variance of the SMH and AO are significantly correlated with the temperature variance where the seasonal mean state of the AO affects the temperature variance by modulating high-frequency components of the SMH. With the intra-seasonal variance of the SMH declining and the AO strengthening, this contributes to the changes in intra-seasonal temperature variance in East Asia has been affected (Gong and Ho, 2004).

Another relationship on a sub-seasonal and inter-decadal period is the El-Nino Southern Oscillation (ENSO). In some recent studies, ENSO doesn't seem to have a clear connection with the EAWM (Martin, 2015; Ha et al., 2012). Ha et al. (2012) examined strong and weak EAWM years and compared these years to ENSO events to see if there was any relationship. It was shown that the winter monsoon does not closely relate to the ENSO phenomena on an intra-seasonal and inter-decadal period. However, other recent studies by Cheung et al. (2012), He and Wang (2013), and Zhou et al. (2007) indicated that ENSO may have a direct and indirect impact on the strength of the EAWM as well as a long-term correlation with it.

For instance, Cheung et al. (2012) showed evidence suggesting that ENSO phases and the strength of the EAWM are indirectly related. The authors illustrated that ENSO phases directly impact the strength of the AO phase which thus affects the strength of Ural-Siberian blocking. The Ural-Siberian blocking is made up of anticyclonic and cyclonic vortices upstream of the SMH. The strength of the EAWM appears to be modulated by the strength of the blocking. For instance, if the blocking is strong, the SMH strengthens producing cold outbreaks in East Asia. When the AO and ENSO are in phase, greater predictability of EAWM strength is afforded. Specifically, when the AO and ENSO are in their negative phases, there will be greater blocking, producing a stronger SMH, and thus stronger cold surges.

He and Wang (2013) showed evidence suggesting there is a 23-yr sliding correlation between the Niño-3.4 index and the EAWM index revealing an obvious low-frequency oscillation with a period of about 50 years in the ENSO–EAWM relationship. More specifically, they illustrated strong and weak periods of the EAWM-ENSO relationship. It is also suggested and proposed that their relationship has made a recovery and is in its strong period since the early 2000s (He and Wang, 2013). Zhou et al. (2007) also illustrated a low-frequency oscillation and that majority of extreme EAWM events are correlated with the decaying La Niña phase or the development of an El Niño phase. Given these varied results, it is clear that additional observational and modeling work is needed to systematically examine the extent and nature of this relationship.

Parts of the present work focus on the relationship between EAWM events and the Eurasian Pattern (EU). Therefore, it is only reasonable to give a brief background on this pattern. The Eurasian teleconnection pattern is a mode of low-frequency variability in the Northern Hemisphere winter that plays an important role in the EAWM variability, with significant correlation to the Siberian-Mongolia High and temperature anomalies in eastern China (Gong et al., 2001). The EU pattern is measured by observing the 500-hPa height anomalies over the mid-latitude and polar region. The positive phase of the EU pattern is associated with negative height anomalies over the Arctic, north of Europe, and positive height anomalies over Siberia while the negative EU phase exemplifies the opposite. Previous studies have shown that the positive phase of EU pattern is accompanied by an intensified subtropical jet, strong SMH, deepened East Asian Trough (EAT), lower temperature, and less precipitation in east China while the negative EU phase results in a weaker SMH, weakened EAT, and warmer temperatures in East Asia (Gong et al., 2001; Liu and Chen, 2012). The positive EU phase is also referred to as the Ural-Siberian

Blocking. The Ural-Siberian Blocking is also defined in the similar manner as the EU pattern and illustrates the same features. The blocking allows for strong subsidence and thus an enhanced SMH for a prolonged period of time (Cheung et al., 2012).

A recent study by Wang and Zhang (2015) focused on the structure and evolution of the EU pattern at daily time scales since previous studies have mainly focused on a monthly time scale. In their study, a better understanding of the developing and decaying stages of the EU pattern was presented. Figure 7 illustrates the developing and decaying stages of the positive EU phase. At lag 0, a clear wave-train structure is present with positive anomalies over the North Atlantic, negative height anomalies over Scandinavia and Eastern Europe, positive height anomalies over Siberia, and negative height anomalies over Japan. The opposite is seen during the negative phase which is illustrated in Fig. 8. It is widely known that the EU pattern has three centers of action near Scandinavia, Siberia, and Japan. However, the study by Wang and Zhang illustrates a possible fourth center of action in the North Atlantic. They also concluded that the EU phases tend to have a 10-day period. Overall, the EAWM does have some clear connections with other global features on the inter-annual, intra-seasonal, and inter-decadal time scales, but almost no studies have focused on the short term variability of features involved in the EAWM.

1.4. Importance of Study

In general, the present study will focus on many variables that have been examined before; however, different measures are taken to understand their interactions in a way no previous study has yet considered. The daily variability in the intensity of the Siberian-Mongolian High, as well as a measure of the 850-hPa temperature anomaly in the sensitive region of eastern China will be examined using indices to be described in the next chapter. These indices will be compared to the HCP index in order to assess if there is any relationship between

the EAWM and the expansion and contraction of the HCP. Furthermore, from the temperature anomaly index, extreme and extended warm (positive anomalies) and cold (negative anomalies) events will be identified. The daily evolution of these events will be analyzed by focusing on the onset and decay of such events. Compositing the daily structure and evolution of the large-scale circulation within which such events occur will help assess if there is a typical synoptic environment that characterizes their onset and decay. Such information will assist in determining if precursors to such extreme EAWM events can be confidently identified. Further explanation of the indices and the methodology to be employed in this effort is given in the next chapter.

2. Data and Methodology

2.1. Data

The study employs the National Centers for Environmental Prediction–National Center for Atmospheric Research (NCEP–NCAR) reanalysis data (Kalnay et al., 1996). The NCEP–NCAR reanalysis employs relatively large grid spacing ($2.5^\circ \times 2.5^\circ$) and is derived from a frozen state-of-the-art global assimilation system in conjunction with a database that includes in situ and remotely sensed data both at the surface and at levels through the troposphere and stratosphere. In this reanalysis dataset, gridded data are available daily at 0000, 0600, 1200, and 1800 UTC. The present study employs daily averaged data from 65 winter seasons spanning the period 1 November 1948–31 March 2013. The EAWM is normally defined from the months of November through March; therefore, it is appropriate to include these months for wintertime analysis (Ding, 1994; Chang et al., 2006). Five atmospheric variables will be used in this study from the reanalysis data: 850-hPa temperature, 500-hPa and 1000-hPa geopotential heights, sea-level pressure, and 200-hPa zonal wind. The reanalysis data is processed using the General Meteorology Package (GEMPAK) (Koch, 1983) and Matrix Laboratory (MATLAB) operating systems.

2.2. Methodology

In an attempt to assess the physical relationships between the SMH, thermal anomalies in the sensitive region of eastern China, and relations to the HCP, the study analyzes three daily averaged indices constructed from the NCEP-Reanalysis data. Construction of composites of the onset and decay of identified extreme events will provide insight into the nature of these events.

2.2.1. Hemispheric Cold Pool Index

First, the hemispheric cold pool index is considered. The HCP index is defined as the areal extent of the -5°C air at 850-hPa in the Northern Hemisphere. The 850-hPa level is chosen for both the HCP and Cold Intensity (CI) indices, which will be further examined in the next section, as it is high enough to be above the wintertime boundary layer at low elevation locations, but low enough to be safely considered as lower tropospheric (Martin, 2015). The calculation is made by first calculating the area occupied by air colder than -5°C within each grid box and then summing over all grid boxes and is exact at the resolution of the dataset. The specific threshold of -5°C was motivated by two primary considerations:

First, since -5°C at 850-hPa is often a reliable discriminator between liquid and frozen precipitation in mid-latitude winter storms, it is a synoptically familiar and operationally relevant value. Second, -5°C is often embedded within the frontal zones of all but the weakest winter storms and so is subject to substantial deformation by both horizontal and vertical advection. Though such advections may influence the day-to-day variability of the areal extent of such air, neither type of advection can systematically create or destroy cold air. Thus, the fact that -5°C air at 850-hPa often extends deep into the mid-latitudes makes it particularly illustrative of the fact that the expansion or contraction of the 850-hPa cold pool over a long time series testifies to changes in radiative forcing over the same period (Martin, 2015).

2.2.2. Cold Intensity Index

a. Measuring and Defining CI Index

The Cold Intensity (CI) index is a proxy measure of the strength of the EAWM. It is measured by summing all daily 850-hPa temperature perturbations at a select collection of grid points in eastern China and is denoted by $\Sigma T'_{850}$. The analysis domain is a $20^{\circ} \times 20^{\circ}$ box

stretching from 25°N to 45°N and 102.5°E to 122.5°E. The domain is motivated by two primary considerations. First, the typical location of cold surges associated with the EAWM, as referenced by many previous studies, runs through eastern China, parts of the Yellow Sea, and East China Sea (Chang et al., 2006; Chang et al., 2004; Wang and Chen, 2010). Another motivation stems from the fact that the original domain is centered in the region of highest correlation from Martin (2015) (see Fig. 6) and is highlighted in pink shown in Fig. 9. Note that the domain in which the CI index is assessed is located to the southeast of the center of the SMH.

The perturbations or anomalies are calculated by subtracting the actual 850-hPa temperature for a specific day from the calendar day average 850-hPa temperature at every grid point in the domain. The calendar day average, for example, is the average of all November 1st days from years 1948 to 2013. This is done for every single day of all months. After calculating the anomalies at each grid point, all the anomalies are added together in the domain to give a single number which indicates the intensity of cold air ($\Sigma T'_{850}$). Positive and negative perturbations are indicative of warm and cold days, respectively. From here, standardized anomalies are constructed in order to easily compare all three indices together. Due to an uneven data distribution of 5116 warm days and 4699 cold days, separate standardized anomalies are calculated for cold and warm days.

b. Identifying Extreme Events

The CI index, as defined above, gives rise to two separate categories: positive anomalies indicating warmer than normal days and negative anomalies indicating colder than normal days. Next, the extreme warm and extreme cold days are identified. Since the distribution of warm and cold days is non-uniform, calculation of the extremes, require separate consideration of the two types. For all positive values (warm days), separate standard deviations were calculated as well

as for all negative values (cold days). Extreme days were defined as any day on which the $\Sigma T'_{850}$ was 1.5σ or more away from the calendar day average. Thus, extreme cold days had CI values less than or equal to -491.23544 ($\Sigma T'_{850} \leq -491.23544$) while extreme warm days had CI values greater than or equal to 435.00179 ($\Sigma T'_{850} \geq 435.00179$).

c. Identifying Extended Events

Once all the extreme days were found, streaks of consecutive extreme events of each kind could be identified. Figure 10 shows the streak-length distribution of extreme warm and cold days. The most common streak for both species of extreme events is the single day streak. Streaks of 2 or 3 days are also rather common, though decreasingly so. In fact, nearly two-thirds of all extreme days are clustered in streaks that are short-lived, lasting 3 days or less. The remaining one-third of all extreme days are therefore clustered into streaks lasting 4 days or greater. Specifically, there are 436 extreme warm days and 426 extreme cold days in the time series. 66% (57%) of extreme cold (warm) days lasted 3 days or less. The more nearly even split among the total population of warm days is primarily an artifact of an outlier streak that lasted 16 days. Even when the outlier is removed, however, the warm days (40/60 for extended streaks) distribution is still shy of the 2/3 to 1/3 ratio of the cold days. Overall, it is clear that streaks of 4 days or greater are rare in occurrence and thus 4 days serves as a reasonable minimum threshold for establishing an extended criteria. The analysis reveals, there are 29 and 34 wintertime extreme and extended cold and warm events, respectively. The present study will analyze these events with the use of composites constructed in the manner explained and outlined in section 3.4.

d. Defining Onset and Decay of Events

After constructing the CI index and setting two criteria (extreme and extended), isolation of a set of relatively rare, extended warm and cold EAWM events was possible. It was stated previously that the current study will also focus on the daily evolution of our 29 and 34 extreme and extended cold and warm events, respectively. Since the actual streaks are of varying length, it was determined that compositing the several days leading to, and the several days of deterioration away from the extended events themselves was an experimentally simpler, yet still insightful problem.

The onset of such events will be defined as the 5 days prior to the first day of the extended period of thermal anomaly. Hereafter, the onset period will be referred to as Day-5, Day-4, Day-3, Day-2, Day-1, Day0, and Day+1. Day 0 represents the first day on which the given extreme is measured while Day+1 indicates the second day. The decay period is defined as the 5 days following the last day on which the extreme thermal anomaly is measured and will be referred to as Day-1, Day 0, Day+1, Day+2, Day+3, Day+4, and Day+5, where Day-1 indicates the second to last day on which the extreme thermal anomaly is measured.

2.2.3. Siberian-Mongolian High Index

The third and final index that will be examined is the Siberian-Mongolian High (SMH) index. The SMH index is a measure of the strength of the cold-core Siberian-Mongolian High which is strongly correlated with the cold surges that occur in East Asia. In this study, the SMH index is defined in a similar fashion to the HCP index. The index is measured by calculating the daily areal extent of the 1000-hPa geopotential heights greater than 256 meters (1032-hPa equivalent) in the domain of 60°E to 150°E and 20°N to 90°N (blue shaded region in Fig. 9). Once the daily values are calculated for the winter months of 1948 to 2013, they are converted to daily standardized anomalies in a manner similar to that employed with the HCP analysis.

A separate index is created for the SMH in order to assess the relationship between the behavior of this feature and the temperatures in eastern China. Many previous studies have used maximum sea-level pressure to measure the intensity of the SMH which, in turn, is a proxy measure of the strength of the EAWM since the SMH is a primary driver of cold surges in Eastern Asia (Wang and Chen, 2010). Rather than considering just the SLP maximum, this study focuses on the areal extent of high SLPs (1000-hPa $\phi > 256$ meters is equivalent to SLPs > 1032 -hPa) to measure the strength of the SMH. This is mainly motivated by the fact that such a measure is likely a more finely tuned measure of the synoptic variability of the SMH than the simpler analysis of the SLP maximum.

The focus on a threshold of 256 meters (1032 mb equivalent) is due to the fact that the SMH has a climatological mean around 1030 mb. In some cases, the central pressure of the SMH can well exceed 1040 mb, but it is safe to use a height equivalent close to the mean of 1030 mb. Also, the domain chosen carves out an area large enough to assume that the SMH is fully contained within it.

Overall, from the SMH index, we can diagnose when the SMH is strong or weak by looking at the values of the standardized anomalies. The SMH is characterized as strong when the standardized anomalies are positive indicating that the SMH is robust and expansive. The SMH is characterized as weak when the standardized anomalies are negative indicating that the SMH is feeble and contracted.

2.2.4. Composite

In order to better understand the large and synoptic scale evolution of the environment preceding and following extreme and extended EAWM events, an examination of all 3 indices and composites of four atmospheric variables will be constructed corresponding to periods of

onset and decay of the various extended events. The composites of all 3 indices will be examined by statistically analyzing the data using boxplots and time series. The composites of four atmospheric variables, 850-hPa temperature, 500-hPa height, sea-level pressure, and 200-hPa zonal wind, will be examined by geospatially illustrating them.

Composites four atmospheric variables are all constructed in a similar way. By taking all daily values of each variable over the Northern Hemisphere from NCEP-Reanalysis, calendar day averages are calculated and subtracted from the dataset resulting in daily anomalies for all winter months from 1948 to 2013. From here, all the daily anomalies from the corresponding period of onset and decay of the 34 extreme and extended warm events and 29 extreme and extended cold events are extracted. These 34 and 29 daily anomalies are then averaged for each onset and decay day in order to represent a daily evolution of extreme and extended EAWM events which may establish a possible precursor and dissipation stage. On top of this, a close examination of the Eurasian Pattern (EU) will be assessed for all composites as it is closely linked to the strength of the EAWM. A thorough description of the EU pattern will be portrayed in the next chapter.

3. Results

In this chapter, all results and analyses will be presented. The first section presents data and seasonal time series analysis on all three indices (HCP, SMH, and CI). The second section briefly discusses the list of extreme and extended EAWM events. The final section will cover the composite analysis of extreme and extended cold and warm events, defined from the CI index, by analyzing boxplots, time series, and spatial plots.

3.1. Data & Time Series Analysis of Indices

Initially, for each index, an examination of the distribution of data is displayed using boxplots. By examining 65 winter seasons, all indices have 9815 days of data spanning from 1948 to 2013. A boxplot is a simple way of displaying the distribution of data based on the five numerical summaries: minimum, first quartile, median, third quartile, and maximum. The rectangle spans the first quartile to the third quartile indicating 50% of the data is within that box. The box is also known as the interquartile range or IQR. The line segment in the IQR illustrates the median of the data. The line segment or whisker below the box illustrates the ‘inner fence’ which is a value that is 1.5 times the IQR below the first quartile. The whisker above the box also illustrates the inner fence, but above the third quartile. Without outliers, the whiskers would display the maximum and minimum values. In this case, the many outliers displayed in each index are indicated by red marks. Outliers are distinguished when data values are three times the IQR above the third quartile or below the first quartile. It is important to understand that the outliers are not necessarily bad data points especially in large datasets; indeed they often represent the most important and rich part of the dataset.

Secondly, for each index, an examination of seasonal averages of standardized anomalies for 65 winter seasons will be shown using time series. The seasonal averages are calculated by

simply taking all daily values from November to March and averaging them for each year from 1948-2013. This results in 65 data points. For all indices, the plot analyses will state the trend, data statistics, and correlation coefficients.

3.1.1. Hemispheric Cold Pool Index

The HCP index consists of daily standardized anomalies that illustrate the areal extent of the -5°C air at 850-hPa in the Northern Hemisphere. Negative standardized anomalies represent a contraction of the cold pool (warmer days) while positive standardized anomalies represent an expansion of the cold pool (colder days). Figure 11 displays the data distribution of the HCP index. At a quick glance, it appears that the boxplot illustrates a well distributed dataset. Notice that the dataset is balanced near zero. Evidently, the mean in this case is also near zero (actually, exactly 0.0061). Both inner fences are nearly evenly distributed. It is clear that there are a lot of outliers which is normal for a large dataset. There are more outliers displayed below the first quartile, emphasizing more extreme cases of warm days or days when the cold pool is contracted. This is not surprising since one would expect more extreme warm cases due to the fact that there is a warming trend in the time series which will be shown below. At the same time, the data includes months such as November and March where seasonal transitions around the globe can result in more warm than cold days. Other statistical data for the HCP index is shown in Table 1 under the first column.

Figure 12 illustrates the time series of the seasonally averaged standardized anomalies of the HCP index over the past 65 winter seasons. The black dashed line represents the linear trend of the HCP index. The decreasing trend of the HCP index highlights and confirms results from Martin (2015) on the contraction of the HCP over the past 65 years. The slope of the trend line is -0.0073 . Table 2 under the first column lists statistical data such as the mean, maximum,

minimum, range, and standard deviation of the seasonal time series. There are 4 cases below the -1.5σ line and 4 cases above the $+1.5\sigma$ line indicating an even amount of extreme extension and contraction events in the past 65 winter seasons. The 4 extreme extension cases occurred in the season of 50-51, 56-57, 74-75, and 76-77. The 4 extreme contracted cases occurred in the season of 98-99, 01-02, 06-07, and 08-09.

3.1.2. Siberian-Mongolian High Index

The SMH index consists of daily standardized anomalies that illustrate the areal extent of the 1000 mb 256m isoheight line. Negative standardized anomalies represent a contraction of the SMH (small areal extent) while positive standardized anomalies represent an expansion of the SMH (large areal extent). Figure 13 displays the data distribution of the SMH index. The line segment in the IQR depicts a median value to be near zero (0.0024) illustrating a well distributed dataset. Both inner fences are practically evenly distributed. All outliers are located above the third quartile where the standardized anomalies are positive. This indicates the SMH tends to be expansive and robust during winter months. This is no surprise simply due to the fact that in winter months, the SMH becomes prominent due to the snow and ice coverage over Siberia as part of the EAWM; therefore, extreme positive anomalies of the SMH should be seen. More statistical data on the SMH index is presented in Table 1 under column 2.

Figure 14 displays the time series of the seasonally averaged standardized anomalies of the SMH index over the past 65 winter seasons. 4 cases reached above the $+1.5\sigma$ line (winter seasons of 52-53, 54-55, 56-57, and 76-77) and 3 cases reached below the -1.5σ line (72-73, 78-79, and 06-07) indicating a close distribution of extreme extension and contraction of the SMH during those times. The minimum, maximum, mean, range, and standard deviation of the SMH index are listed in Table 2 under column 2. The black trend line illustrates a decreasing trend (-

0.0038) from Nov. 1948 to Mar. 2013, signifying a weakening of the SMH over the past 65 winter seasons. However, it is important to note that the first 10 years of the NCEP- Reanalysis data may be unreliable due to a lack of confidence in compiling the data and it clearly has a substantial influence on the trend line. By removing the first 9 years' worth of data and calculating the trend line, there is a substantial difference. The slope now has a value of -0.0001 which is minuscule compared to the previous stated trend of -0.0038 (see green line in Fig. 14). This result displays quite the opposite conclusions from previous studies. Past studies concluded that the SMH is weakening and becoming warmer since the early 20th century which is consistent with the warming trends over eastern China (Gong, 2002; Tubi, 2012; Xu et al., 2015; Chang et al. 2004; Ha et al., 2012). Some studies even stated that the weakening of the SMH has increased in rate since the mid-1980s. However, keep in mind, the current calculation of the SMH index is different compared to others, therefore, results may differ.

3.1.3. Cold Intensity Index

The CI index consists of daily standardized anomalies that measure the intensity of cold air over a limited portion of eastern China using 850-hPa temperature anomalies. Positive standardized anomalies indicate warmer than normal temperatures while negative standardized anomalies indicate colder than normal temperatures. Figure 15 displays the data distribution of the CI index. The median range is near zero (-1.61×10^{-12}), indicating an evenly distributed dataset. Both inner fences are also virtually evenly distributed. There are many outliers above the third quartile and below the first quartile indicating a common tendency for outliers to occur. The maximum value in the index is 3.4148 and the minimum value is -4.0965. The minimum value is a rather extreme case compared to the warm value. This is most likely the case due to the

tendency of strong cold surges to occur as part of the EAWM. Statistical data of the CI index is listed in Table 1.

Figure 16 displays the seasonal averaged standardized anomalies of the CI index over the past 65 winter seasons (see Table 2 for more statistical data). The time series shows 6 cases in which the temperature anomalies reached below -1.5σ (winter seasons 50-51, 55-56, 56-57, 69-70, and 76-77) and 3 cases above $+1.5\sigma$ (98-99, 01-02, and 06-07, all within the past 20 years). As stated above, more extreme cases of negative temperature anomalies are expected due to the occurrence of cold surges during winter. The years in which the extreme cases occurred reflects a shift to more extreme warm cases and the overall increasing trend line ($+0.0067$) indicates that eastern China has become warmer in the past 65 winter seasons. This is consistent with previous studies that examined temperature trends over eastern China. These studies showed the same warming trend in the region claiming that global warming may be the issue (Wang et al., 2014; Simmons et al., 2016; Li et al., 2009; Li et al., 2010; Lin et al., 1995; Tang and Ren, 2005; Wang, 1990; Wang et al., 1998; Zhao et al., 2005). In fact, because the warming trend is not consistent with the trend of the SMH index from 1957, other aspects of the climate system can be greatly influencing the temperatures in eastern China. Specifically, the substantial warming trend may simply be a result of regional warming instead of seasonal variations in the SMH. However, when observing the SMH trend from 1948, there is a weakening, which ultimately would result in fewer, less vigorous cold surges that characterize winter, thus, suggesting a warming trend over eastern China.

The three seasonal time series demonstrate a close relationship to each other as seen by the extreme (1.5σ) seasons. Tables 3a and 3b list all the extreme winter seasons in which the HCP, SMH, and CI indices occurred as identified by the $\pm 1.5\sigma$ line. Table 3a clearly illustrates

several seasons in which all three indices correspond to each other. For instance, the winter season of 56-57 and 76-77 resulted in an expansive HCP, strong SMH, and thus anomalously cold season in eastern China. The year of 50-51 resulted in an expansive HCP and extreme cold season, but did not result in a strong SMH. Table 3b also lists several seasons in which the indices correspond to each other. The seasons of 98-99 and 01-02 resulted in a contracted HCP and an extreme warm season, but it did not result in an extremely weak SMH. The season of 06-07 however, resulted in a contracted HCP, weak SMH, and a warm season. Overall, it is rather obvious that in order to receive anomalously cold days in eastern China, both the HCP and SMH must be expansive to some extent and to receive anomalously warm days in eastern China, both the areal extent of the HCP and SMH must be small. Overall, there is a clear relationship amongst these indices which can have a great impact on the distribution of cold air during winter. In the next section, an examination of the correlation between all indices is presented using scatterplots and time series.

3.1.4. Comparison of Indices

First, in order to understand the linear dependence of all three indices, an examination of daily standardized anomalies will be presented using scatterplots. Figure 17 shows a scatterplot between the daily standardized anomalies of the CI and SMH indices. The scatterplot is a great representation of the relationship between both these indices. It is clear that when the SMH is robust, there are more cold days, shown by negative standardized anomalies of the CI index. In fact, the correlation coefficient between both indices is -0.4164, significant at the 99% level (Table 4). The negative correlation is consistent with previous studies and the general circulation of the EAWM. Positive SMH values indicate a robust SMH which thus results in efficient meridional transport of cold air to the southern latitudes (negative CI values). When the SMH is

feeble, there tend to be warmer than normal days (positive CI values) due to a weak transport of cold air to eastern China. This correlation may seem relatively low especially since these two variables are closely related through the EAWM, nonetheless, it may be true by expanding the domain of the CI index; a better correlation may exist. This may be true because cold surges also tend to extend through Korea, Japan, and Taiwan when extreme; therefore, in some cases the CI index may not be including such data. On top of this, the dataset is very large and due to a lot of daily variation throughout these 65 winter years, a lower correlation is understandable, though it is still a substantial correlation. The other feature to point out in the scatterplot is the range of the SMH index. As discussed in the boxplot, the SMH only extends from about -2 to 5 because the SMH is prevalent during winter months resulting in more positive standardized anomalies. There are many cases in which the CI and SMH indices do not follow the expected structure of the EAWM, suggesting that other circulations can influence such features. Nevertheless, the dominating aspect of this scatterplot confirms previous studies on the understanding of the features involved in the EAWM.

Figure 18 illustrates a scatterplot of the CI and HCP indices. These indices seem to have a richer relationship. In fact, the correlation coefficient between the CI and HCP indices is -0.5113, significant at the 99% level (Table 4). With an expansive HCP (positive anomalies), there tend to be colder than normal days in eastern China (negative anomalies). When the HCP is contracted (negative anomalies), there tend to be warmer than normal days (positive anomalies) in eastern China. This is a striking feature due to the fact that a comparison is made between the entire Northern Hemisphere and regional temperatures in eastern China. In fact, this is consistent and confirms the correlation maps constructed by Martin (2015) where a rather strong correlation was seen between hemispheric temperatures and regional temperatures in East Asia.

Figure 19 depicts the scatterplot between the SMH and HCP indices. At first glance, the relationship between the two is not as evident as those just presented; however, there is still a correlation of +0.4618, significant at the 99% level (Table 4). This indicates when the HCP is expansive (positive anomalies) so is the SMH and vice versa. Similar to the previous scatterplot, a substantial correlation is made between the Northern Hemisphere and a regional feature. This surprising correlation raises new questions regarding the impact of the SMH on the extension and contraction of the HCP due to such a substantial positive correlation. Overall, it is safe to say there is a clear definite relationship amongst these daily indices with the CI and HCP indices being the most intimate.

Secondly, a further analysis of the relationship between the indices is addressed by calculating the correlation coefficients of the seasonally averaged standardized anomalies, instead of daily data (Table 4). Figure 20 displays a time series of the seasonal averaged standardized anomalies for the CI and SMH indices. The correlation coefficient is -0.6200, significant at the 99% level. This significant negative correlation clearly illustrates a close relationship between the SMH and the temperatures in eastern China. Note the seasonal averaged correlation coefficient is higher compared to the presumably reported daily averaged correlation coefficient (-0.4164). Although, the trends of both indices do not agree, it is evident that both correlate strongly on a seasonal time-scale. Figure 21 depicts a time series of the seasonal averaged standardized anomalies for the CI and HCP indices. Astoundingly, the correlation coefficient is -0.7500, significant at the 99% level. This rather strong negative correlation reiterates how the HCP interacts with regional temperatures in eastern China and why strong correlations were evident in Martin (2015) in similar regions. Moreover, due to such a strong seasonal correlation, the warming trend over eastern China may be resulting in the decreasing

trend of the HCP. With less intense cold air in eastern China, this would ultimately minimize the extension of the HCP due to their strong correlation. Figure 22 displays a time series of the seasonal averaged standardized anomalies for the SMH and HCP indices. Here, we see a positive correlation of 0.5878, significant at the 99% level. The seasonal correlation between the SMH and HCP is lower compared to the two presented previously, similar to the daily correlations. This positive correlation is obviously higher than the daily correlation and it raises a rather intriguing question of whether relatively large-scale features like the SMH can have an impact on the areal extent of the HCP whether directly or indirectly.

There are a couple noteworthy points when observing all three time series together. The winter seasons of 56-57, 76-77, and 08-11 are quite prominent as indicated by the time series. When looking at year 56-57 and 76-77 there is a clear positive correlation with the HCP and SMH and negative correlation with the CI index. During these seasons, the HCP and SMH were well extended and strong, resulting in a cold season. The winter season of 08-11 displays a positive correlation with the HCP and SMH and negative correlation with the CI index. Notice how the HCP is extremely contracted, but the SMH is not as weak. Compared to the two previous winter seasons, the SMH often reached similar anomalies as the HCP, however, during this season, it did not. This may illustrate that the SMH and HCP have a stronger correlation when both are extended and strong, but a feeble relationship when they are both contracted and weak. This could also be a great example of how other possible large-scale features, excluding the SMH, can influence the extension and contraction of the HCP. These seasons and other noticeable years will be discussed further in the next section when examining extreme and extended events identified by the CI index.

3.2. Extreme and Extended Events

After examining the daily values of the CI index, a closer look at extreme and extended warm and cold events from the CI index will now be assessed. Recall when looking at the sum of the temperature perturbations ($\sum T'_{850}$), the extreme criteria for warm and cold events is considered to be any value above 435.002 and any value lower than -491.235, respectively. This translates to a 1.5 standard deviation from the average when considering standardized anomalies. The extended criterion is met when a given event lasts four days or longer. Figure 10 displays the length of all extreme warm and cold events.

The CI index contains of 5135 warm days (positive values) and 4680 cold days (negative values). Moreover, there are a total of 862 extreme days with 436 being warm days and 426 being cold days. 186 of the 436 extreme warm days are involved in 34 extended warm events while 149 of the 426 extreme cold days are grouped into 29 extended cold events. These events are relatively rare and, consequently, it is important to understand the synoptic structure and evolution of such events in order to assess whether their analysis might contribute to enhance predictability of these cases. Tables of all warm and cold events with their dates, length, and maximum CI value will be presented in the following section.

3.2.1. Extreme and Extended Cold Events

Table 5 displays a list of all 29 extreme and extended cold events as defined by the CI index. The table consists of the dates, length, and maximum CI value of the events. Highlighted in light blue are the events that lasted the longest. There are 3 events that lasted a length of 7 consecutive days, February 16th-22nd, 1952; December 9th-15th, 1975; and November 14th-20th, 2009. Although these events were lengthy, they did not have the lowest temperature anomalies. Highlighted in dark blue is the event with the lowest temperature anomaly reached in late February and early March of 1951. It is surprising to note that both the warmest and coldest events occurred primarily in early March and lasted 4 days. Table 6 displays the frequency of

extreme events lasting 4, 5, 6, and 7 days. The few noticeable aspects of this table is how there are no cold events lasting longer than 7 days and how it is frequent to observe 4 day events. Similar to the warm events, it is not always the case that lengthy events contain the coldest anomaly. Randomness occurs when it comes to the intensity of temperature anomalies and the length of these events.

3.2.2. Extreme and Extended Warm Events

Table 7 displays a list of all 34 extreme and extended warm events as defined by the CI index. The table consists of the dates, length, and maximum CI value of the events. Highlighted in light red is the event that lasted the longest; 16 consecutive days from January 29th-February 13th in 2009. The second longest event lasted 8 days and occurred in December 12th-December 23rd of 1996. Although these events were lengthy, they did not have the highest temperature anomaly. Highlighted in dark red is the event that had the highest temperature anomaly reaching a value of 930.904 indicating a really warm eastern China in early March of 2013. Table 8 displays the frequency of extreme events lasting 4, 5, 6, 7, 8, and 16 days. It is more common to observe 4 day events than 5, 6, 7, 8, or 16 days events. It is also not always the case that lengthy events contain the warmest anomaly values. In fact, there is no apparent relationship when it comes to the intensity of temperature anomalies and the length of those events.

3.3. Composite Analysis

A composite of the onset and decay periods for all extreme and extended EAWM events will now be assessed. The composite analysis focuses on the daily evolution of the events by looking at 5 days prior to the first day of the event (onset) and 5 days after the last day of the event (decay). A composite of the HCP and SMH data, on top of the CI index, are also constructed by taking the corresponding dates of the 34 warm events and 29 cold events.

The first two sections will focus on the composite of 29 extreme and extended cold events; the first being a data analysis and the second being a spatial analysis. The last two sections will assess the composite of 34 extreme and extended warm events; the first being a data analysis and the second being a spatial analysis. The data analysis will consist of examining box plots and time series while the spatial analysis will consist of examining 4 atmospheric variables in the following order: 200-hPa zonal wind anomalies (U'_{200}), 500-hPa height anomalies (ϕ'_{500}), sea-level pressure anomalies (SLP'), and 850-hPa temperature anomalies (T'_{850}).

3.3.1. Composite: Data Analysis of Cold Events

a. Onset & Decay of CI Index

At first, an examination of the data distribution using box plots will be assessed. Figure 23a portrays the data distribution composite for onset period of the CI index. On day -5, the median value is slightly above 0 indicating warmer than normal temperature anomalies in eastern China. During the onset period, notice how the median value along with most of the data decreases continuously until the second day of the event (day +1), where most of the data is anomalously cold. On top of this, the range in temperature anomalies, indicated by the whiskers and IQR, continuously shrink as well. This simply shows that there is a lot of variation in the 29 data points during days -5 through day -2 and less variation in the data from day -1 to day +1. An interesting point to make on this figure is that day 0 has a smaller range in data and IQR than day +1 suggesting that all cold events have a much more similar value on the very first day than the second day of the event. Note that day -4 has two outliers with one having an extreme warm temperature anomaly while the other has an extreme cold temperature anomaly. The second day of the event (day +1) also has an outlier with an extremely cold temperature anomaly. In fact,

this is the event that had the coldest value compared to all other events. For further reference to this event, refer to table 5.

Figure 23b portrays the composite data distribution for decay period of the CI index. On day -1 the median value is well below 0 as it is still the second to last day of the event. However, the median value continuously increases during the decay period, indicating the warming that brings about the end of an event. Notice from day +3 to day +5, the median value is still slightly increasing, but at a slow rate. On top of this, it is surprising to note from day -1 to day +1, the range in data and IQR shrink and from day +1 to day +5, the variation increases. One would expect that the last or second to last day of the event would have the smallest range in data, however, it is clear that day +1 has the least variation. Overall, the onset and decay periods of the CI index for the cold events nearly cast a mirror image with the onset period consisting of a decreasing trend toward colder temperatures and the decay period consisting of an increasing trend toward warmer temperatures.

Secondly, an examination of the composites using a time series will be assessed. These figures add further insight to the details conveyed by the boxplots. Figure 24a illustrates the composite of the CI index using a time series corresponding to the onset period of cold events. Each colored lines represent one of the 29 cold events. The black dotted line is the average of all events for each consecutive day. Generally, during the onset period, the range in temperature anomalies decreases and converges toward a similar value; also represented by the boxplots. From day -5 to day -2, the average gradually decreases. From day -2 to day 0, the average decreases at a greater rate and then once again, at a gradual rate. On day -5, less than half (41.38%) of the events started off with negative temperature anomalies, while the remainder beginning with positive temperature anomalies. There is one interesting event that began with the

most extreme negative value, continuously increased in value until day -1, and then dropped again by day 0 and day +1. This event occurred on February 3rd-8th of 1980. This case is of interest for future work due to its dramatic daily variability.

Figure 24b illustrates the composite of the CI index using a time series corresponding to the decay period of cold events. During this period, the range in temperature anomalies converges on day +1 and then diverges; also seen on the boxplots. The average gradually increases indicating an end to the cold event. On day +5, more than half (58.62%) of the events ended with negative temperature anomalies, while the remainder ending with positive temperature anomalies. Overall, the time series also illustrate a near mirror image just as the boxplots did.

An important statement must be made about two separate cold events and their corresponding dates. Event 19 occurred from January 29th-February 1st, 1980 while event 20 occurred from February 3rd-8th, 1980. Consequently, a couple of the onset days of event 20 and the decay days of event 19 overlap. It is rather astounding to note that if the 1 day gap between these events maintained its 1.5σ requirement, it would be considered a single 11 day event which would have been the longest extended cold event in the record. Note the 1 day gap on February 2nd had a value of -468.806 which is not considerably far from the 1.5σ requirement of -491.235.

b. Onset & Decay of SMH Index

Figure 25a displays the data distribution of the SMH index for the corresponding dates of the onset period of cold events. During the onset period, the variation in data is large, but continuously shrinks toward the day of the event. A large variation in data is reasonable due to a large domain and seasonal variability. Note on day -5, most of the data including the median is above 0, indicating a strong SMH (large areal extent) to begin with. In fact, the median value of

the data continuously increases until day 0. This signifies that the SMH is not only expansive at the beginning of the onset period, but it continuously expands until day 0. However, notice how the median value stagnates at day 0 and begin to decrease by day +1. This may suggest that the SMH simply needs to build up its pressure and not have to sustain the increase during the events. Also, when comparing to the temperature anomalies of the CI index, this may suggest a lag between the expansion of the SMH and transportation of cold temperatures to eastern China. Further examination of this hypothesis must be considered.

Figure 25b displays the data distribution of the SMH index for the corresponding decay period of cold events. The median value tends to stagnate a few times during the decay period, but overall, the data continuously decreases until it reaches a value slightly below 0 on day +5. This signifies that the SMH continuously weakens until it is near normal. Also, the variation in data increases and is larger compared to the onset period. This may suggest that during the onset period, the SMH strengthens in a more regular fashion amongst the cases than it does when it weakens during the decay period.

Figure 26a depicts the composite of the SMH index corresponding to the onset period of cold events using a time series which will provide further insight to the information conveyed in the boxplots. First of all, the average increases until day 0 and decreases afterward. A similar pattern is seen on the boxplot, where the median also began to decrease after day 0. Another interesting aspect of this figure is the lack of convergence toward the mean over the time series. This reflects a notable daily variability in the areal extent of the SMH. In fact, this is interesting due to the SMH being such a large scale, semi-permanent feature. Previous studies have indicated that the SMH does have a tendency to shift southeastward toward the East China Sea which may help explain drastic increases in areal extent. On day -5, a vast majority (79.31%) of

the events began with positive anomalies, while only a small fraction of the events began with negative anomalies.

Figure 26b depicts the composite of the SMH index using a time series corresponding to the decay period of cold events. First of all, the average continuously decreases at a fast rate until day +1, and then gradually decreases until day +5 consistent with the weakening of the SMH that heralds an end to the extended cold events. Another rather interesting aspect of this figure is the exceptional daily variability of each event which exceeds that displayed during the onset period. Similar to the onset period, there is a lack of convergence or divergence toward the mean over the time series. On day +5, slightly less than half (44.83%) of the events ended with positive anomalies, while the remainder ended with negative anomalies. Most of the events ended with a weak SMH, but a nearly similar number of events ended with a strong SMH. The decay period seems to depict a slow shift to a weak SMH, even though the temperature anomalies reached warmer than normal values. This may suggest a systematic lag between the two indices. Overall, it is clear from the onset of the SMH time series, the SMH does not need to continuously strengthen during the event itself, but merely needs to gain the strength prior to the event.

c. Onset & Decay of HCP Index

Figure 27a shows the data distribution of the HCP index for the corresponding dates of the onset period of cold events. During the onset period, the variation in data is relatively large and the IQR tends to fluctuate greatly. This suggests that the HCP does not seem to have a clear trend, instead it is highly variable. Note on day -5, most of the data including the median is above 0, indicating an expansive HCP (large areal extent) to begin with. In fact, the median value of the data continuously increases until day +1. This signifies that the HCP is not only

expansive at the beginning of the onset period, but it continuously expands to encompass a larger region of the Northern Hemisphere with colder air.

Figure 27b shows the data distribution of the HCP index for the corresponding decay period of cold events. The median value continuously decreases, indicating a shrinking of the HCP, but still maintains mostly positive anomalies through day +5. This signifies that the HCP is still expansive, but slowly decreasing in areal extent. A few noticeable aspects of this figure are the large variation in data and the lack of outliers. In fact, there is a larger range in data during the decay period than the onset period, similar to the SMH index.

Figure 28a shows the composite of the HCP index corresponding to the onset period of cold events using a time series providing further details that are illustrated from the boxplots. First and foremost, the average areal extent of the HCP gradually increases during the time series, as indicated by the boxplot. This increase reveals that the HCP is expanding, becoming more robust, and encompassing a greater region with cold air. Similar to the SMH, there does not seem to be any significant convergence toward the mean over the time series, perhaps because the areal extent of the HCP exhibits extreme daily variability. On day -5, the vast majority (82.76%) of the events began with positive anomalies, while the remainder began with negative anomalies. Similar to the SMH index, majority of the events are already expansive and strong, however, the HCP continuously increases in average while the SMH began decreasing after day 0.

Figure 28b shows the composite of the HCP index using a time series corresponding to the decay period of cold events. First and foremost, the average areal extent of the HCP continuously decreases after day 0, as indicated by the boxplot. Although the HCP is shrinking over the time series, the average value stays above 0 by day +5, indicating a weakened, yet,

expansive HCP. This gradual decrease reveals that the HCP is encompassing a smaller region of the Northern Hemisphere with cold air. On day +5, 19 of 29 events ended with positive anomalies, while the remaining 10 ended with negative anomalies. The decay period of the cold events seems to favor an expansive HCP though it is shrinking.

d. Data Analysis Summary

Overall, there is a clear pattern indicated by the data analysis of the EAWM cold events. During the onset period, on average, the SMH and HCP continuously expanded while the temperatures in eastern China continuously dropped for majority of the events. This is consistent with many previous studies where a strong SMH leads to a transport of cold temperatures to eastern China. This data analysis also illustrated the negative correlation, where the expansion of the HCP corresponds to the decrease in temperature over eastern China. Also, a majority of the corresponding SMH and HCP data began with expansive anomalies and continuously increased. One would assume, based off the expansive SMH that a majority of the temperature anomalies in eastern China would begin with cold days; however, a majority of the events indicated by the CI index began with warm days before reaching a negative anomaly. As stated previously, this may potentially suggest a lag correlation or even a certain threshold requirement between these indices. For instance, it may be the case that temperatures in eastern China will take time to drop even when the SMH and HCP are expansive in the first place. On top of this, the SMH and HCP became more robust as the days went on. This may suggest that in order for temperatures to meet the extreme criteria in eastern China, a certain expansive threshold must be met by the SMH or HCP.

During the decay period, the exact opposite is seen as the SMH and HCP continuously contract and weaken while the temperatures in eastern China continuously increase for majority

of the events. It is understood that a weakening of the SMH results in less frequent cold surges due to a lack of meridional transport of air from the eastern stretch of the high pressure center. The decay period also illustrated the negative correlation, where the contraction of the HCP corresponds to the increase in temperature over eastern China. It is interesting to note during the decay period of the EAWM cold events, a majority of the events still ended with colder than normal days and an expansive HCP. Some hint as to why, arises from the fact that the HCP is closely related to the temperature anomalies in eastern China. The SMH showed a fast decrease in the average, suggesting the SMH can quickly contract within days. Thus, the weakening of cold air delivery to eastern China via the shrinking of the SMH – which only prevents additional impact of cold air – does not necessarily rid the region of pre-existing cold air. In fact, the suggestion is that in order for temperatures to become warmer in eastern China, a certain negative threshold must be met by the SMH and HCP.

Note there has been no examination of the causality that may lurk behind the relationships amongst the indices. However, careful examining of the data, suggests that the SMH has a direct impact on the regional temperatures in eastern China, which then may impact the HCP. On top of this, it is clear other synoptic features may influence the indices. Nonetheless, further statistical analysis must be conducted in order to understand these relationships.

3.3.2. Composite: Spatial Analysis of Cold Events

a. Onset & Decay of U_{200}

First, the onset of 200-hPa zonal wind anomalies will be examined for cold events. Figure 29(a-g) depicts the evolution of the 200-hPa zonal wind anomalies in meters per second from day -5 to day +1. All composite figures also illustrate the change in magnitude of the variable

between day -5 and day 0 for the onset period and day 0 to day +5 for the decay period, shown in the bottom right panel. The red line outlines the 95% significance level. On day -5, several noticeable anomalies are evident. First, notice the wind anomaly north-south couplet over Asia. There is robustness in positive wind anomalies over the Arctic (north of Siberia) (i.e. stronger winds), negative wind anomalies over Siberia (i.e. weaker winds), and positive wind anomalies over northwest China and Mongolia. Another point of interest is seen over the central to western Pacific where a north-south couplet of wind anomaly is also seen, but not as robust. When observing the evolution of these locations, notice how both sets of couplets become more anomalous as shown and confirmed in the bottom right panel (Fig. 29h). By day +1, both sets of couplets are clearly apparent over Asia and the Pacific. The couplet over Asia not only becomes more anomalous, but it also shifts slightly southward by day +1. The robust positive wind anomaly over China is commonly related to the East Asian Jet (EAJ) which has a typical location around 32.5°N and sits over east Asia (Chang et al., 2006; Yang et al., 2002; Wu and Sun, 2016). As stated before the EAJ is a common feature of the EAWM that aids in cold surge events. Also, notice how the winds become stronger over eastern China and weaken over the western Pacific (east of Japan). This westward shift in wind anomalies clearly represents a retraction of the EAJ toward China. From this composite, it is clear that the jet has retracted during the onset period of cold events.

Secondly, the decay of 200-hPa zonal wind anomalies will be examined for cold events. Figure 30(a-g) depicts the evolution of the 200-hPa zonal wind anomalies in meters per second from day -1 to day +5. On day -1, the second to last day of the events, the two sets of couplets are still evident, but have become less anomalous. During the decay period, the couplets continuously become weaker. When carefully examining the EAJ (positive wind anomaly over

eastern China), notice how it extends back out into the central Pacific by day +5. This clearly resembles an extension of the EAJ during the decay period of cold events. This is also clearly shown in the bottom right panel (Fig. 30h) where eastern China sees a weakening of wind anomalies and the central Pacific sees a strengthening of wind anomalies. Another interesting feature seen on the evolution panels is the strengthening of positive wind anomalies over the Atlantic indicating that the winds are becoming stronger during the decay period.

Overall, the onset and decay period of U'_{200} associated with cold events has several manifest characteristics. First and foremost, the onset period displays two sets of wind anomaly couplets that weaken substantially during the decay period. Secondly, the change in magnitude of wind anomalies during the onset and decay period, display the opposite features, suggesting a rich evolution structure. Lastly, the EAJ has a tendency to retract toward China and shift slightly south during the onset period, and then extend back outward into the central Pacific during the decay period. In fact, this confirms a previous study by Handlos and Martin (2016) that concluded strong cold surge events result in a strengthening of the West Pacific Jet (or EAJ). This was shown through a composite analysis observing 44 cases. In this analysis, the strong SMH results in cold air advection equatorward towards the anomalous convection near Indonesia. These northerly cold winds act to strengthen the convection by enhancing surface convergence and thus vertical motion. From here, the West Pacific Jet (EAJ) increased in magnitude by ultimately enhancing the jet entrance region and Hadley Cell circulation. This confirmation is rather important due to the downstream affects resulted from the strengthened jet.

b. Onset & Decay of ϕ_{500}

We will now examine the 500-hPa height anomalies for the onset period of cold events. Figure 31(a-g) depicts the evolution of the 500-hPa height anomalies in meters from day -5 to

day +1. On day -5, several robust features are evident. A robust positive height anomaly is seen over northern and western Russia, and the Arctic (north of Russia). In fact, this immense positive height anomaly stretches into the North Atlantic mainly over Greenland. A negative height anomaly is seen over Mongolia and eastern Kazakhstan, just southeast of the positive anomaly. And a weak positive anomaly is seen over southern Japan. During the onset period, notice how this wave-train structure gradually propagates east-southeast and becomes more anomalous by day +1. Even the positive anomaly over Greenland has become more robust and extended into northeast Canada and the Hudson Bay. On day +1, the wave-train structure has a northwest-southeast orientation. The change in magnitude of the height anomalies is manifest in Fig. 31h, where four significant changes occurred, all a part of the wave-train feature. This feature resembles several things. First, a strong ridge formation over Siberia and a strong trough over eastern Asia is a perfect set up for massive upper-level convergence right along southern Siberia. This would ultimately strengthen the Siberian-Mongolian High. Secondly, it is important to note that the trough over Eastern Asia is commonly known as the East Asian Trough (EAT) and is a primary feature observed during cold surge events. And last, the wave-train structure observed in the evolution as well as the change in magnitude panel closely resembles the teleconnection pattern known as the Eurasian pattern (EU). As discussed previously, the EU pattern is a large-scale pattern during the Northern Hemisphere winter that greatly affects the variability of the EAWM. The onset period nearly resembles the positive phase where negative height anomalies are seen over Scandinavia/Arctic, positive height anomalies are seen over Siberia and negative height anomalies are seen over eastern China/Japan. The three centers of action during the positive phase are clearly visible in the bottom right panel. However, it is quite clear that there may be another center of action that formed over Japan and migrated to the east. Looking at the

bottom right panel (Fig. 31h), notice how there are four centers of action; the original three as part of the EU pattern, and a positive height anomaly just east of the EAT. This raises an intriguing question regarding the original structure of the EU pattern. With a composite of 29 extreme and extended cold events, the fourth center of action is quite dominant and may ultimately be a common feature during the onset period of cold events.

The decay period of 500-hPa height anomalies for cold events are shown in Fig. 32(a-g). On day -1, the second to last day of the events, notice the evident, but weakened wave-train structure over Asia. During the decay period, the robust anomalies become weaker, nearly diminishing by day +1. In terms of the EU pattern, the decay period does not seem to resemble any phase. Instead, it simply illustrates the diminishing of the positive EU phase. Figure 32h shows several significant changes in magnitude from day -5 to day 0. There are three over Asia as part of the weakening of the positive EU phase, and an increase in height anomalies over Alaska, Western Europe, and Pakistan. Generally, the evolution of the positive EU phase seems to control the EAWM features greatly and may ultimately be the largest contributor in the events lasting for a prolonged period of time. This will further be seen when examining the SLP and temperature anomalies.

Overall, several noteworthy features are seen in the onset and decay period of ϕ'_{500} for cold events. First, the onset period clearly displays a strong wave-train structure over Asia most commonly resembling the positive EU phase and/or an Ural-Siberian Blocking (Wang and Zhang, 2015; Cheung et al., 2012). This structure in the height anomalies will ultimately result in strong subsidence, an intensification of the SMH, and thus strong cold surges in eastern China. In fact, the studies stated above also suggested how this wave-train structure may be the most controlling aspect of the EAWM variability. Secondly, the positive EU phase seems to illustrate

a possible fourth significant center of action just east of Japan. Lastly, the change in magnitude of height anomalies during the onset and decay period nearly displays the opposite structure, suggesting a rich evolution structure.

c. Onset & Decay of SLP

An investigation of sea-level pressure (SLP) anomalies for the onset period of cold events will now be assessed. Figure 33(a-g) depicts the evolution of the SLP anomalies in millibars from day -5 to day +1. On day -5, one noticeable feature is seen. A large robust positive SLP anomaly is seen over western and central Siberia. This robust feature exemplifies the SMH. Looking at the evolution of the SMH, it shifts eastward and southward into eastern Russia and southeastern China, respectively. This is also shown in Fig. 33h where a massive increase in SLP anomalies is seen over Mongolia and eastern China and a decrease is seen over northwest Russia and Scandinavia. The shift in the SMH during the onset period clearly results in strong cold surges that will be shown in the next section when describing the temperature evolution. The evolution of the SMH during the onset period verifies a study by Chang et al (2006) who illustrated the daily evolution of the south-eastward migration of the SMH. The present study fortifies this evolution by identifying it in a composite of 29 extreme and extended cold events.

The decay period of SLP anomalies for cold events are shown in Fig. 34(a-g). On day -1, notice how the SMH begins to diminish and split over western Russia, though robust positive SLP anomalies are still seen over eastern China. Observing the evolution, the SMH continuously weakens over Asia and splits into two with one positive anomaly over eastern Europe and the other over eastern China. By day +5, there is almost no trace of the SMH in eastern Asia, but the positive SLP anomaly is still present in Eastern Europe. The substantial decrease in SLP anomalies is clearly evident in the bottom right panel (Fig. 34h). Another interesting feature seen

during the decay period is the negative SLP over north central Pacific that becomes more anomalous on day +3 and +4, but weakens again on day +5. This feature is known as the Aleutian Low (AL) and tends to fluctuate in strength from day to day as shown in this figure. This is interesting due to the fact that studies have shown the AL to be present during cold surge events. In this case, a modest AL is seen during the decay period and not the onset period.

Overall, the onset and decay period of SLP' for cold events display several characteristics. First, the onset period clearly displays a strong SMH that shifts and extends east-southeastward into eastern Asia. Secondly, the change in magnitude of height anomalies during the onset and decay period nearly displays the opposite structure. Lastly, the onset period does not appear characterized by a strong AL over the central north Pacific; however, during the decay period a modest AL appears briefly. This conclusion appears somewhat odd with previous research regarding the AL and its role in the EAWM.

d. Onset & Decay of T_{850}

Finally, 850-hPa temperature anomalies for the cold events will be considered. Figure 35(a-g) depicts the evolution of 850-hPa temperature anomalies from day -5 to day +1 of the cold events. On day -5, a cold anomaly is seen over Siberia between the Aral Sea and Lake Baikal. Also, a warm anomaly is present over Scandinavia and southeastern China. This wave-train structure in temperature anomalies becomes more robust over time while shifting southeastward. By day +1, eastern China and even parts of Taiwan are covered with immense cold anomalies while northern Siberia and the west Pacific is anomalously warm. This is also shown in the bottom right panel (Fig. 35h) where the significance level of the anomaly regions is indicated.

Figure 36(a-g) shows the composite of 850-hPa temperature anomalies during the decay period of cold events. Day -1 still illustrates the wave-train structure of temperatures anomalies, though it has weakened. During the decay period, the robust temperature anomalies nearly vanish by day +5. The weakening of the anomalies is seen in Fig. 36h. Also shown is the significant increase in warm anomalies over Alaska during the decay period. The warm anomaly over Alaska is brought on by the upper-level ridge that also developed during the decay period (see Fig. 32).

Overall, it is clear that the onset and decay period of 850-hPa temperature anomalies for cold events illustrate several common features. First, the onset period clearly illustrates a strong cold surge migrating southeastward into eastern China as well as a warm anomaly over Siberia and the west Pacific. Secondly, the decay period simply shows the diminishing cold surge. Lastly, the bottom right panels clearly illustrate opposing features for the onset and decay, suggesting that each period has its own clear structure.

e. Spatial Analysis Summary

All in all, the evolutionary composites of cold events clearly demonstrated a typical synoptic structure and illustrated several features seen in Wang and Zhang (2015), Cheung et al. (2012), and Handlos and Martin (2015). The 500-hPa height anomalies clearly resembled a positive EU phase or an Ural-Siberian Blocking (Wang and Zhang, 2015; Cheung et al., 2012). During the onset period, the ridge-trough couplet shifts east-southeastward, resulting in the shift of the SMH and 850-hPa temperature anomalies. By day -1, the 500-hPa height anomalies become nearly stationary. However, this ridge-trough couplet has been perfectly positioned for placing robust upper-level convergence, leading to subsidence, directly over the climatological core of the SMH. With a continuous strengthening of the SMH, it begins to expand and shift

southeastward into eastern China which ultimately results in strong cold surges as seen from the cold anomalies. It may be the case that the prolonged period of the near-stationary positive EU phase resulted in a prolonged period of extreme cold temperatures in eastern China. During the decay period, the positive EU phase completely diminishes over Asia, resulting in the weakening of the SMH, and thus the end to the cold surge events over eastern China. All the while, the EAJ retracted toward eastern China during the onset and extended into the Pacific during the decay period. As in Handlos and Martin (2016) this suggest that after the cold surge event has occurred, the EAJ strengthens in the west Pacific or extends back into the central Pacific by first modulating the convection over Indonesia.

3.3.3. Composite: Data Analysis of Warm Events

a. Onset & Decay of CI Index

At first, an examination of the data distribution using box plots will be assessed. Figure 37a portrays the data distribution composite for onset period of the CI index. On day -5, the median value is above 0 indicating warmer than normal temperature anomalies in eastern China. During the onset period, notice how the median value along with most of the data increases continuously until all of the data is anomalously warm by day +1. In addition, the range in temperature anomalies, indicated by the whiskers and IQR, continuously shrink after day -5. This simply shows that there is a lot of variation in the 34 data points during days -5 through day -2 and less variation in the data from day -1 to day +1. An interesting point to make on this figure is that day 0 has a smaller range in data than day +1 suggesting that all warm events have a much more similar value on the very first day than the second day of the event. Note during the onset period, that many of the days have outliers below the first quartile, indicating colder than normal temperatures which are not unexpected immediately preceding an extended warm event.

Figure 37b portrays the data distribution composite for the decay period of the CI index. The median value begins to decrease to near 0 by day +5 indicating an end to the extended warm events. Not only is the median decreasing, but the IQR is expanding as well indicating that the data is becoming more variable. Note there are two outliers during the decay period, both having an extreme cold anomaly. Overall, the data distributions of both the onset and decay period of the CI index for warm events are nearly mirror images of each other. This signifies that the temperature anomalies increase (decrease) in a regular fashion amongst the cases during the onset (decay) period.

Figure 38a illustrates the onset period of the CI index for the composite using a time series. Every colored line represents a warm event with their corresponding dates. On day -5, the average value is above 0. The average gradually increases during the onset period, indicating the temperatures are warming. The temperature anomalies have a large variation during the beginning, but converge toward the mean during the onset period. On day -5, only 9 of the 34 events began with negative temperature anomalies, while the remainder beginning with positive temperature anomalies. There is one particular event highlighted in gold that has an immense daily variability. Surprisingly, this event began with a positive temperature anomaly, plummeted to the lowest negative anomaly, and quickly rose again to an extreme warm event all within several days. This event occurred on March 16th-21st in 2009, the same season as the longest warm event that lasted 16 days (see Table 7).

Figure 38b illustrates the decay period of the CI index for the composite using a time series. Interestingly, the average value continuously decreases until day +2 where it nearly becomes stagnant near 0; also indicated by the boxplots. On day +5, only 15 of 34 events end with negative temperature anomalies, while the remaining 19 end with positive temperature

anomalies. The event of March 21st-24th, 1958 (purple line), had the greatest daily variability. From an extreme warm event, it drastically dropped in temperature and reached the lowest value on day +3, then rapidly began to increase. Both warm cases with an immense daily variability from the onset and decay period occurred in March. This sparks a question of whether highly variable events are more likely in the month of March when seasonal transitions are occurring. Note there are two events that slightly overlap each other during their onset and decay period. These are event 9 which occurred on November 21st-25th of 1968 and event 10 which occurred on December 3rd-9th of 1968. The onset of event 10 overlaps the decay of event 9 by two days.

b. Onset & Decay of SMH Index

Figure 39a displays the data distribution of the SMH index for the corresponding dates of the onset period of warm events. On day -5, most of the data is below 0 indicating a weakened SMH to begin with. Not only is the SMH already weak to begin with, but the median value gradually decreases illustrating a further weakening of the SMH. There is also greater variation in data at the beginning then nearer day 0. Moreover, note that the smallest variation in data occurs on day 0 compared to the second day of the event (day +1). Another interesting feature seen during the event (day 0 and day +1) is the several outliers that exist above the third quartile. These outliers are illustrating a strong SMH during the start of an extreme warm event which is rather odd. This may suggest that other synoptic features are forcing the extreme warm event.

Figure 39b displays the data distribution of the SMH index corresponding to the decay period of warm events. The data distribution seems to fluctuate greatly day by day. In fact, the median value increases until day +1 then decreases until day +3 where it becomes somewhat stagnant near a value of -0.5. This clearly illustrates that even by day +5 the SMH is still relatively weak. This odd fluctuation is interesting and it may be the case that other global

features or small scale features may be influencing these events to cause such daily variability. Further evaluation should be considered in order to assess this result. There are also fewer outliers during the decay period. Overall, the decay period shows considerable variability in anomalies compared to the onset period where a smooth weakening of the SMH occurs.

Figure 40a shows the composite of the SMH index corresponding to the onset period of warm events using a time series. On day -5, the average value is slightly below 0 indicating that on average the SMH is somewhat weak; as illustrated in the boxplots as well. During the onset period, the average value slightly decreases as it reaches the start of the event. On day -5, only 10 of the events had positive anomalies (strong SMH), while 24 of the events began with negative anomalies (weak SMH). It is interesting that the vast majority of the warm events began with a weak SMH. This is consistent with the CI index, where a majority of the events began as warmer than normal.

Figure 40b displays the composite of the SMH index corresponding to the decay period of warm events using a time series. It is clear that the decay period illustrates a larger daily variation amongst the events than onset. The average value increases until day +1 and then continuously decreases; also shown on the boxplots. On day +5, 10 of the events ended with positive anomalies (strong SMH), while the remaining 24 ended with negative anomalies (weak SMH). Overall, during the onset period, the SMH weakens in a more regular fashion amongst the cases than it strengthens during the decay period, similar to cold events. It is also interesting to note that both the onset and decay period of warm events began and ended with a weak SMH suggesting that the decay period of a warm event does not always signify an onset period for cold events.

c. Onset & Decay of HCP Index

Figure 41a shows the data distribution of the HCP index corresponding to the onset period of warm events. On day -5, most of the data including the median is below 0, indicating a contracted HCP. Not only does the HCP begin with a contracted state, but the median value continuously decreases indicating a further shrinking of the HCP. As stated before, the range of values is consistently large most likely due to the synoptic variability.

Figure 41b shows the data distribution of the HCP index corresponding to the decay period of warm events. The median value generally increases until day +3 and slightly decreases again by day +5. This simply illustrates that the HCP is becoming expansive, however, the median value does not reach above 0, and instead it stagnates around -0.5. Overall, the distribution during the onset and decay period of the HCP index are near mirror images of each other similar to the CI index, but unlike the SMH index.

Figure 42a displays the composite of the HCP index corresponding to the onset period of warm events using a time series. Here, we see a relatively wide range in data and a lot of variability as indicated by the boxplots as well. The average value continuously decreases during the onset period, representing a shrinking HCP. On day -5, 9 of the 34 events begin with positive anomalies (expansive HCP), while the remaining 25 begin with negative anomalies (contracted HCP). Similar to the SMH index, most of the events start off with contracted HCP.

Figure 42b displays the composite of the HCP index corresponding to the decay period of warm events using a time series. Here, we also see a relatively wide range of data and variability. The average value continuously increases each day until it begins to stagnate after day +3 with a value near -0.5. By day +5, the average state of the HCP is still contracted, though not so much as on the last day of the event. On day +5, 15 of the 34 events end with positive anomalies (expansive HCP), while 14 end with negative anomalies (contracted HCP). The decay period of

warm events does not seem to favor either an extended or contracted HCP by day +5; however, the onset period clearly favored an initially contracted state.

d. Data Analysis Summary

Overall, there are several noteworthy features indicated by the data analysis of the EAWM warm events. During the onset period, on average, the SMH and HCP continuously contracted and weakened while the temperatures in eastern China continuously increased for majority of the events. This is consistent with many previous studies such as Chang et al., 2006 and Ha et al., (2012), where a weak SMH leads to fewer cold surges and thus warmer temperatures in eastern China. This analysis also illustrated the negative correlation between the HCP and CI indices, where the contraction of the HCP corresponds to the increase in temperature over eastern China. Secondly, when examining the evolution of the three indices during the onset period, a majority of the corresponding SMH and HCP data began with a contracted state and continuously shrank while the CI index began with warmer than normal temperatures and continuously increased. In this case, there does not appear to be any lag correlation between the indices unlike the onset of cold events where a lag correlation was seen. Recall the SMH and HCP was already expansive, but temperature anomalies were still near average at the beginning before it began to decrease. Lastly, during the onset period of the SMH index for warm events, few events reached beyond a contracted value of -1.5 (see Fig. 40a). In other words, it reveals a possible threshold for the contraction of the SMH. This threshold may suggest that some part of the SMH is still present in the domain, however, when examining a warm event case study; this may not be the case. For instance, the case study illustrated a diminishing of the well-organized SMH; all the while local high pressures formed over the Tibetan Plateau as well the far northeast Siberia. Recall that the domain of the SMH index

includes a large portion of eastern Asia which ultimately would include local high pressure systems. Overall, it is most likely the case that the contracted threshold is simply present due to the large domain picking up local high pressure systems and not the fact that a part of the SMH is still present. It is important to look at further case studies in order to assess if local high pressures over the Tibetan Plateau are a common occurrence during extreme and extended warm events.

During the decay period, the exact opposite is seen where the SMH and HCP generally expanded and strengthened while the temperatures in eastern China continuously decreased for majority of the events. It is understood that a strengthening of the SMH results in frequent cold surges due to efficient meridional transport of cold air from Siberia. The decay period also illustrated the negative correlation between the HCP and CI indices, where an expansive HCP corresponds to the decrease in temperature over eastern China. It is interesting to note during the decay period of the EAWM warm events, a majority of the events still ended with warmer than normal temperatures and a weak SMH. This result clearly emphasizes the close relationship between regional temperatures and the SMH; however, unlike the cold events where a lag correlation seemed to be present, no lag is seen during warm events. It is also important to note that the CI and HCP indices had mirror images in the boxplots, while the SMH index did not (see Fig. 39). The decay period of the SMH did not display any sort of organized structure where the onset period did. Lastly, keep in mind that there are multiple events where the standard EAWM structure is not followed. For instance, there are cases where the SMH and HCP are expansive, yet, eastern China is anomalously warm. As stated previously, this would simply illustrate that other synoptic features may influence the indices.

As a whole, the data analysis clearly illustrates a long term anomalously warm period, weak SMH, and contracted HCP during warm events whereas the opposite is seen during cold events. This suggests that the decay period of warm events does not simply represent the onset of cold events as seen from the still weak SMH and contracted HCP by day +5. It is also true that the onset of warm events is not directly preceded by the decay period of cold events due to the negative SMH and HCP anomalies by day +5. This sparks further research where a longer onset and decay period (-10 and +10) should be assessed in order to see when or if warm events are preceded by cold events or vice versa and generally how long these events tend to last even if they are not extreme any more.

3.3.4. Composite: Spatial Analysis of Warm Events

a. Onset & Decay of U_{200}

First, the onset of 200-hPa zonal wind anomalies for warm events will be examined. Figure 43(a-g) depicts the evolution of the 200-hPa zonal wind anomalies in meters per second from day -5 to day +1. On day -5, several noticeable anomalies are evident. First, notice the north-south wind anomaly couplet over Asia. There are negative wind anomalies over the Arctic (north of Siberia) (i.e. stronger winds), robust positive wind anomalies over Siberia (i.e. weaker winds), and negative wind anomalies over Afghanistan and western China. Another point of interest is seen over the central to western Pacific and the north Atlantic. When observing the evolution of these locations notice how the couplet over Asia becomes more anomalous and extends eastward zonally by day +1; as shown and confirmed in the bottom right panel of the figure. During this evolution the central to western Pacific sees an intensification of positive wind anomalies while the North Atlantic sees a diminishing of positive wind anomalies. An interesting feature seen in Fig. 43h, is the significant increase in positive wind anomalies over

northeast Pacific, southwest Canada, and northwest US. In fact, the strengthening of the winds in this location is not seen during the onset period of cold events. Moreover, the features seen in this panel are nearly the opposite of the onset period of cold events with the exception of the robust couplet over western Pacific. Moreover, the EAJ weakens over eastern China and intensifies over the central Pacific, indicating an extension of the jet which is also seen during the decay phase of the cold events. Although both represent an extension of the jet, different structures are seen in the wind anomalies, suggesting that the decay phase of cold events does not necessarily represent the onset of warm events, instead a more complicated relationship between the two is seen.

Secondly, the decay period of 200-hPa zonal wind anomalies for warm events will be examined. Figure 44(a-g) shows the evolution of 200-hPa zonal wind anomalies in meters per second from day -1 to day +5. On day -1, the second to last day of the event, the couplet over Asia is still evident. However, a robust negative anomaly is now present just east of Japan in the western Pacific. This negative anomaly is northwest of the original positive anomaly seen in the central Pacific. During the decay phase notice how the wind anomalies over eastern China shift to average and now a new set of robust wind anomalies are seen; the original robust positive anomaly over Mongolia and Siberia, the robust negative anomaly east of Japan, and the original positive wind anomaly over the central Pacific. This wave-train structure in wind anomalies shifts eastward into the central Pacific and now has a north-south orientation by day +5. Over most of Asia, the wind anomalies are near normal on day +5, with no indication of an onset of cold events. Figure 44h emphasizes and clearly illustrates the massive increase and decrease of wind anomalies in the regions discussed above.

Overall, the onset and decay period of U'_{200} of warm events has several manifest characteristics. First and foremost, the onset period displays one wind anomaly couplet over Asia that strengthens substantially during the onset period and weakens during the decay period. Secondly, the EAJ has a tendency to extend into the central Pacific during the onset period, but does not retract toward China during the decay period. Instead, there is merely a shift in the wind anomaly couplet to the central Pacific. In fact, days +3, +4, and +5 nearly illustrate classic jet retraction days as portrayed in Handlos and Martin (2016). Lastly, the change in magnitude of wind anomalies during the onset and decay period, display the opposite features with differences in the robustness.

b. Onset & Decay of ϕ_{500}

The onset period of 500-hPa height anomalies for warm events will be examined. Figure 45(a-g) depicts the evolution of the 500-hPa height anomalies in meters from day -5 to day +1. On day -5, several anomalous features are seen. First, notice the wave-train structure of height anomalies over western Asia. There are strong positive height anomalies over the Arctic, negative anomalies over northwest Siberia, positive height anomalies over the Middle East extending into Mongolia and China. In addition to this wave-train structure, Western Europe has a robust positive height anomaly while the North Atlantic has a robust negative height anomaly. During the onset period, notice how the negative anomaly over Siberia becomes more anomalous and extends zonally while the positive height anomaly over the Middle East becomes robust and shifts eastward into northeast China and Japan by day +1. This wave-train structure in height anomalies is the perfect representation of the negative EU phase. It is important to note that the onset period of warm events illustrates the same exact evolution as the onset period of cold events, but with oppositely signed centers of action. Also, the fourth center of action in the EU

phase discussed previously does show up in the warm events, but is significantly smaller than its counterpart in the cold events.

The decay period of 500-hPa height anomalies for warm events is shown in Fig. 46(a-g). On day -1, the negative EU phase is still present except a new robust positive height anomaly is seen over the Bering Sea. During the decay period, notice how the negative EU phase diminishes over Asia. The robust negative height anomaly over Siberia weakens rapidly and shifts northwestward back to its original position as seen during the onset period on day -5. The positive height anomaly over Japan becomes entwined with the positive height anomaly over the Bering Sea. By day +5, a strong positive height anomaly is seen over the central north Pacific, while negative height anomalies are seen over northwest Siberia, and northwest Canada. The change in height anomalies is clearly shown in Fig. 46h. It is important to note that the decay phase of warm events illustrates the same exact evolution as the decay phase of cold events, but with oppositely signed centers of actions; as denoted by the bottom right panels.

Overall, several noteworthy features are seen in the onset and decay period of ϕ'_{500} for warm events. First, the onset period displays a weakened ridge-trough feature over Asia that clearly denotes the negative EU phase with a fourth small, but significant, center of action east of Japan, while the decay period is merely a diminishing of the negative EU phase. As stated from Wang and Zhang (2015) and Cheung et al. (2012), the negative EU phase or a weak Ural-Siberian Blocking is related to a weakened EAWM which is clearly illustrated in the above results with warmer than normal temperatures. Secondly, the evolution of the onset and decay period for warm events exemplifies the same exact evolution as the cold events, but with oppositely signed centers of action.

c. Onset & Decay of SLP

The onset period of sea-level pressure (SLP) anomalies for warm events will now be examined. Figure 47(a-g) depicts the evolution of SLP anomalies from day -5 to day +1. On day -5, several noticeable features are seen. First, a large robust positive SLP anomaly is seen over the Arctic corresponding to the positive height anomalies at 500-hPa and a small positive SLP anomaly is seen over the Tibetan Plateau. Robust negative SLP anomalies are seen over western Siberia and the North Atlantic. During the onset period, notice how the negative SLP anomaly becomes more robust and shifts eastward into central Siberia, Mongolia, and China. Similar to the SMH during cold events, notice how the negative SLP anomaly extends down into southeastern China. It is important to note that the negative SLP anomaly most likely represents an extremely weakened SMH. To determine if the negative SLP anomaly is merely a weakened SMH or even a low pressure system, further investigation needs to be taken.

The decay period of SLP anomalies for warm events are shown in Fig. 48(a-g). On day -1, the negative SLP anomaly is still evident in eastern China. A robust positive SLP anomaly is now seen over Alaska as well. During the decay period, notice the negative anomaly over China has completely diminished by day +5 while the positive SLP anomaly over Alaska has shifted southwestward in the north central Pacific. Another interesting feature seen in the evolution is how the Arctic becomes positively anomalous for a few days all the while a brief positive SLP anomaly formed and diminished near Lake Baikal. This reiterates the fact that the decay period of warm events does not necessarily represent the onset of cold events where a reemergence of the SMH is seen. The bottom right panel (Fig. 48h) clearly illustrates the changes in SLP anomalies where very similar features are seen for a classic jet retraction event (Handlos and Martin, 2016).

Overall, the onset and decay period of SLP' for warm events display several characteristics. First, the onset period clearly displays an extremely weakened SMH (possibly to the extent that a surface low pressure center occupies the region) that shifts and extends east-southeastward into eastern Asia following the same exact path as the positive SLP anomalies associated with the cold events. Lastly, the change in magnitude of height anomalies during the onset and decay period for warm events nearly displays the opposite features as the onset and decay period of cold events.

d. Onset & Decay of T_{850}

Finally, 850-hPa temperature anomalies will be considered for the onset period of warm events. Figure 49(a-g) portrays the onset period of temperature anomalies in degrees Celsius from day -5 to day +1. On day -5, there are colder than normal temperatures in northwest Siberia and warmer than normal temperatures over the Middle East. During the onset period, notice how both of these anomalies become more robust and extend zonally. Not only does the positive temperature anomaly become more robust, but it shifts eastward into Mongolia and consolidates in eastern China by day +1. When looking at the bottom right panel (Fig. 49h), it is interesting to note that Canada and the north central US are characterized by positive temperature anomalies, significant in portions of the central plains. In fact, since the temperatures in that region shift from negative anomalies to positive anomalies, this represents a warm up.

Finally, the composite of 850-hPa temperature anomalies during the decay period of warm events will be assessed (Fig. 50(a-g)). On day -1, the Siberian and classic anomalous features are still present. During the decay phase, notice how both features shift slightly eastward and diminish completely by day +5. The change in temperature anomalies is also seen in the

bottom right panel (Fig. 50h) where eastern China sees a decrease in temperature anomalies, illustrating the weakening of the warmer than normal temperatures.

e. Spatial Analysis Summary

Overall, these results elucidate a coherent synoptic structure to the onset and decay periods of warm events. Generally, it is clear from the daily evolution of all four atmospheric variables that a weakened EAWM circulation is occurring. For instance, negative height anomalies over Siberia illustrate a weakened ridge; while positive height anomalies over eastern China, illustrate a weakened EAT. Ultimately, this would result in a weakened SMH and thus weaker cold surges in eastern China. This analysis clearly represents the negative EU phase. In fact, it is widely reported that the negative EU phase results in a weaker SMH, weaker EAJ, weaker EAT, fewer cold surges, and more precipitation over eastern Asia (Gong et al., 2001; Liu and Chen, 2012; Sung et al., 2009).

To emphasize the weakened EAWM event, a brief examination of the synoptic evolution is presented. The large scale 500-hPa height anomalies is perfectly oriented over Siberia where weaker upper-level convergence is present, leading to much weaker subsidence, thus resulting in a weaker SMH. During the onset period, the height anomalies shifted east-southeastward, resulting in the shift of the weakened SMH and 850-hPa temperature anomalies. By day -1, the 500-hPa height anomalies become nearly stationary. However, the extremely weakened SMH shifts southeastward into eastern China most likely without sufficient circulatory strength to induce a cold surge. All the while, the EAJ is continuously shifting toward the central Pacific and strengthening in time during both the onset and decay period. This is a great illustration of the results presented in Handlos and Martin (2016) where days +3, +4, and +5 closely resemble a classic jet retraction event. During the decay phase, the height anomalies over Asia diminish

which result in the diminishing of the already weakened SMH and thus the end to the warm event over eastern China.

4. Conclusion & Future Work

When examining the time series of seasonal averaged anomalies for all three indices (HCP, SMH, CI), noticeable trends were evident. Both the HCP and SMH experienced a systematic decrease, suggesting both features have been shrinking in size over the past 65 winter seasons. The CI index illustrated a positive trend, signifying that eastern China has become warmer in the past 65 winter seasons. It is important to examine if this warming trend is a direct result or manifestation of the weakening of the SMH or if it is simply a manifestation of a physically separate, regional global warming issue. In addition, significant daily correlations (CI & SMH: -0.42; CI & HCP: -0.51; SMH & HCP: 0.46) and seasonal correlations (CI & SMH: -0.62; CI & HCP: -0.75; SMH & HCP: 0.59) between all three indices were seen. In both cases, the CI and HCP had the strongest relationship; suggesting, as in Martin (2015), that eastern China's winter temperatures bear an unusually intimate relationship to the areal extent of the HCP. The time series of all three indices displayed a possible lag correlation that needs to be further addressed in future work in order to determine which index precedes or follows the other. For instance, as previously hypothesized, it may be the case that the SMH first influences the cold surges in eastern China and thus affects the areal extent of the HCP. Further statistical work needs to be undertaken in order to assess this problem.

The spatial composites of both extreme and extended cold and warm events displayed distinctive synoptic structures. First, the 200-hPa zonal wind anomalies displayed rather intriguing results. The EAJ has a robust positive wind anomaly over China during the onset period of cold events that migrates and extends into the central Pacific during the decay period, illustrating that after a cold surge has occurred, an intensification of the EAJ is seen over the

central Pacific. During warm events, the EAJ has a negative wind anomaly over China during the onset period that migrates into the central Pacific during the decay period, illustrating that after a warm event has occurred, a weakening of the EAJ is seen over the central Pacific. In general, during colder (warmer) events in eastern China, the EAJ tends to extend (retract) into the central Pacific. This confirms part of a study by Handlos and Martin (2016) that hypothesized a potential relationship between the intensification of the Pacific Jet and cold surge events. The study concluded that strong cold surge events are associated significantly with a strong West Pacific jet also referred to as the EAJ in the current study. This was shown through a composite analysis observing 44 cases. In this analysis, the strong SMH results in cold air advection equatorward towards the anomalous convection near Indonesia. These cold northerly winds act to strengthen the convection by enhancing surface convergence and thus vertical motion which in turn strengthens the Hadley cell circulation. From here, the West Pacific Jet (EAJ) intensifies. This is similar to the current study where the evolution of U'_{200} illustrated a migration and extension of the positive wind anomaly from China to the central Pacific, suggesting again, that the cold surge events affects the strength of the EAJ or Pacific Jet.

Secondly, the evolution of the cold (warm) events clearly portrayed a preferred synoptic setup for the production of strong (weak) cold surges. With a ridge-trough pattern over Siberia and eastern Asia, strong subsidence forced over in Siberia resulting in an intensification of the SMH. The subsequent southeastward migration of the SMH, led to a drop in temperature over eastern China. The evolution of warm events seems to portray an extremely weakened cold surge where a weakened ridge-trough pattern is seen over Siberia and eastern Asia, resulting in much weaker subsidence (if at all any), and thus a weakened SMH. Though the weakened SMH still migrates to eastern China, it does not bring large negative temperature anomalies. Overall, the

synoptic evolution of these features confirms parts of previous studies on the synoptic understanding of the EAWM (Chang et al., 1980; Chang, 2004; Chang et al., 2006; Ding, 1994; Handlos and Martin, 2016; Sun et al., 1997; Sung et al., 2009; Ha et al., 2012; Chen et al., 1991).

From the composites of 500-hPa height anomalies, a rather intriguing feature was seen during the onset period of the cold and warm events. As discussed previously, the EU pattern was robust; illustrating a positive phase during the onset of cold events and a negative phase during the onset of warm events. The decay periods of each type of event merely illustrated the diminishment of the associated governing phases. Wang and Zhang (2015) illustrated that the EU pattern has a strong daily variability, as well as a 10-day lifespan. In the current study, an examination of these events was made 5 days prior to the first day of the event and 5 days following the last day of the event. Although the actual events vary in length, the evolution still gives a reasonable perspective on the life-span of the EU pattern. For instance, during the onset periods, the phases were well developed and during the decay periods, the phases completely diminished. This gives a rough conclusion that the EU pattern may indeed have a near 10-day lifespan as suggested by Wang and Zhang (2015). Essentially, the prolonged EU phases may be the ultimate contributor to the prolonged EAWM events in eastern China (Cheung et al., 2012; Wang and Zhang, 2015). From this observation, it is apparent that there is a clear connection between the EU pattern and the EAWM strength that needs to be further explored in future work.

To conclude, it is vital to conduct several case studies examining the evolution of extreme and extended cold and warm events. This would allow a better understanding of the physical synoptic structural evolution during these events. It may also support and extend the insights derived from analysis of the composite structures presented in this work. In fact, an examination of a cold event case has briefly been assessed and for the most part, the evolution

was very similar to the composites. However, an interesting feature was seen for this case study. The temperatures in eastern China were stagnant for several days until the temperatures drastically dropped even further. Though the SMH was present, a cyclone formed south of Japan, intensified and migrated northeastward at the same time the temperatures began to drop drastically. This may suggest that cyclones that form over Japan can greatly influence the cold surge events by aiding the SMH in a meridional transport of cold air. Previously, many studies illustrated that the AL, a climatological feature representing multiple lows, was the dominant feature that aided the SMH in transporting cold air; however, it may be circulations associated with individual cyclones that are more important in this circumstance. An investigation of other events must be taken in order to further assess the influence of similar synoptic structures on the EAWM.

All in all, this study reiterated the strong correlation between the temperatures in eastern China and the areal extent of the HCP by constructing a new index. Nonetheless, much more statistical work needs to be conducted in order to further understand the relationship between the two indices as well as the SMH index. In addition, this work established that the EAWM has a strong daily variability that is utterly influenced by synoptic features, revealing that the EAWM must also be considered on synoptic time scales rather than the seasonal time scales on which most prior studies have focused in the past. Last but not least, the composites clearly demonstrated a standard synoptic scale evolution of the environment preceding and following the extreme and extended EAWM events that sparked even further questions for future work.

5. References

- Arrhenius, P. S. (1896). XXXI. On the influence of carbonic acid in the air upon the temperature of the ground. *Philosophical Magazine*, 41(251), 237–276.
<https://doi.org/10.1080/14786449608620846>
- Brohan, P., Kennedy, J. J., Harris, I., Tett, S. F. B., & Jones, P. D. (2006). Uncertainty estimates in regional and global observed temperature changes: A new data set from 1850. *Journal of Geophysical Research: Atmospheres*, 111(D12), D12106. <https://doi.org/10.1029/2005JD006548>
- Callendar, G. S. (1938). The artificial production of carbon dioxide and its influence on temperature. *Quarterly Journal of the Royal Meteorological Society*, 64(275), 223–240.
<https://doi.org/10.1002/qj.49706427503>
- Chang, Chih-Pei. (2004). *East Asian Monsoon*. World Scientific.
- Chang, C-P., & Lau, K. M. W. (1980). Northeasterly Cold Surges and Near-Equatorial Disturbances over the Winter MONEX Area During December 1974. Part II: Planetary-Scale Aspects. *Monthly Weather Review*, 108(3), 298–312. [https://doi.org/10.1175/1520-0493\(1980\)108<0298:NCSANE>2.0.CO;2](https://doi.org/10.1175/1520-0493(1980)108<0298:NCSANE>2.0.CO;2)
- Chang, C.-P., Wang, Z., & Hendon, H. (2006). The Asian winter monsoon. In *The Asian Monsoon* (pp. 89–127). Springer, Berlin, Heidelberg. https://doi.org/10.1007/3-540-37722-0_3
- Change, I. P. on C. (2014). *Climate Change 2013: The Physical Science Basis: Working Group I Contribution to the Fifth Assessment Report of the Intergovernmental Panel on Climate Change*. Cambridge University Press.
- Chen, L. X., Q. G. Zhu, and H. B. Luo (1991). In *East Asian Monsoon* (pp. 362). China Meteorological Press.

- Cheung, H. N., Zhou, W., Mok, H. Y., & Wu, M. C. (2012). Relationship between Ural–Siberian Blocking and the East Asian Winter Monsoon in Relation to the Arctic Oscillation and the El Niño–Southern Oscillation. *Journal of Climate*, *25*(12), 4242–4257.
<https://doi.org/10.1175/JCLI-D-11-00225.1>
- Ding, Y. (1994). Monsoons over China. *Kluwer Acad., Norwell, Mass.*, 419 pp.
- Fourier, J. (1824). Remarques générales sur les températures du globe terrestre et des espaces planétaires. *Annales de Chimie et de Physique* (Vol. 27, No. 136-167).
- Gong, Dao-Yi, & Ho, C.-H. (2004). Intra-seasonal variability of wintertime temperature over East Asia. *International Journal of Climatology*, *24*(2), 131–144. <https://doi.org/10.1002/joc.1006>
- Gong, Dao-Yi, Wang, S.-W., & Zhu, J.-H. (2001). East Asian Winter Monsoon and Arctic Oscillation. *Geophysical Research Letters*, *28*(10), 2073–2076.
<https://doi.org/10.1029/2000GL012311>
- Gong, D.-Y., & Ho, C.-H. (2002). The Siberian High and climate change over middle to high latitude Asia. *Theoretical and Applied Climatology*, *72*(1–2), 1–9.
<https://doi.org/10.1007/s007040200008>
- Ha, K.-J., Heo, K.-Y., Lee, S.-S., Yun, K.-S., & Jhun, J.-G. (2012). Variability in the East Asian Monsoon: a review. *Meteorological Applications*, *19*(2), 200–215.
<https://doi.org/10.1002/met.1320>
- Handlos, Z. J., & Martin, J. E. (2016). Composite Analysis of Large-Scale Environments Conducive to Western Pacific Polar/Subtropical Jet Superposition. *Journal of Climate*, *29*(19), 7145–7165.
<https://doi.org/10.1175/JCLI-D-16-0044.1>

- Hansen, J., Ruedy, R., Sato, M., Imhoff, M., Lawrence, W., Easterling, D., ... Karl, T. (2001). A closer look at United States and global surface temperature change. *Journal of Geophysical Research: Atmospheres*, 106(D20), 23947–23963. <https://doi.org/10.1029/2001JD000354>
- Hansen, J., Ruedy, R., Sato, M., & Lo, K. (2010). Global Surface Temperature Change. *Reviews of Geophysics*, 48(4), RG4004. <https://doi.org/10.1029/2010RG000345>
- He, S., & Wang, H. (2013). Oscillating Relationship between the East Asian Winter Monsoon and ENSO. *Journal of Climate*, 26(24), 9819–9838. <https://doi.org/10.1175/JCLI-D-13-00174.1>
- Jhun, J.-G., & Lee, E.-J. (2004). A New East Asian Winter Monsoon Index and Associated Characteristics of the Winter Monsoon. *Journal of Climate*, 17(4), 711–726. [https://doi.org/10.1175/1520-0442\(2004\)017<0711:ANEAWM>2.0.CO;2](https://doi.org/10.1175/1520-0442(2004)017<0711:ANEAWM>2.0.CO;2)
- Kalnay, E., Kanamitsu, M., Kistler, R., Collins, W., Deaven, D., Gandin, L., ... Joseph, D. (1996). The NCEP/NCAR 40-Year Reanalysis Project. *Bulletin of the American Meteorological Society*, 77(3), 437–471. [https://doi.org/10.1175/1520-0477\(1996\)077<0437:TNYRP>2.0.CO;2](https://doi.org/10.1175/1520-0477(1996)077<0437:TNYRP>2.0.CO;2)
- Karl, T., Hassol, S., Miller, C., & Murray, W. (2006). *Temperature Trends in the Lower Atmosphere. Steps for Understanding and Reconciling Differences*. do not have: U.S. Climate Change Science Program//Subcommittee on Global Change Research. Retrieved from <http://www.climatechange.gov/Library/sap/sap1-1/default.php>
- Koch, S. E., desJardins, M., & Kocin, P. J. (1983). An Interactive Barnes Objective Map Analysis Scheme for Use with Satellite and Conventional Data. *Journal of Climate and Applied Meteorology*, 22(9), 1487–1503. [https://doi.org/10.1175/1520-0450\(1983\)022<1487:AIBOMA>2.0.CO;2](https://doi.org/10.1175/1520-0450(1983)022<1487:AIBOMA>2.0.CO;2)

- Li, QingXiang, Dong, W., Li, W., Gao, X., Jones, P., Kennedy, J., & Parker, D. (2010). Assessment of the uncertainties in temperature change in China during the last century. *Chinese Science Bulletin*, 55(19), 1974–1982. <https://doi.org/10.1007/s11434-010-3209-1>
- Li, Qingxiang, Zhang, H., Liu, X., Chen, J., Li, W., & Jones, P. (2009). A Mainland China Homogenized Historical Temperature Dataset of 1951–2004. *Bulletin of the American Meteorological Society*, 90(8), 1062–1065. <https://doi.org/10.1175/2009BAMS2736.1>
- Lin, X. C., S. Q. Yu, and G. L. Tang (1995). Chinese temperature series during recent 100 years. *Chin. J. Atmos. Sci.*, 15, 525–534.
- Liu Y.Y., Chen W. (2012). Variability of the Eurasian teleconnection pattern in the Northern Hemisphere winter and its influences on the climate in China. *Chin. J. Atmos. Sci.*, 36(2), 423–432.
- Lugina, K. M., P. Ya. Groisman, K. Y. Vinnikov, V. V. Koknaeva, and N. A. Speranskaya, (2005). Monthly surface air temperature time series area-averaged over the 30-degree latitudinal belts of the globe, 1881–2005. *Carbon Dioxide Information Analysis Center, Oak Ridge National Laboratory, U.S. Department of Energy*. <https://doi:10.3334/CDIAC/cli.003>
- Martin, J. E. (2015). Contraction of the Northern Hemisphere, Lower-Tropospheric, Wintertime Cold Pool over the Past 66 Years. *Journal of Climate*, 28(9), 3764–3778. <https://doi.org/10.1175/JCLI-D-14-00496.1>
- Sakai, K., & Kawamura, R. (2009). Remote response of the East Asian winter monsoon to tropical forcing related to El Niño–Southern Oscillation. *Journal of Geophysical Research: Atmospheres*, 114(D6), D06105. <https://doi.org/10.1029/2008JD010824>
- Simmons, A. J., Berrisford, P., Dee, D. P., Hersbach, H., Hirahara, S., & Thépaut, J.-N. (2016). A reassessment of temperature variations and trends from global reanalyses and monthly surface

climatological datasets. *Quarterly Journal of the Royal Meteorological Society*, 143(702), 101–119. <https://doi.org/10.1002/qj.2949>

Simmons, A. J., Poli, P., Dee, D. P., Berrisford, P., Hersbach, H., Kobayashi, S., & Peubey, C. (2014). Estimating low-frequency variability and trends in atmospheric temperature using ERA-Interim. *Quarterly Journal of the Royal Meteorological Society*, 140(679), 329–353. <https://doi.org/10.1002/qj.2317>

Smith, T. M., Peterson, T. C., Lawrimore, J. H., & Reynolds, R. W. (2005). New surface temperature analyses for climate monitoring. *Geophysical Research Letters*, 32(14), L14712. <https://doi.org/10.1029/2005GL023402>

Smith, T. M., & Reynolds, R. W. (2005). A Global Merged Land–Air–Sea Surface Temperature Reconstruction Based on Historical Observations (1880–1997). *Journal of Climate*, 18(12), 2021–2036. <https://doi.org/10.1175/JCLI3362.1>

Stocker, T. F., and Coauthors, Eds. (2014). *Climate Change 2013: The Physical Science Basis*. Cambridge University Press, 1535 pp.

Sun, B. M., and C. Y. Li (1997). Relationship between the disturbances of East Asian trough and tropical convective activities in boreal winter. *Chin. Sci. Bull.*, 42, 500–504.

Sung, M.-K., Lim, G.-H., Kwon, W.-T., Boo, K.-O., & Kug, J.-S. (2009). Short-term variation of Eurasian pattern and its relation to winter weather over East Asia. *International Journal of Climatology*, 29(5), 771–775. <https://doi.org/10.1002/joc.1774>

Tang, G. L., & Ren, G. Y. (2005). Reanalysis of surface air temperature change of the last 100 years over China. *Climatic and Environmental Research*, 10(4), 791-798.

- Thorne, P. W., Lanzante, J. R., Peterson, T. C., Seidel, D. J., & Shine, K. P. (2010). Tropospheric temperature trends: history of an ongoing controversy. *Wiley Interdisciplinary Reviews: Climate Change*, 2(1), 66–88. <https://doi.org/10.1002/wcc.80>
- Tubi, A., & Dayan, U. (2012). The Siberian High: teleconnections, extremes and association with the Icelandic Low. *International Journal of Climatology*, 33(6), 1357–1366. <https://doi.org/10.1002/joc.3517>
- Tyndall, J. (1859). Note on the Transmission of Radiant Heat through Gaseous Bodies. *Proceedings of the Royal Society of London Series I*, 10, 37–39.
- Wang, J., Xu, C., Hu, M., Li, Q., Yan, Z., Zhao, P., & Jones, P. (2014). A new estimate of the China temperature anomaly series and uncertainty assessment in 1900–2006. *Journal of Geophysical Research: Atmospheres*, 119(1), 2013JD020542. <https://doi.org/10.1002/2013JD020542>
- Wang, L., & Chen, W. (2010). How well do existing indices measure the strength of the East Asian winter monsoon? *Advances in Atmospheric Sciences*, 27(4), 855–870. <https://doi.org/10.1007/s00376-009-9094-3>
- Wang, L., & Chen, W. (2013). An Intensity Index for the East Asian Winter Monsoon. *Journal of Climate*, 27(6), 2361–2374. <https://doi.org/10.1175/JCLI-D-13-00086.1>
- Wang, N., & Zhang, Y. (2015). Evolution of Eurasian teleconnection pattern and its relationship to climate anomalies in China. *Climate Dynamics*, 44(3–4), 1017–1028. <https://doi.org/10.1007/s00382-014-2171-z>
- Wang, S. W., and D. Z. Ye (1993). An analysis of global warming during the last one hundred years. *Climate Variability—Proceedings of International Workshop on Climate Variabilities (IWCV)*, Ye et al., Eds., *China Meteorological Press*, 23–32.

- Wang, S. W. (1990). Trends and periodic of Chinese temperature changes during recent 100 years. *Meteorology*, *16*, 11–15.
- Wang, S. W., J. L. Ye, and D. Y. Gong (1998). Construction of mean annual temperature series for the last one hundred years in China. *J. Appl. Meteorol. Sci.*, *9*, 392–401.
- Wen, C., Graf, H.-F., & Ronghui, H. (2000). The interannual variability of East Asian Winter Monsoon and its relation to the summer monsoon. *Advances in Atmospheric Sciences*, *17*(1), 48–60. <https://doi.org/10.1007/s00376-000-0042-5>
- Wu, B., & Wang, J. (2002). Winter Arctic Oscillation, Siberian High and East Asian Winter Monsoon. *Geophysical Research Letters*, *29*(19), 1897. <https://doi.org/10.1029/2002GL015373>
- Wu, S., & Sun, J. (2016). Variability in zonal location of winter East Asian jet stream. *International Journal of Climatology*, n/a-n/a. <https://doi.org/10.1002/joc.4947>
- Xu, M., Xu, H., & Ma, J. (2016). Responses of the East Asian winter monsoon to global warming in CMIP5 models. *International Journal of Climatology*, *36*(5), 2139–2155. <https://doi.org/10.1002/joc.4480>
- Yang, S., Lau, K.-M., & Kim, K.-M. (2002). Variations of the East Asian Jet Stream and Asian–Pacific–American Winter Climate Anomalies. *Journal of Climate*, *15*(3), 306–325. [https://doi.org/10.1175/1520-0442\(2002\)015<0306:VOTEAJ>2.0.CO;2](https://doi.org/10.1175/1520-0442(2002)015<0306:VOTEAJ>2.0.CO;2)
- Zhao, Z. C., S. W. Wang, and Y. Xu (2005). Attribution of the 20th century climate warming in China. *Clim. Environ. Res.*, *10*, 808–817.
- Zhou, W., Wang, X., Zhou, T. J., Li, C., & Chan, J. C. L. (2007). Interdecadal variability of the relationship between the East Asian winter monsoon and ENSO. *Meteorology and Atmospheric Physics*, *98*(3–4), 283–293. <https://doi.org/10.1007/s00703-007-0263-6>

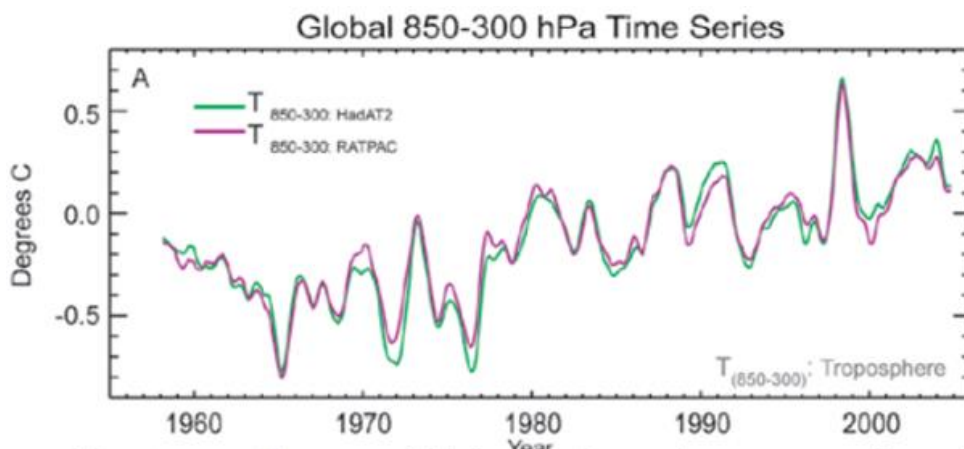


Figure 1: Time series of globally averaged tropospheric temperature ($T_{(850-300)}$) for RATPAC (violet) and HadAT2 (green) radiosonde datasets. All time series are 7-month running averages of original monthly data, which were expressed as a departure ($^{\circ}\text{C}$) from the 1979-97 average. (From Karl et al. 2006)

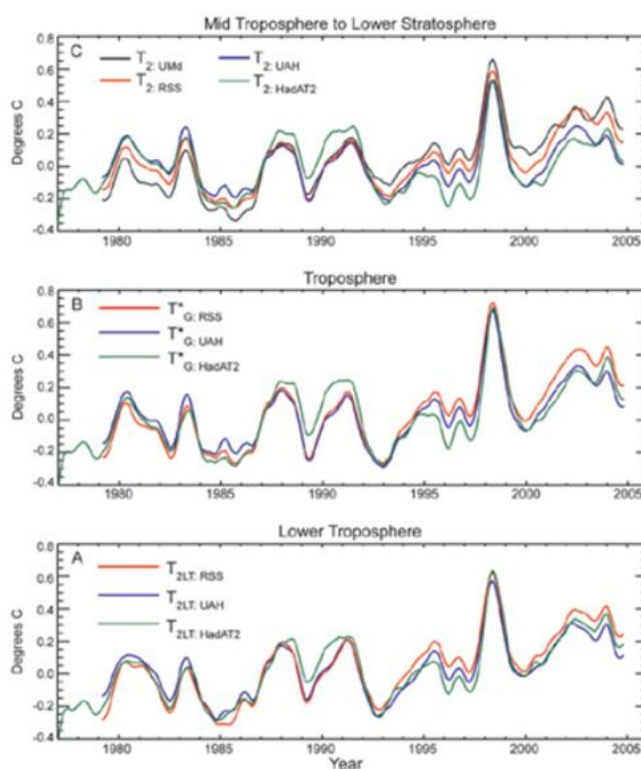


Figure 2: (a) Time series of globally averaged lower tropospheric temperature (T_{2LT}) as follows: UAH (blue) and RSS (red) satellite datasets, and HadAT2 (green) radiosonde data. All time series are 7-month running averages of original monthly data, which were expressed as a departure ($^{\circ}\text{C}$) from the 1979-97 average. (b) As for Fig. 2a but for globally averaged middle tropospheric temperature (T_{G}^{*}). (c) As for Fig. 2a but for upper tropospheric temperature (T_{2}). (From Karl et al. 2006)

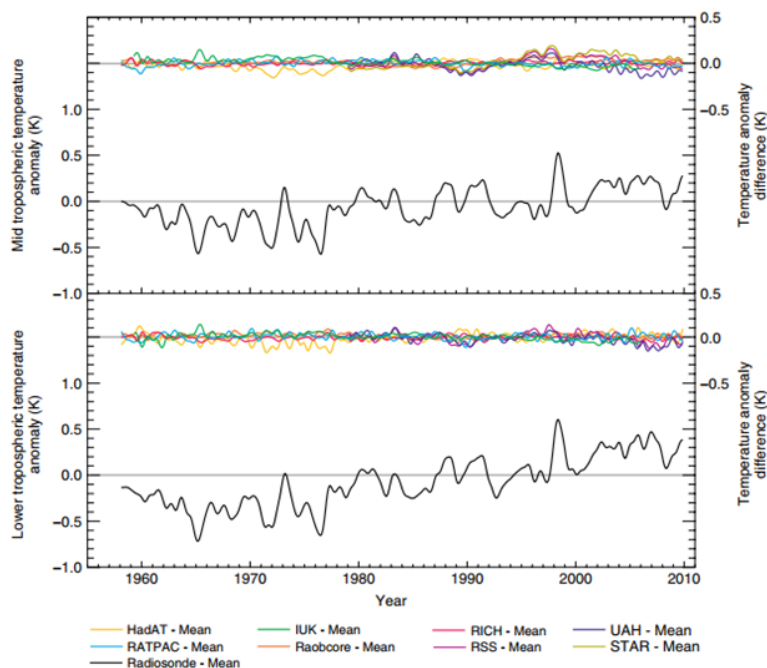


Figure 3: Smoothed global-mean temperature anomalies from 1958-2009 based on radiosonde and MSU datasets for two layers (top MT; bottom LT). In each panel, the bottom trace is the average of five radiosonde datasets (HadAT, RATPAC, IUUK, RAOBCORE, and RICH), and above are differences for individual datasets. Modified from State of the Climate in 2008¹⁹⁴ and courtesy of Carl Mears, Remote Sensing Systems.

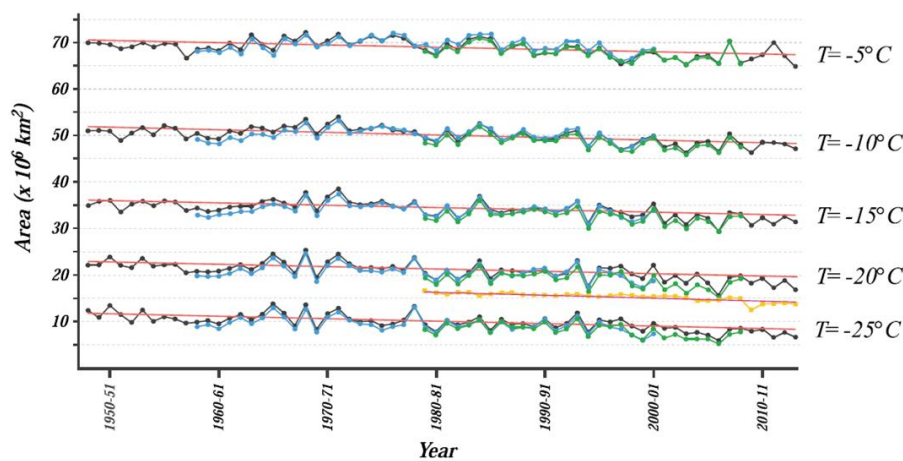


Figure 4: Time series of seasonally averaged areal extent of 850-hPa cold pool at five indicated threshold temperatures. Black line with black dots is the 66-yr time series derived from the NCEP reanalysis data. Blue line with blue dots is the 44-yr time series derived from the ERA-40 data. Green line with green dots is the 30-yr time series derived from the NCEP CFSR data. Red lines represent the trend lines (significant at the 99.9% level) calculated using the NCEP reanalysis time series. Orange line with squares is the 30-yr time series of February sea ice extent with magenta line indicating the trend (significant at the 99.9% level). (From Martin 2015)

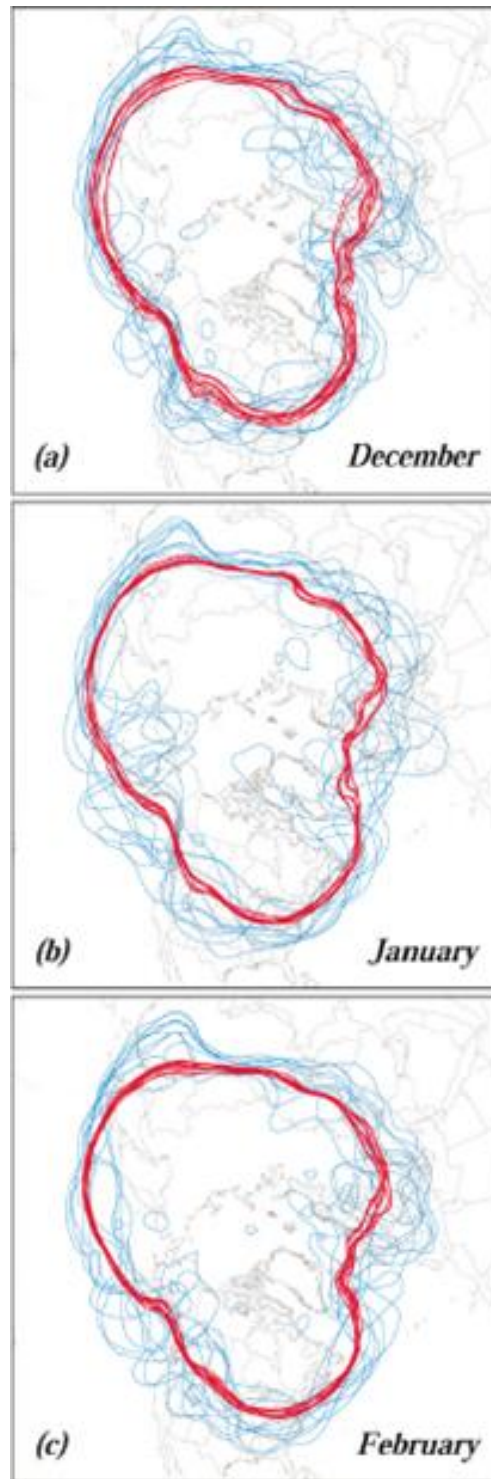


Figure 5: (a) Blue lines are daily averaged -5°C isotherm on 12 select December days (see text for explanation) when the areal extent of -5°C air was $>2\sigma$ above the 66-yr mean for that day. Thick red lines are the 66-yr daily average -5°C isotherms for those calendar days. (b) As in (a), but for the 11 select days in January. (c) As in (a), but for the 11 select days in February. (From Martin 2015)

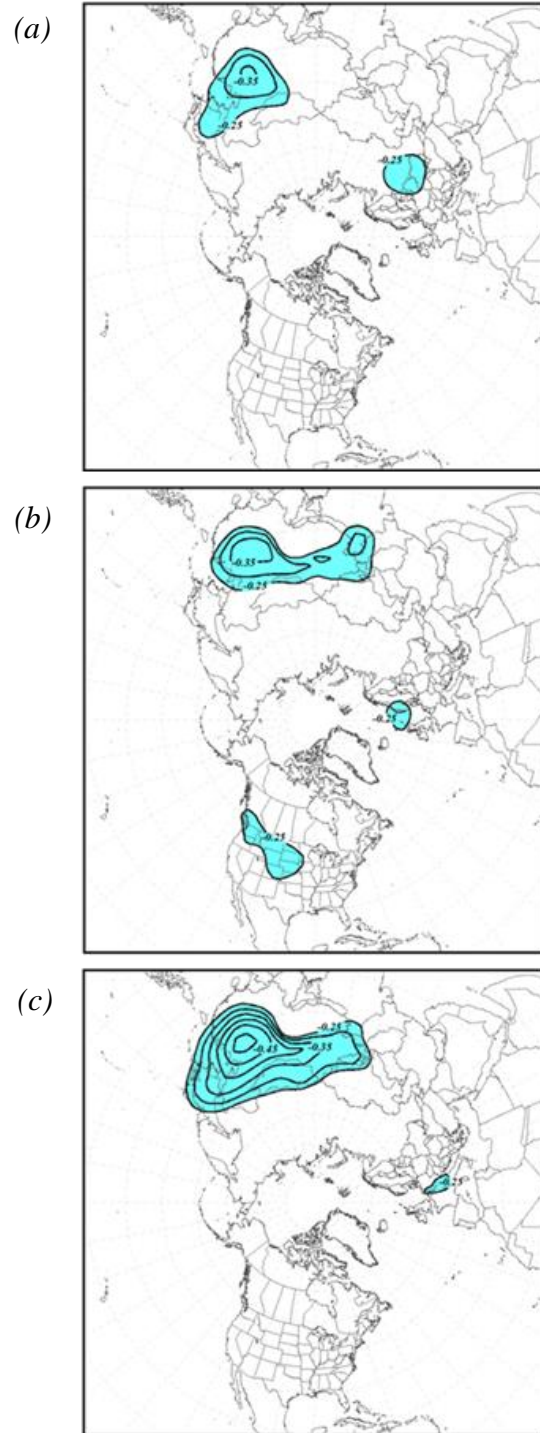


Figure 6: (a) Map of correlation between the daily average, December, 850-hPa temperature at each grid point (from 1948 to 2013) in the NCEP reanalysis data to the daily time series of normalized Northern Hemisphere cold pool area for each December day in that interval. Magnitudes of correlations significant at the 95% level are contoured and blue shaded every 0.05 beginning at 0.20. (b) As in (a), but for January days from 1948 to 2014. (c) As in (a), but for February days from 1948 to 2014. (From Martin 2015)

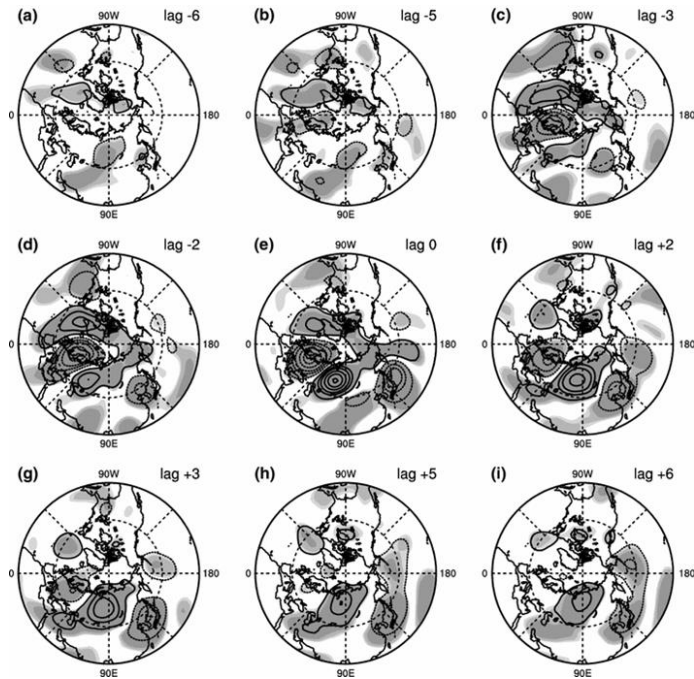


Figure 7: The 500 hPa geopotential height anomaly field for positive EU phase at lag -6 days (a), lag -5 days (b), lag -3 days (c), lag -2 days (d), lag 0 days (e), lag $+2$ days (f), lag $+3$ days (g), lag $+5$ days (h) and lag $+6$ days (i). *Solid contours* are positive and *dashed contours* are negative. The contour interval is 30 m. *Light and heavy shadings* indicate significant variation above 95 and 99 % confidence level, respectively. (From Wang and Zhang 2015)

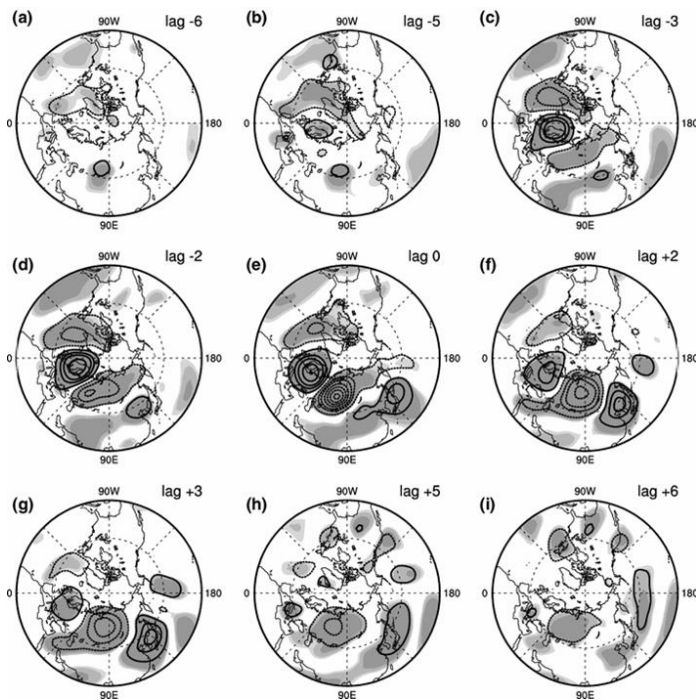


Figure 8: As for fig. 7, but for negative EU phase. (From Wang and Zhang 2015)

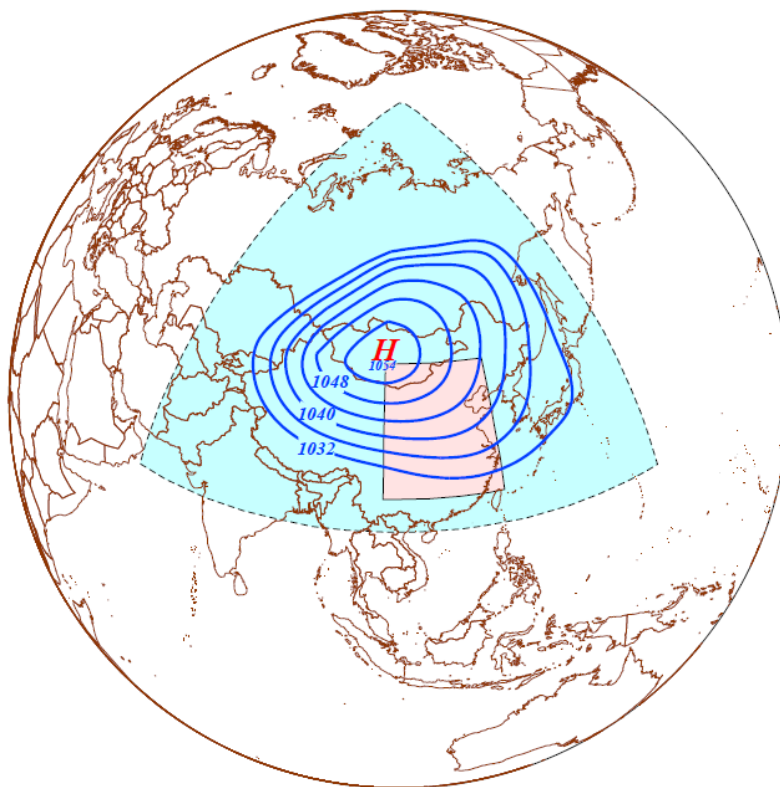


Figure 9: Highlighted in blue is the SMH index area. 'H' illustrates the center of the SMH surrounded by sea-level isobars contoured at 4 hPa intervals starting at 1032 hPa on 12Z - Jan. 8th, 1955. Highlighted in pink is the CI index area.

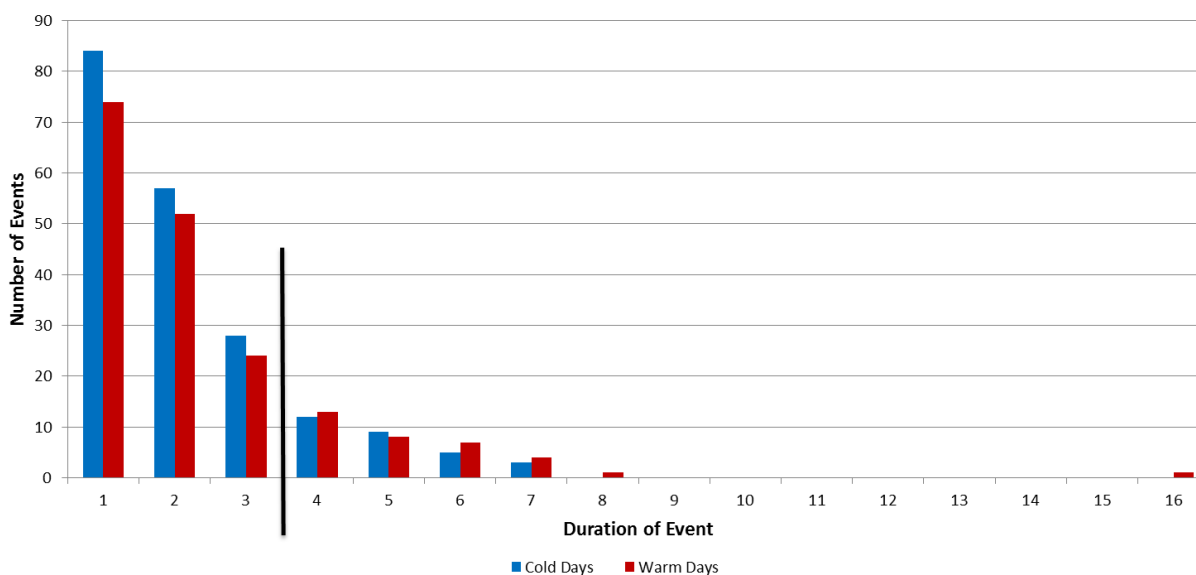


Figure 10: Cumulative distribution function of the duration of extreme warm (red) and cold (blue) events. Black line is drawn to indicate the chosen length criteria of 4 days or greater which represent the 66th (57th) percentile of extreme cold (warm) days.

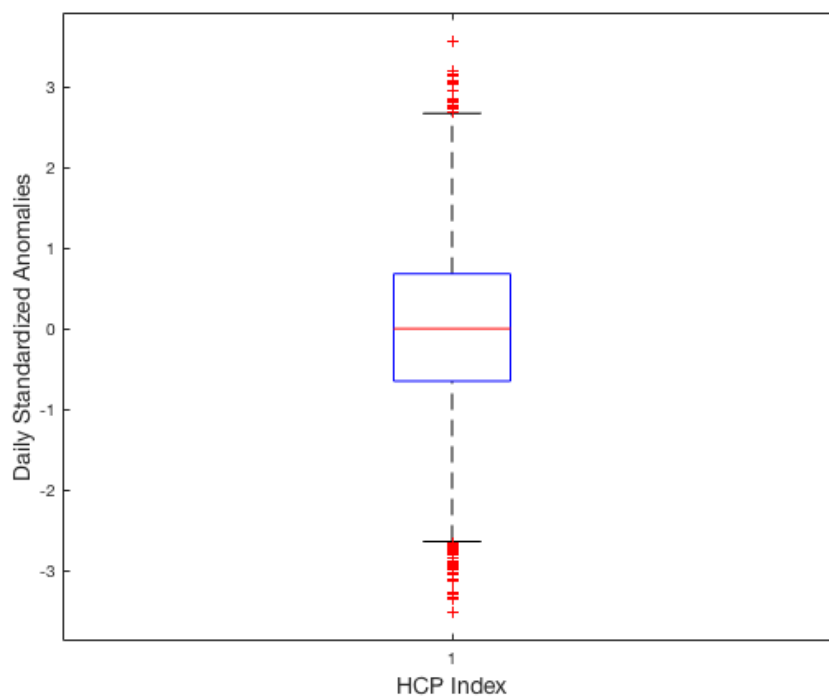


Figure 11: Data distribution of daily standardized anomalies for the HCP index from Nov. 1948 – Mar. 2013. See text for boxplot explanation.

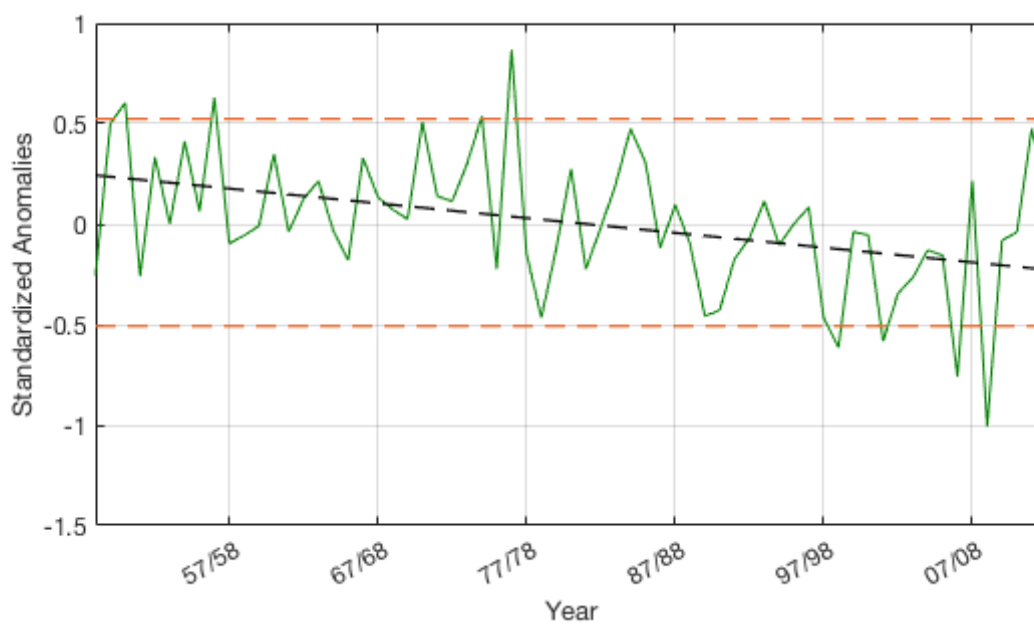


Figure 12: Time series of seasonal averaged HCP anomalies from Nov. 1948 – Mar. 2013. Dashed orange lines represent ± 1.5 standard deviations from the average. Black dashed line represents the linear trend of the time series.

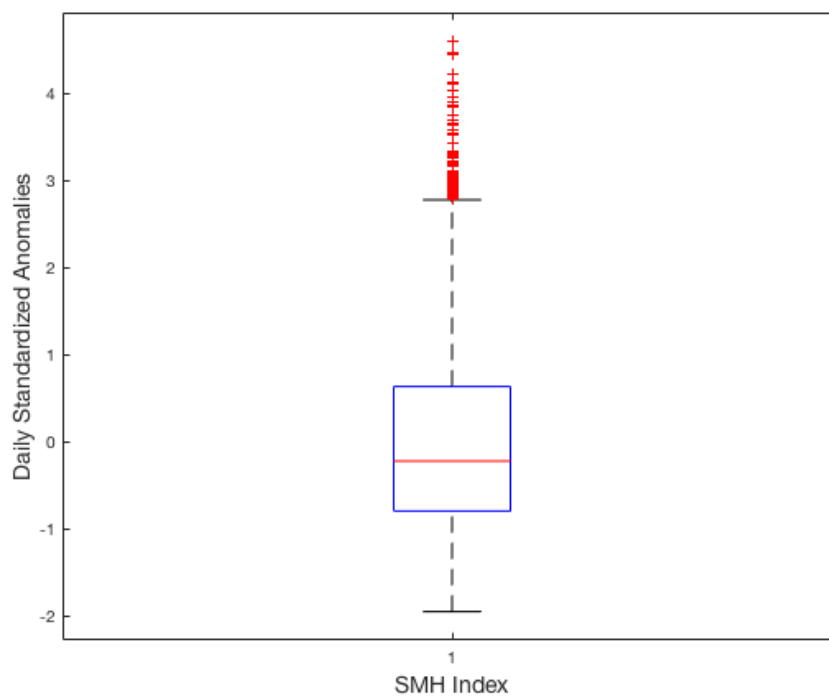


Figure 13: Data distribution of daily standardized anomalies for the SMH index from Nov. 1948 – Mar. 2013. See text for boxplot explanation.

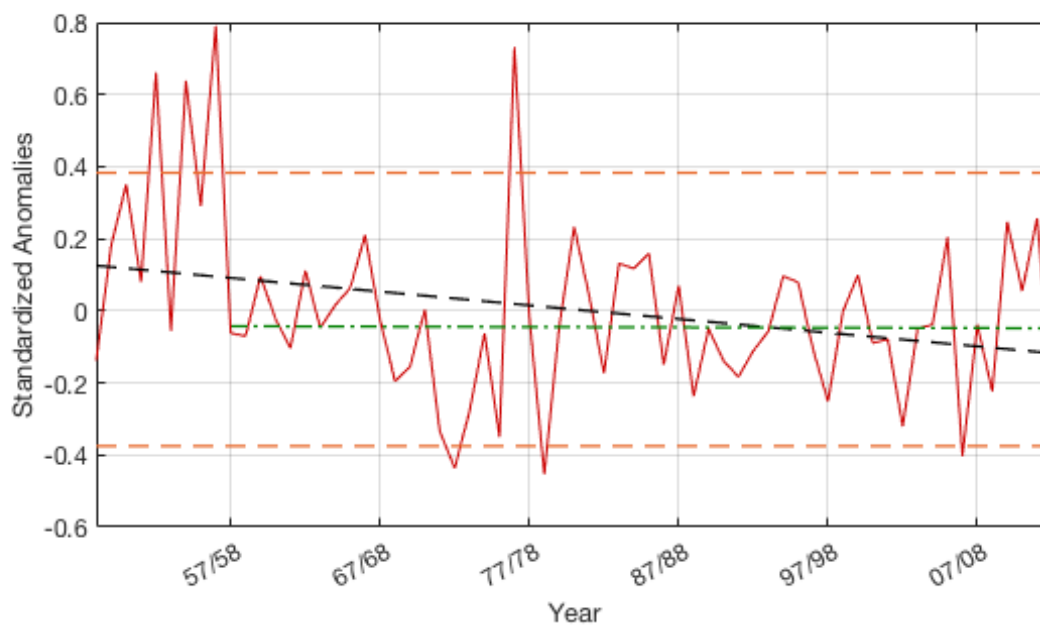


Figure 14: Time series of seasonal averaged SMH anomalies from Nov. 1948 – Mar. 2013. Dashed orange lines represent ± 1.5 standard deviations from the average. Black (green) dashed line represents the linear trend of the time series from 48/49-12/13 (57/58-12/13).

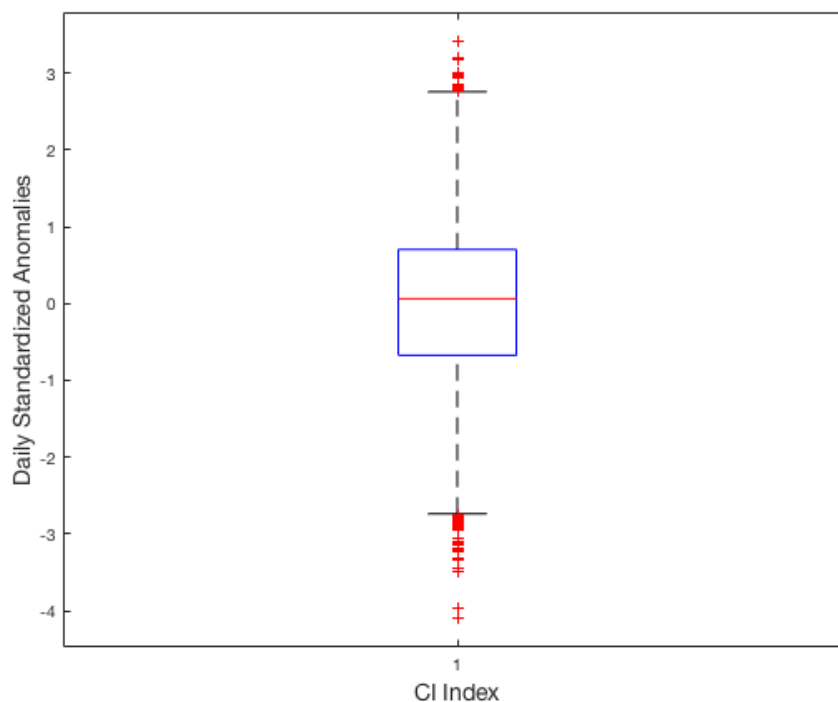


Figure 15: Data distribution of daily standardized anomalies for the CI index from Nov. 1948 – Mar. 2013. See text for boxplot explanation.

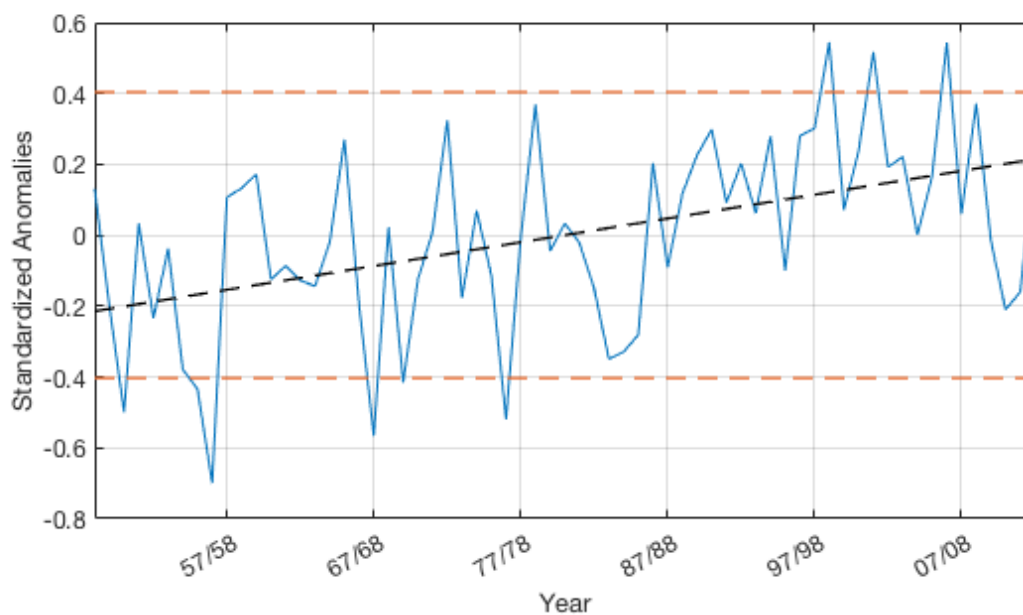


Figure 16: Time series of seasonal averaged CI anomalies from Nov. 1948 – Mar. 2013. Dashed orange lines represent ± 1.5 standard deviations from the average. Black dashed line represents the linear trend of the time series.

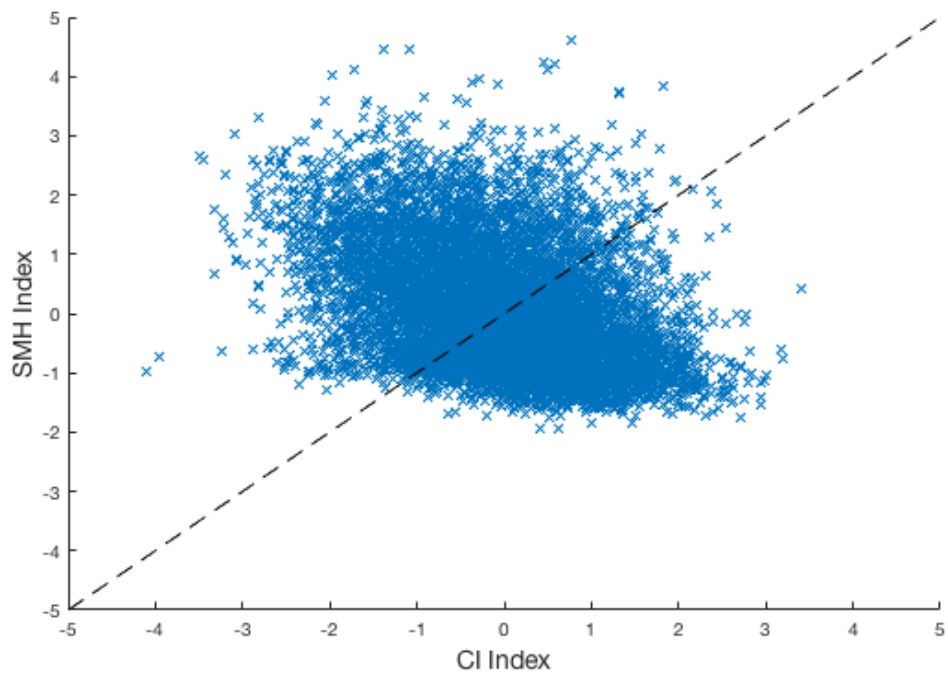


Figure 17: Scatterplot of daily standardized anomalies for the SMH and CI indices over all 66 cold seasons.

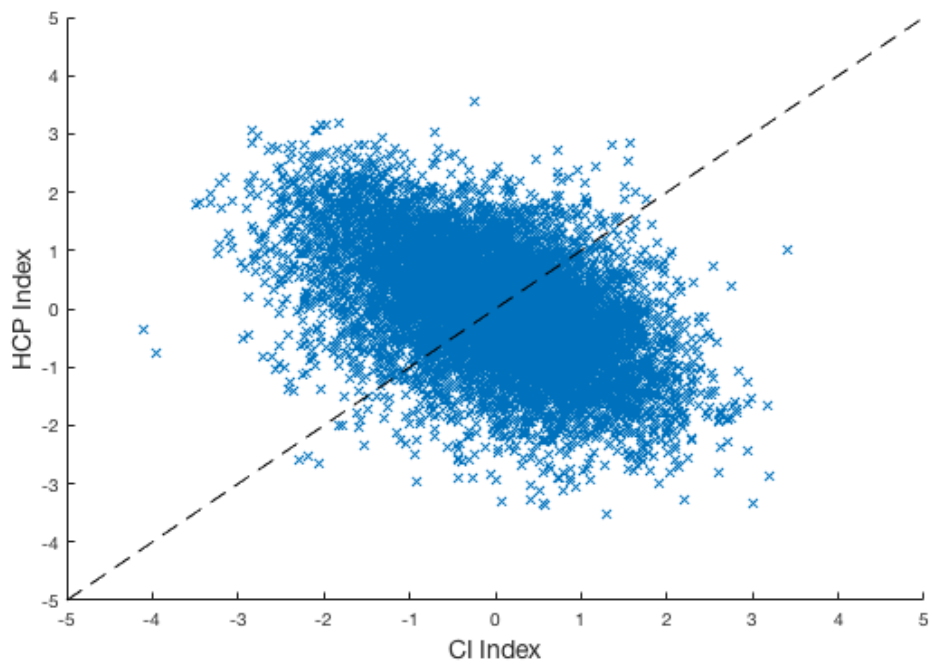


Figure 18: Scatterplot of daily standardized anomalies for the HCP and CI indices over all 66 cold seasons.

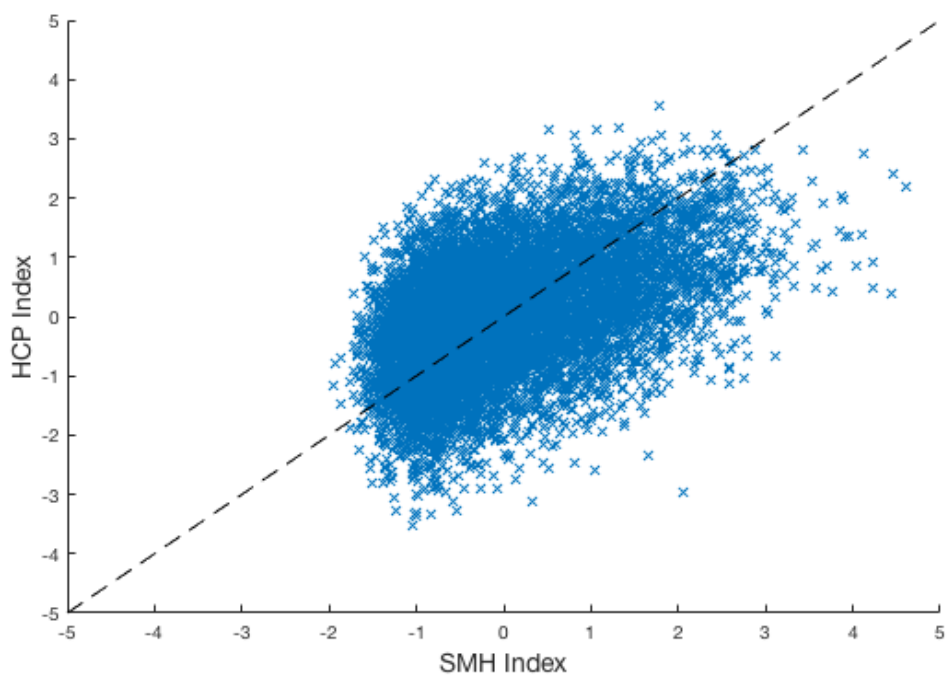


Figure 19: Scatterplot of daily standardized anomalies for the SMH and HCP indices over all 66 cold seasons.

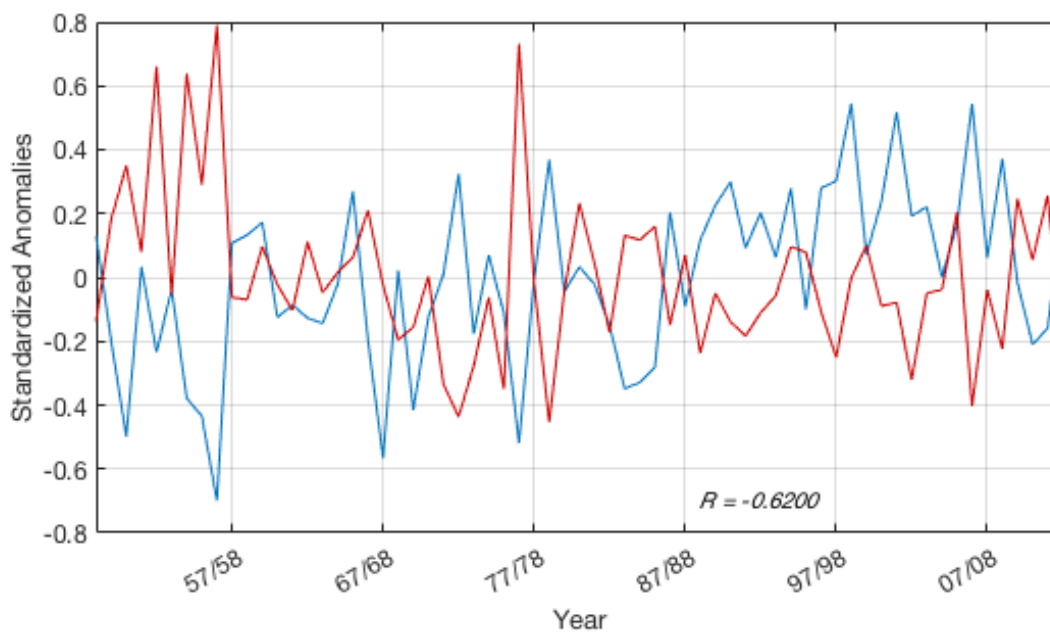


Figure 20: Time series of seasonal averaged CI (blue) and SMH (red) anomalies from Nov. 1948 – Mar. 2013. Correlation coefficient is indicated in italicized black (significant at the 99% confidence level).

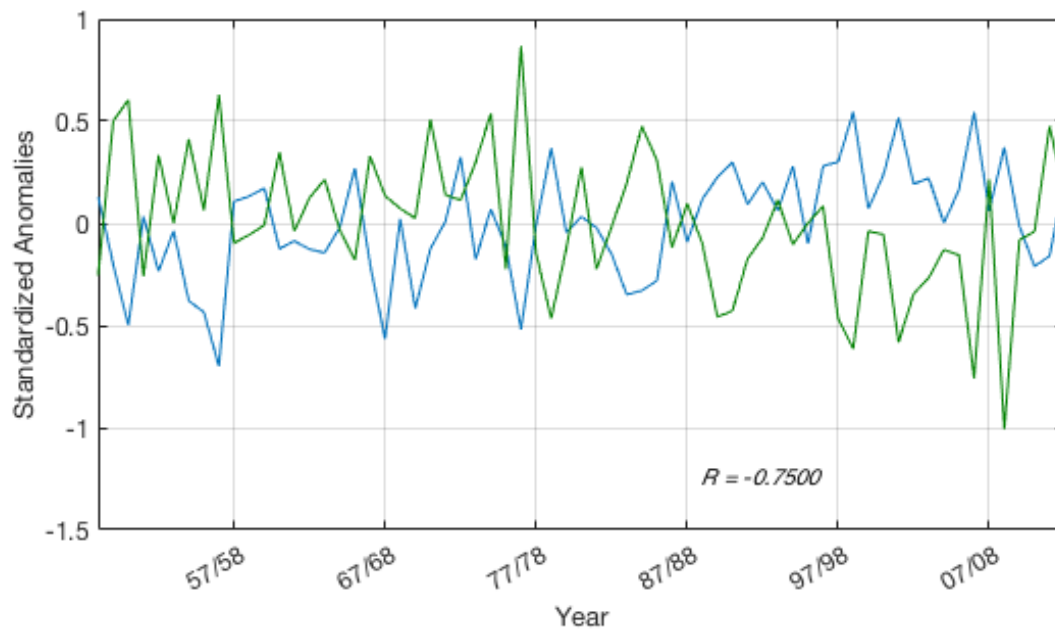


Figure 21: Time series of seasonal averaged CI (blue) and HCP (green) anomalies from Nov. 1948 – Mar. 2013. Correlation coefficient is indicated in italicized black (significant at the 99% confidence level).

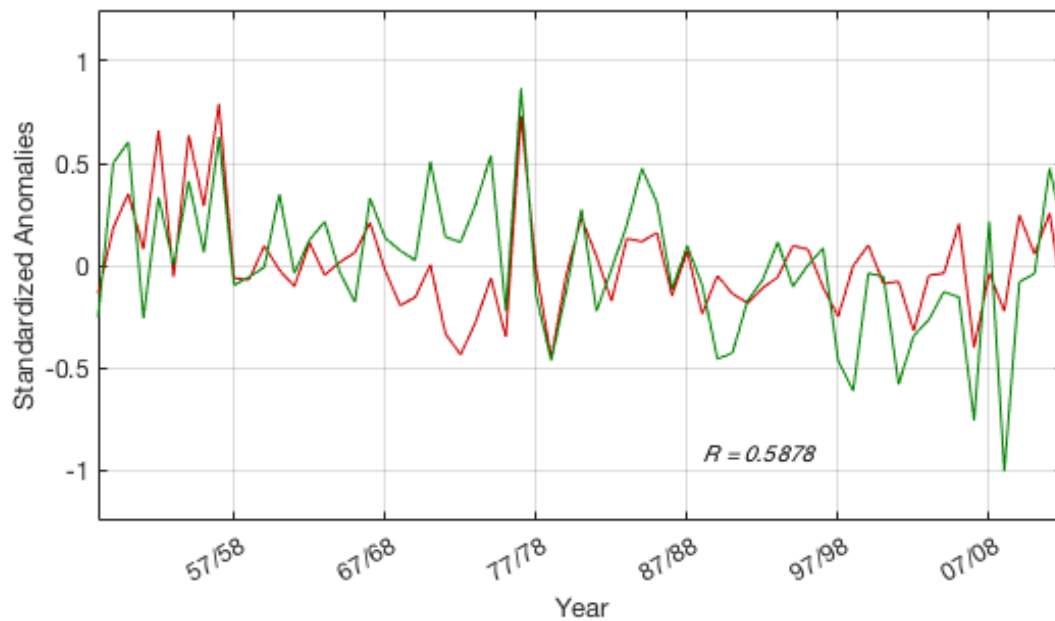


Figure 22: Time series of seasonal averaged HCP (green) and SMH (red) anomalies from Nov. 1948 – Mar. 2013. Correlation coefficient is indicated in italicized black (significant at the 99% confidence level).

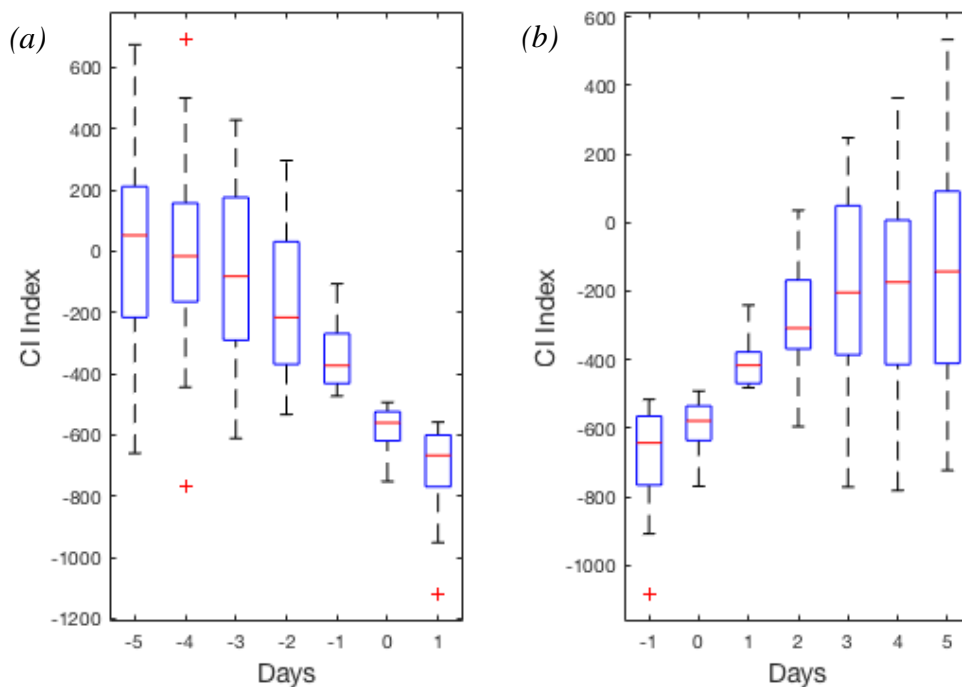


Figure 23: Composite of 29 extreme and extended cold events. (a) Data distribution of the onset period for the CI index. (b) As for Fig. 23a, but for the decay period.

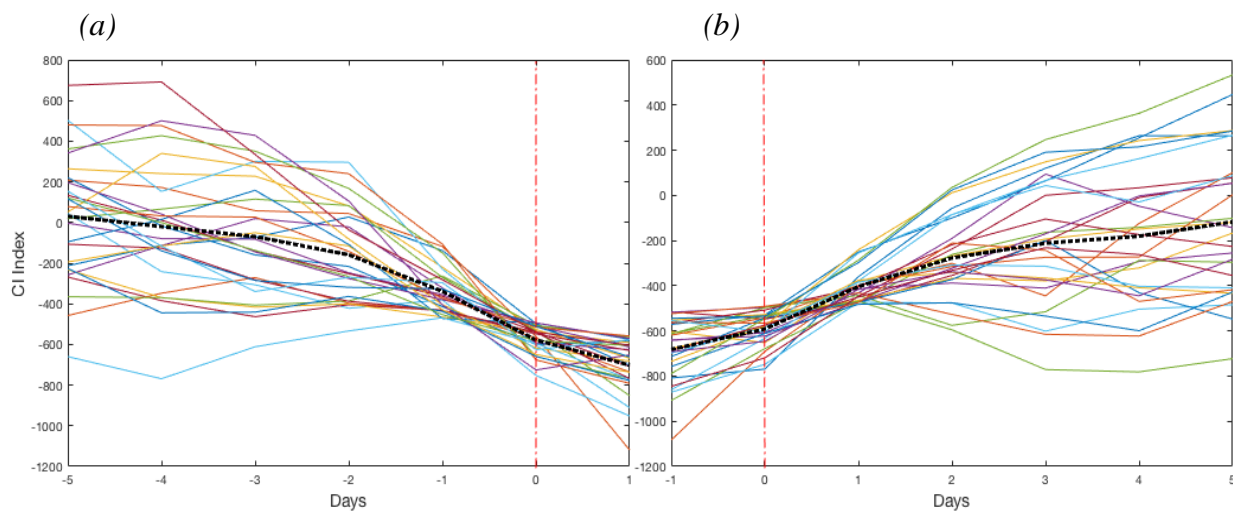


Figure 24: Composite of 29 extreme and extended cold events. (a) Time series of the onset period for the CI index. (b) As for Fig. 24a but for the decay period.

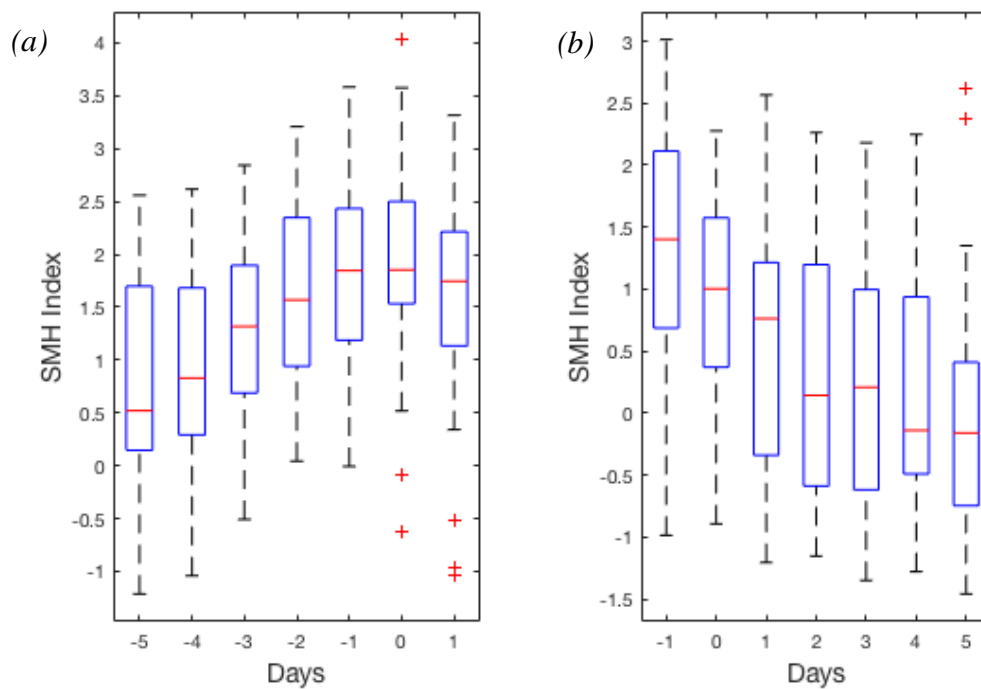


Figure 25: Composite of 29 extreme and extended cold events. (a) Data distribution of the onset period for the SMH index. (b) As for Fig. 25a but for the decay period.

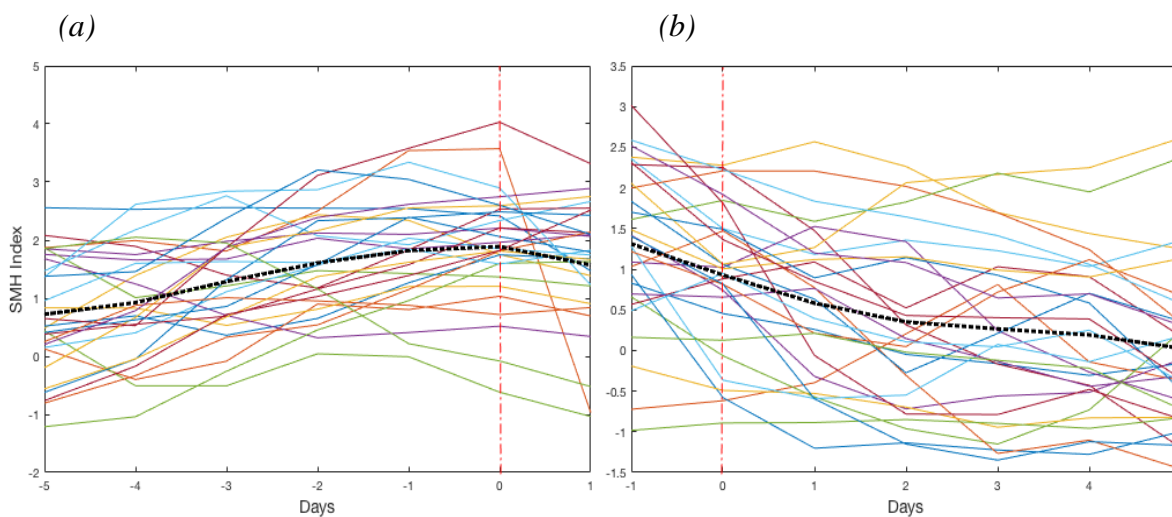


Figure 26: Composite of 29 extreme and extended cold events. (a) Time series of the onset period for the SMH index. (b) As for Fig. 26a but for the decay period.

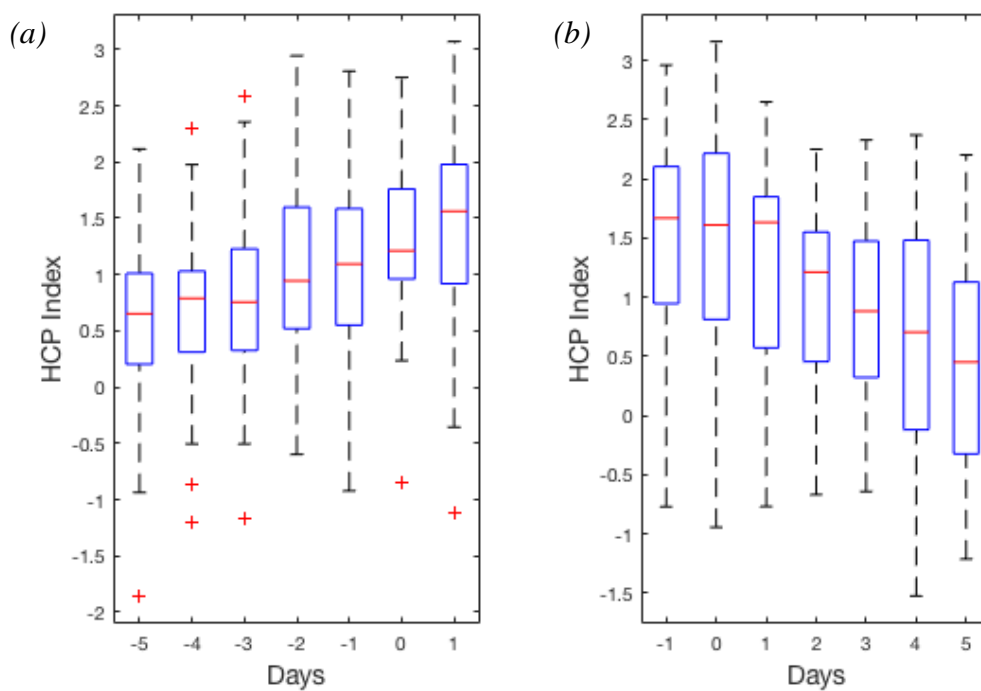


Figure 27: Composite of 29 extreme and extended cold events. (a) Data distribution of the onset period for the HCP index. (b) As for Fig. 27a but for the decay period.

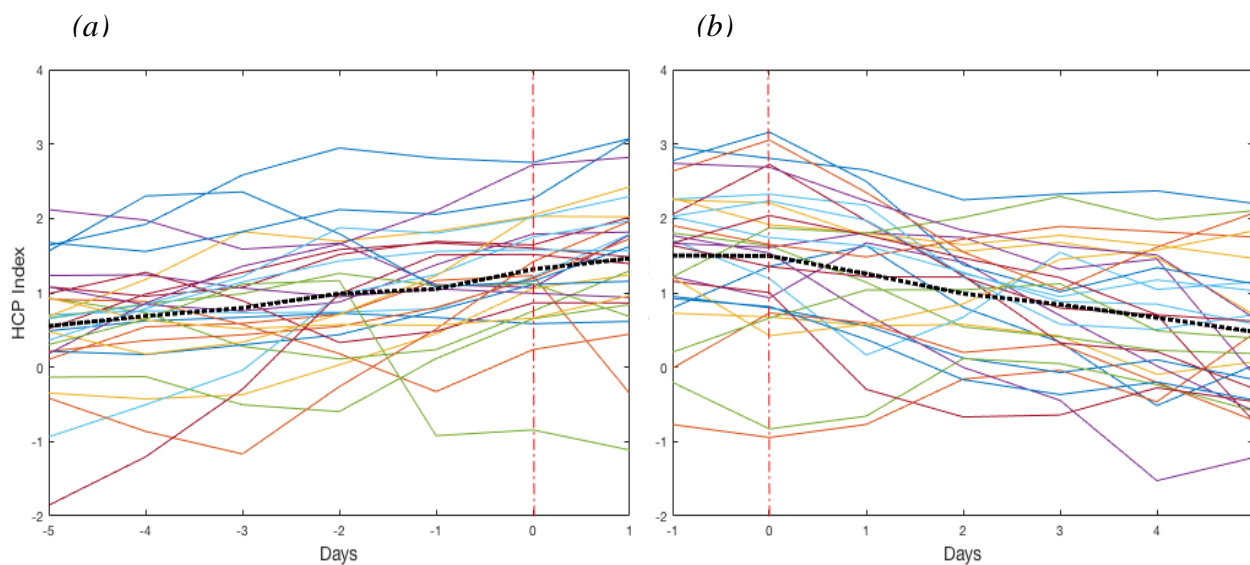


Figure 28: Composite of 29 extreme and extended cold events. (a) Time series of the onset period for the HCP index. (b) As for Fig. 28a but for the decay period.

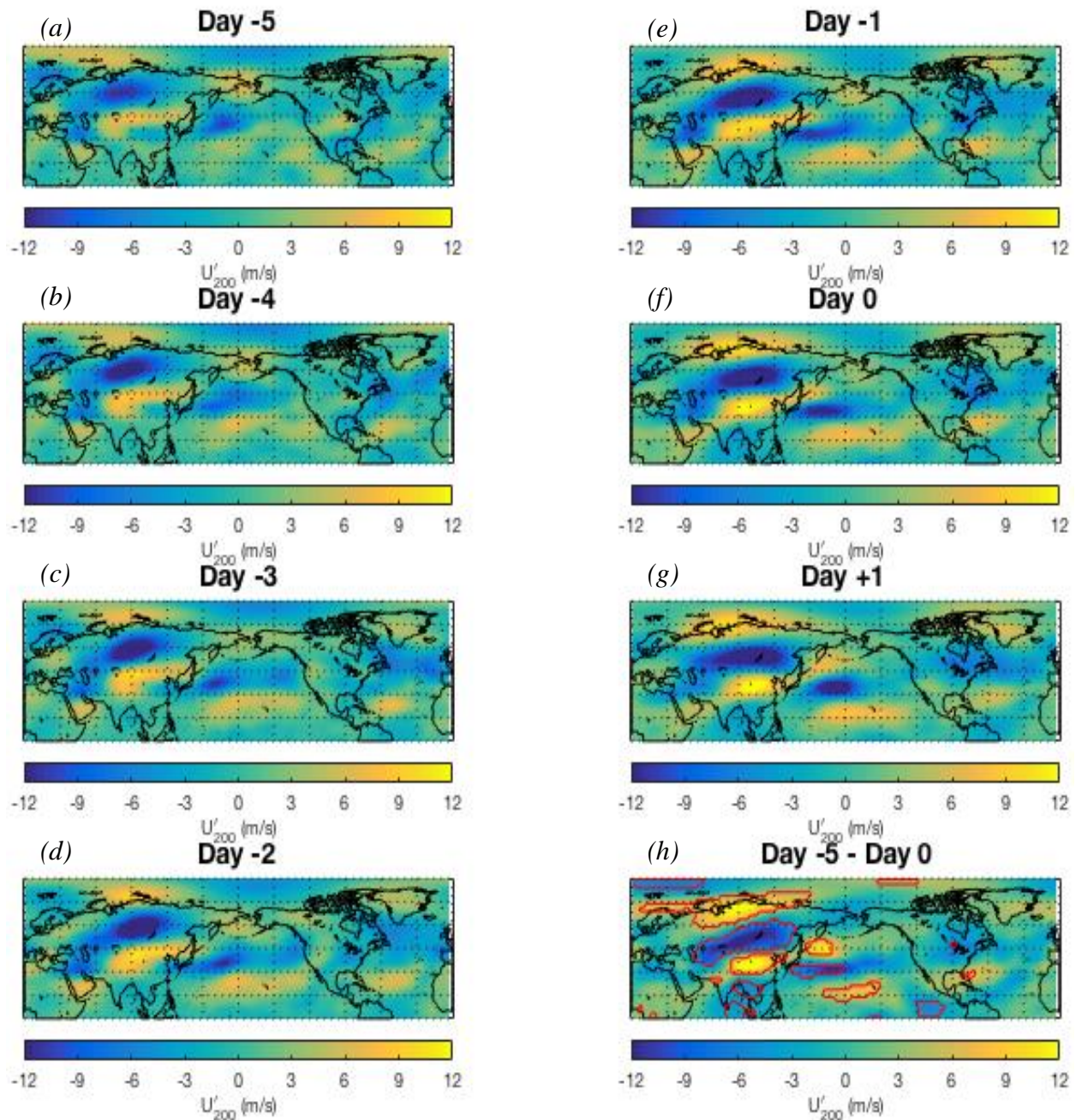


Figure 29: (a-g) Composite of 200-hPa zonal wind anomalies for each day of the onset period of 29 extreme and extended cold events. (h) Change in magnitude of zonal wind anomalies from day -5 to day 0. Red contours represent the 95% confidence level.

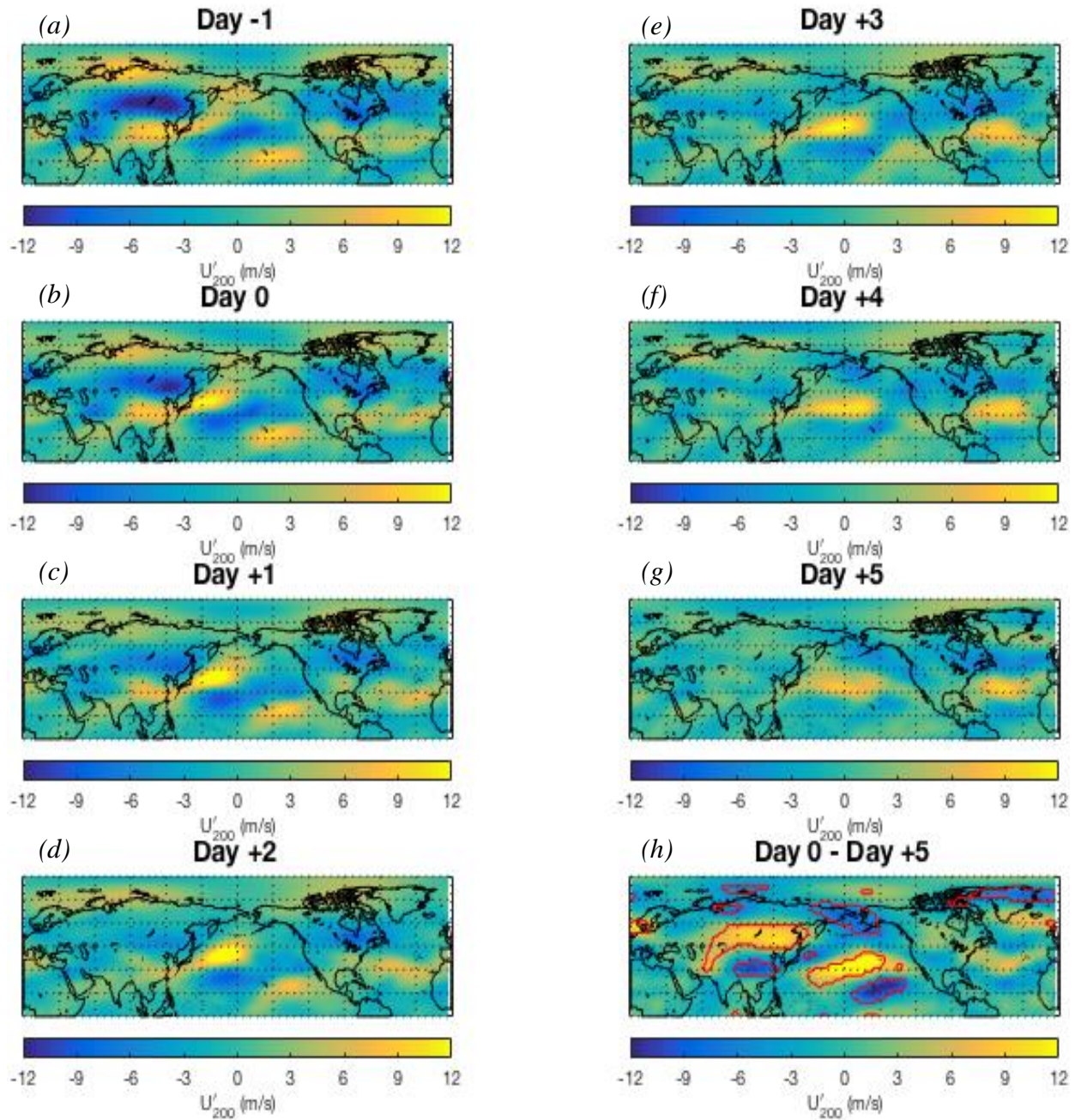


Figure 30: (a-g) Composite of 200-hPa zonal wind anomalies for each day of the decay period of 29 extreme and extended cold events. (h) Change in magnitude of zonal wind anomalies from day 0 to day +5. Red contours represent the 95% confidence level.

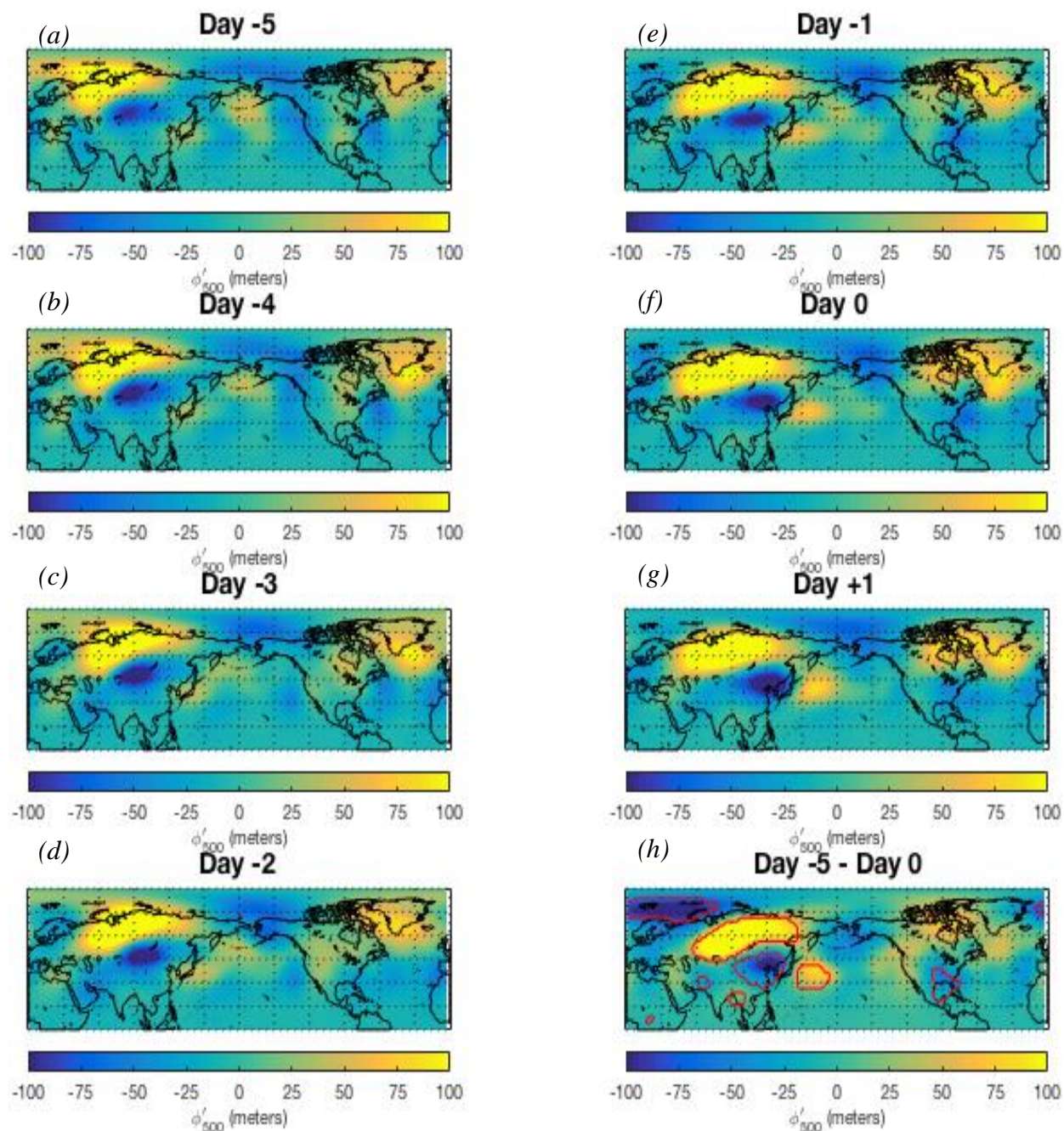


Figure 31: As for Fig. 29, but for composite of 500-hPa height anomalies.

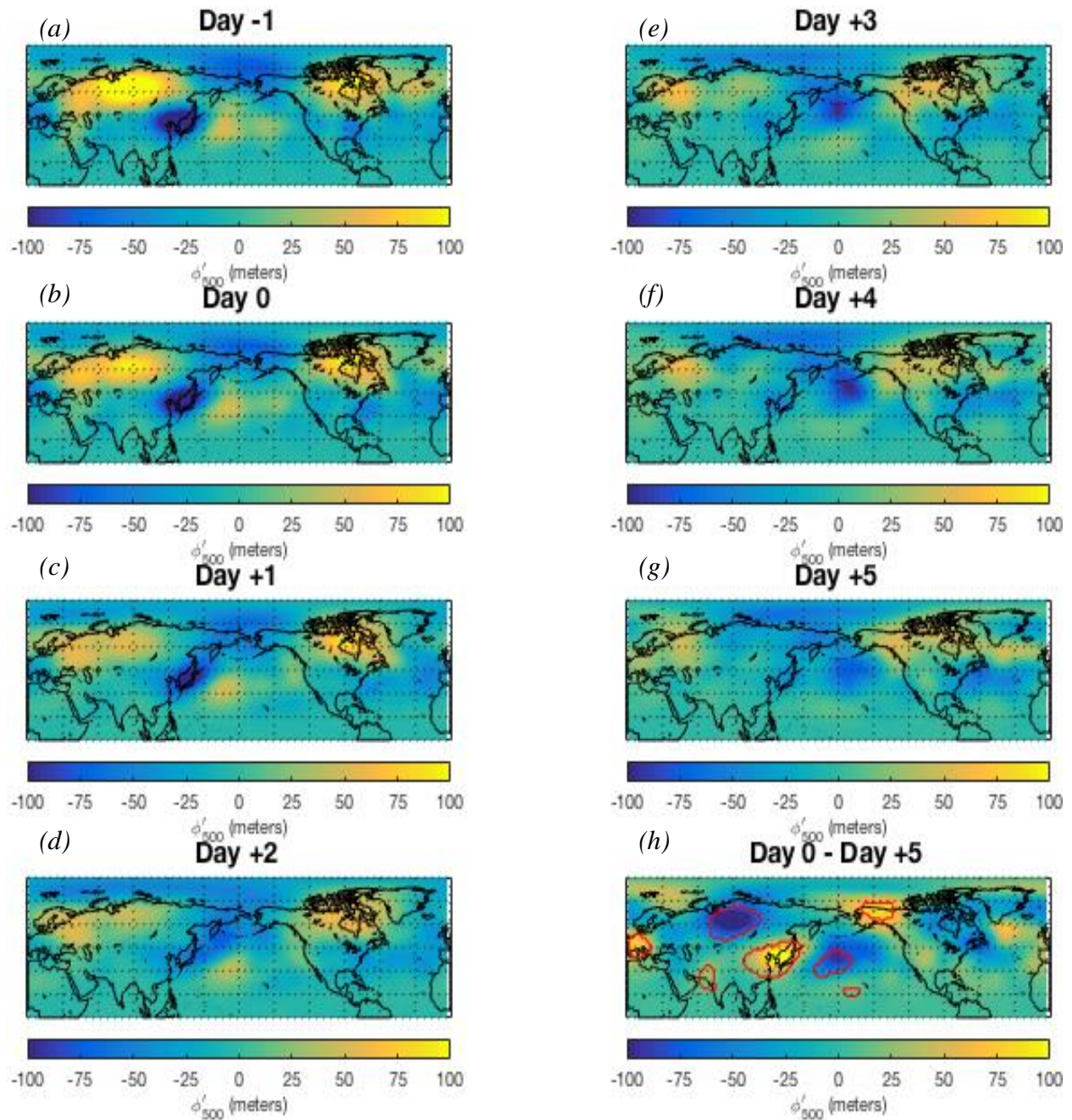


Figure 32: As for Fig. 30, but for composite of 500-hPa height anomalies.

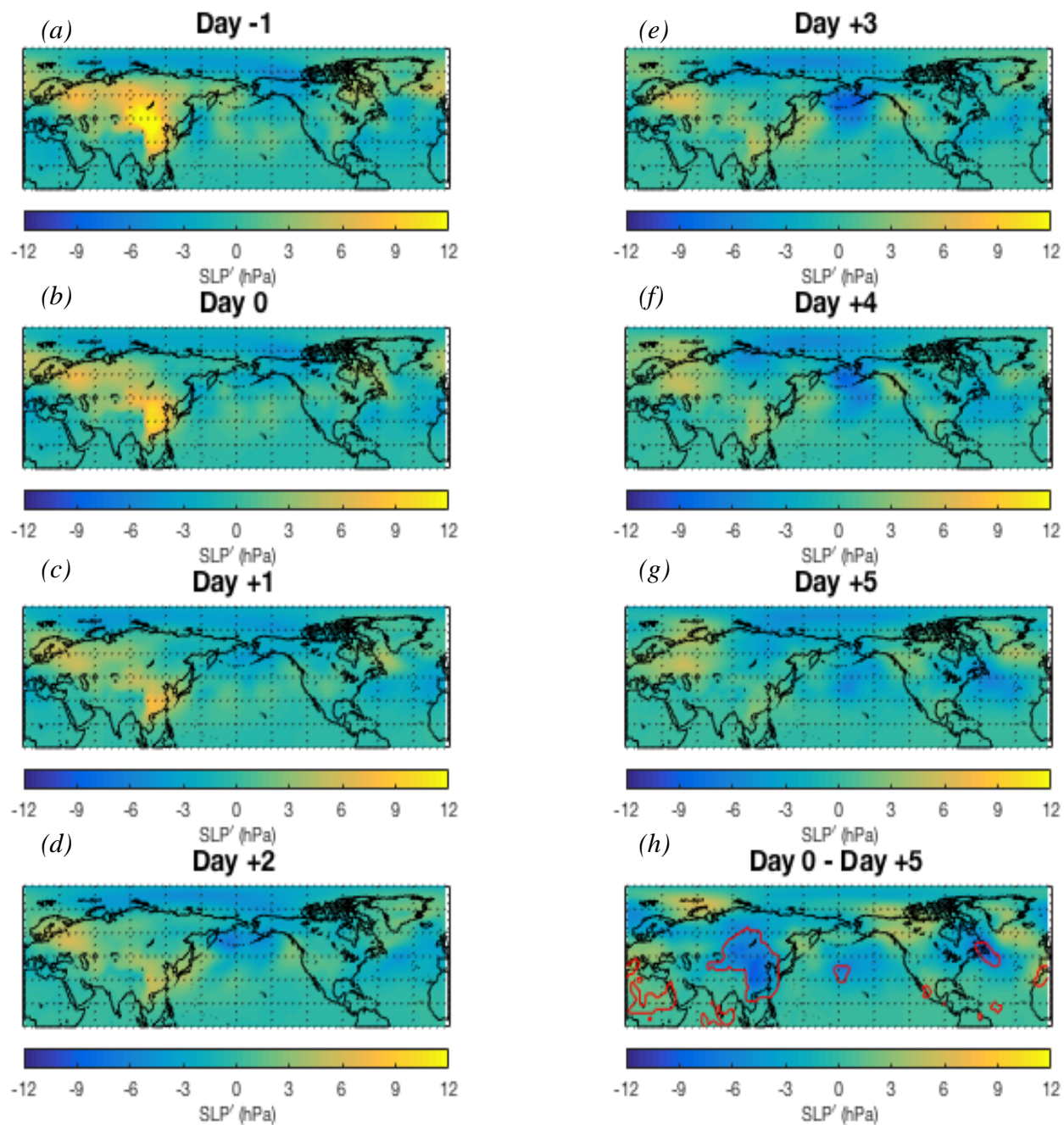


Figure 34: As for Fig. 30, but for composite of sea-level pressure anomalies.

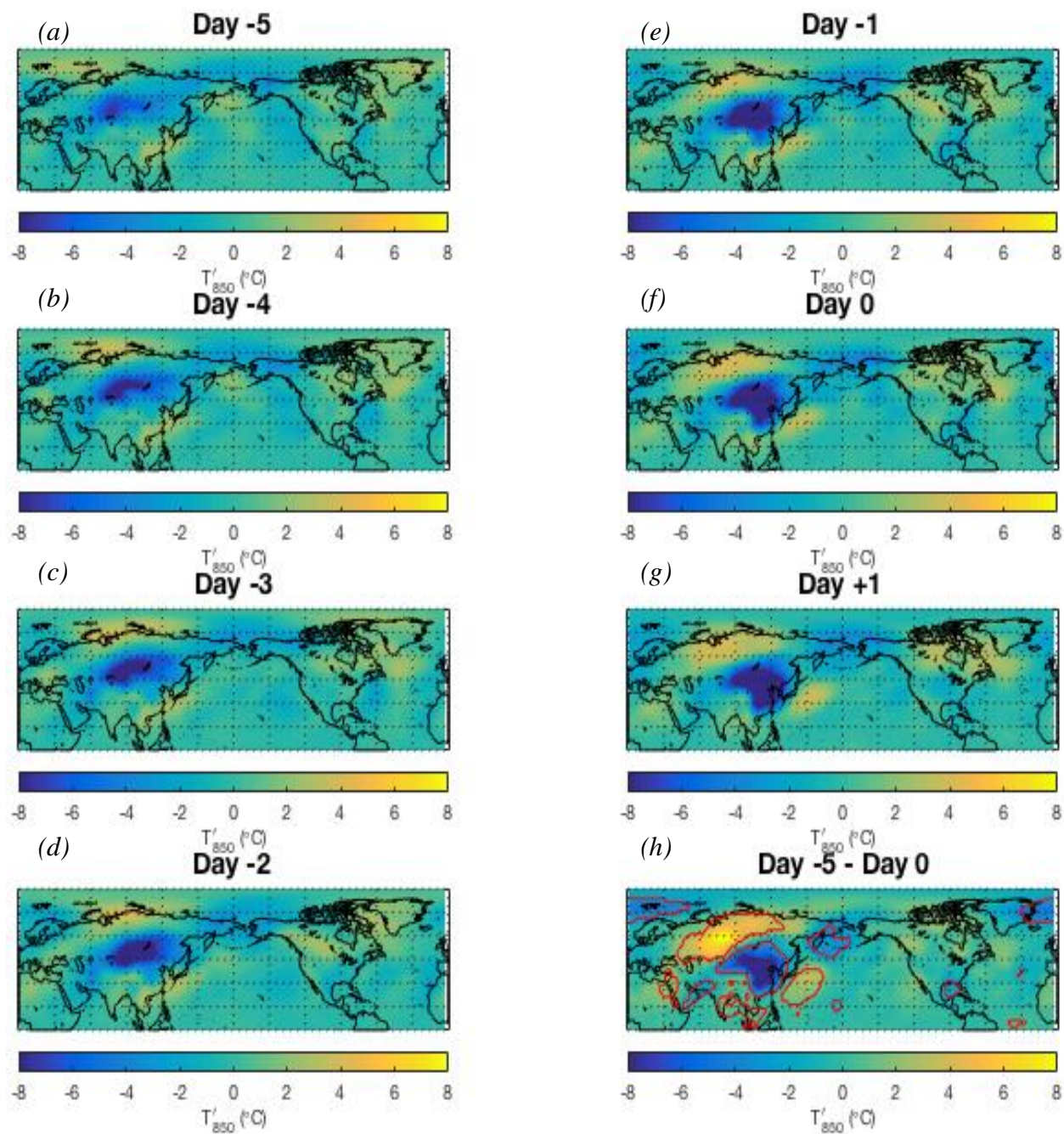


Figure 35: As for Fig. 29, but for composite 850-hPa temperature anomalies.

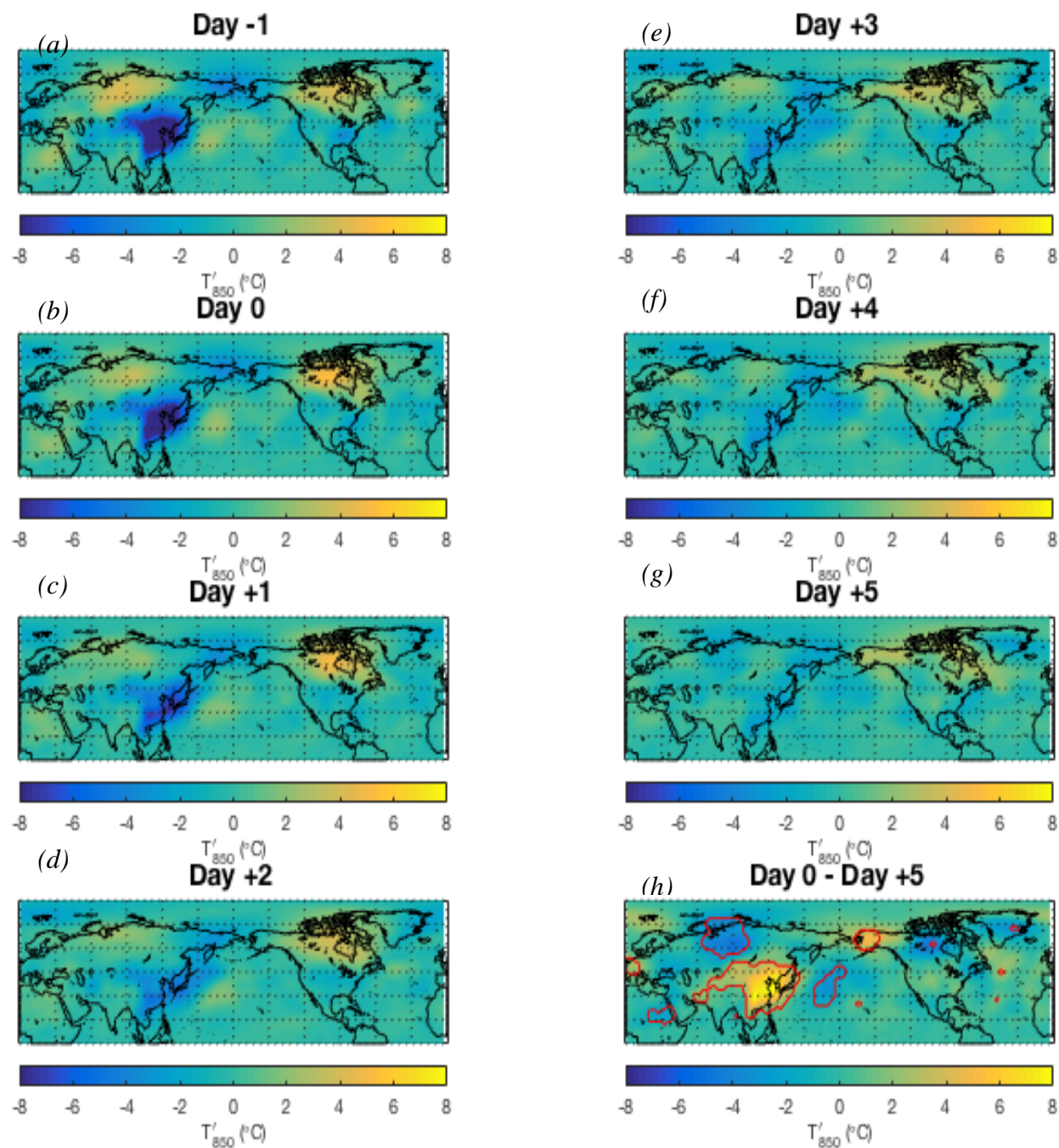


Figure 36: As for Fig. 30, but for composite of 850-hPa temperature anomalies.

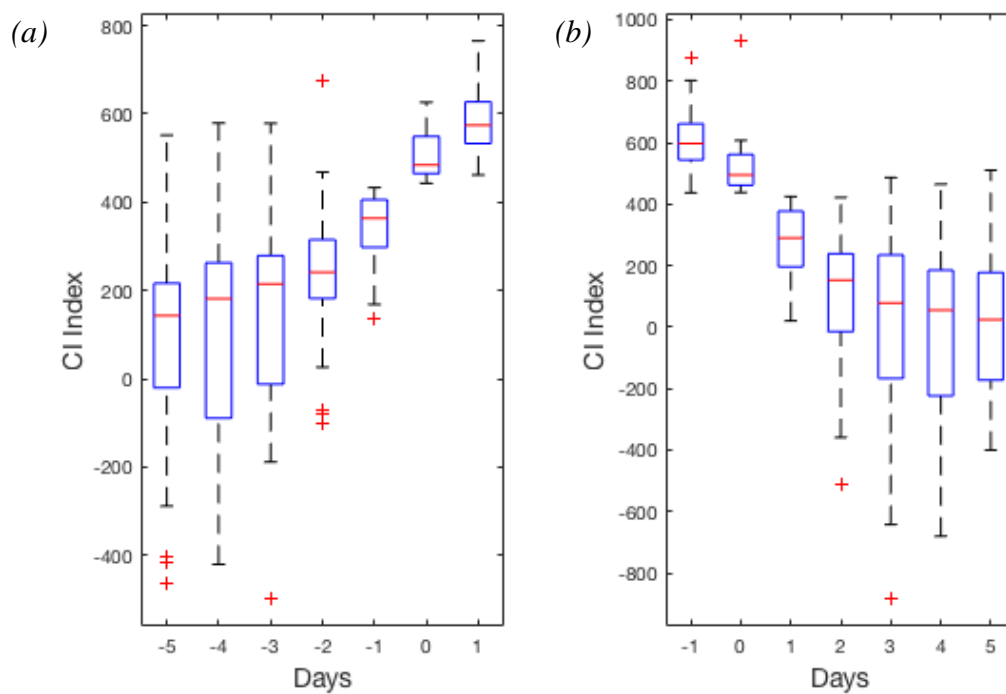


Figure 37: Composite of 34 extreme and extended warm events. (a) Data distribution of the onset period for the CI index. (b) As for Fig. 37a, but for the decay period.

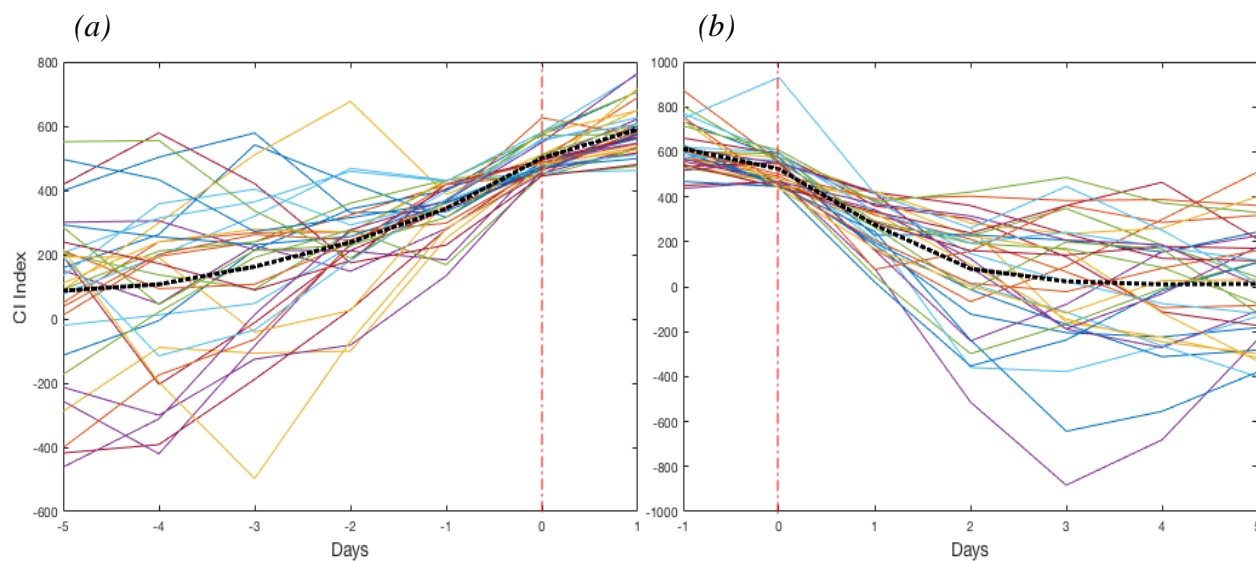


Figure 38: Composite of 34 extreme and extended warm events. (a) Time series of the onset period for the CI index. (b) As for Fig. 38a but for the decay period.

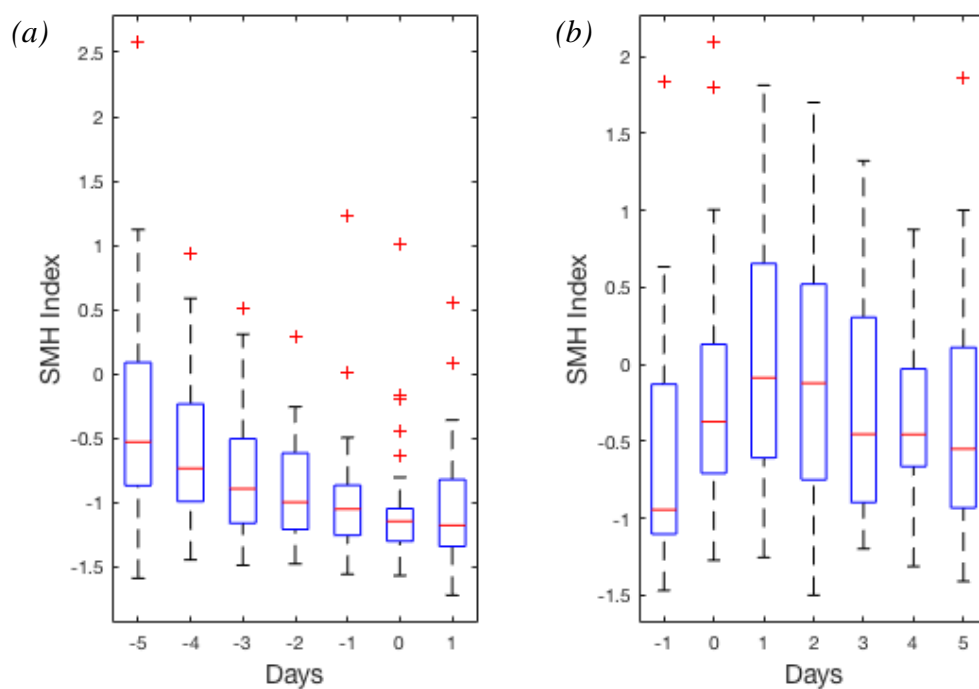


Figure 39: Composite of 34 extreme and extended warm events. (a) Data distribution of the onset period for the SMH index. (b) As for Fig. 39a, but for the decay period.

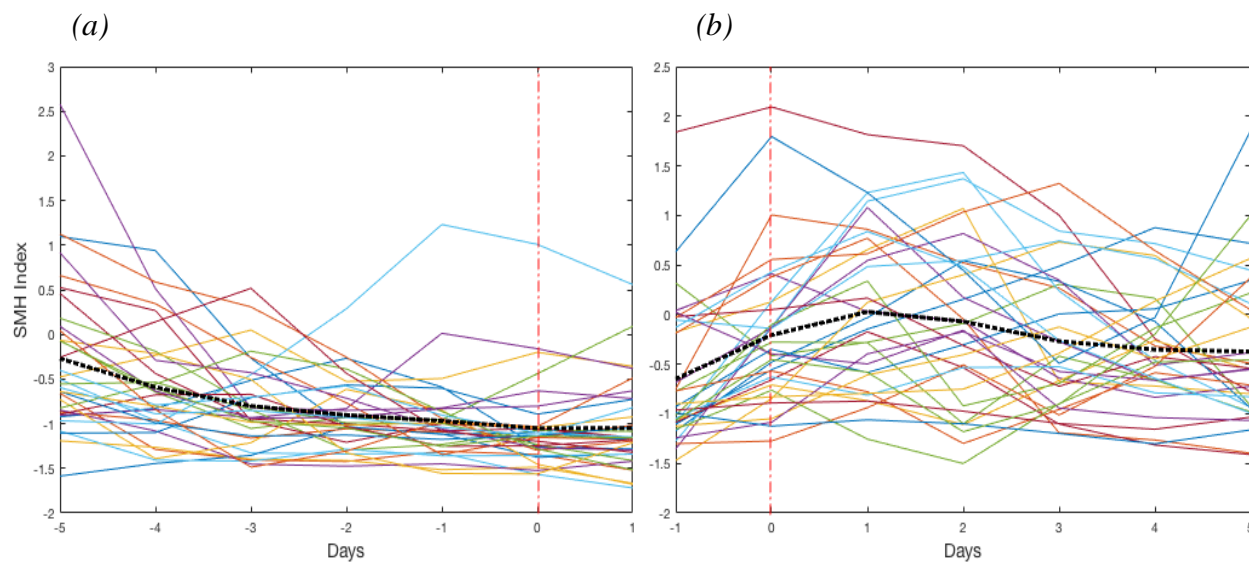


Figure 40: Composite of 34 extreme and extended warm events. (a) Time series of the onset period for the SMH index. (b) As for Fig. 40a but for the decay period.

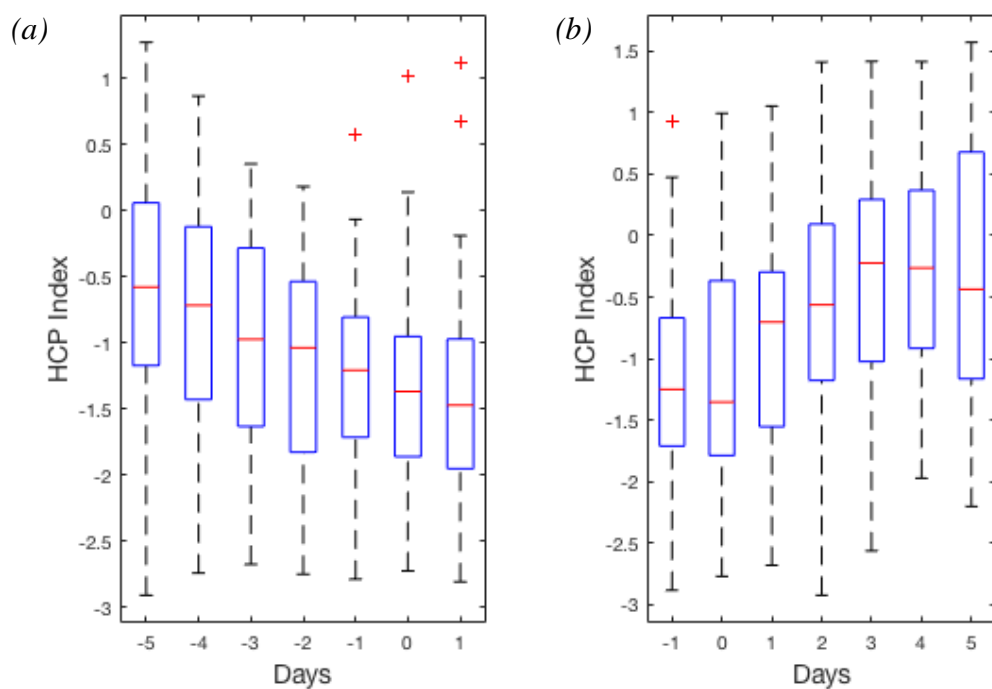


Figure 41: Composite of 34 extreme and extended warm events. (a) Data distribution of the onset period for the HCP index. (b) As for Fig. 41a, but for the decay period.

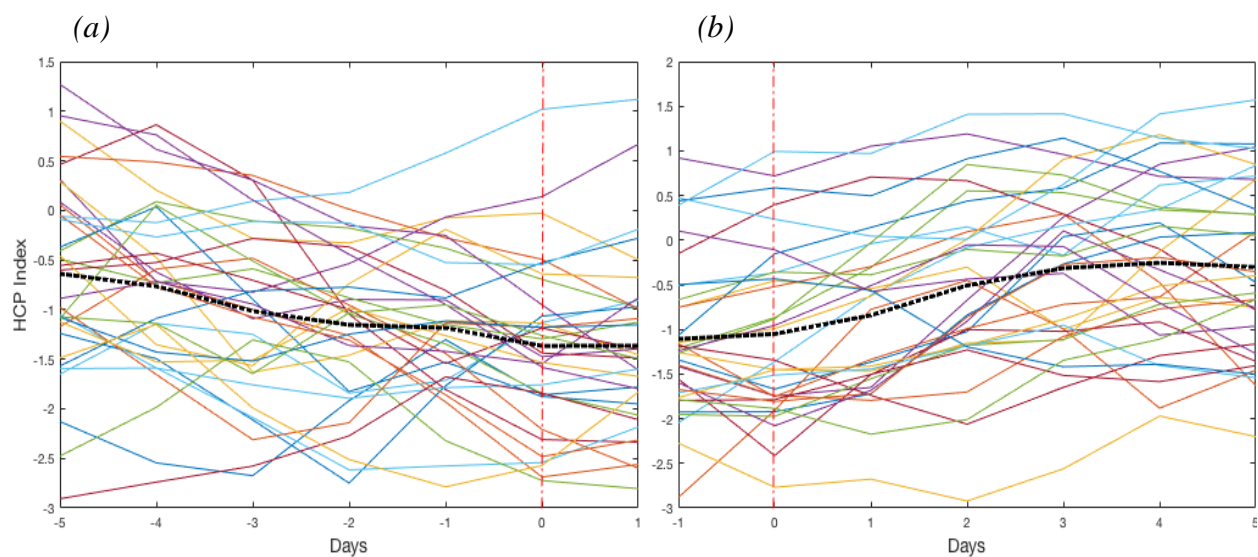


Figure 42: Composite of 34 extreme and extended warm events. (a) Time series of the onset period for the HCP index. (b) As for Fig. 42a but for the decay period.

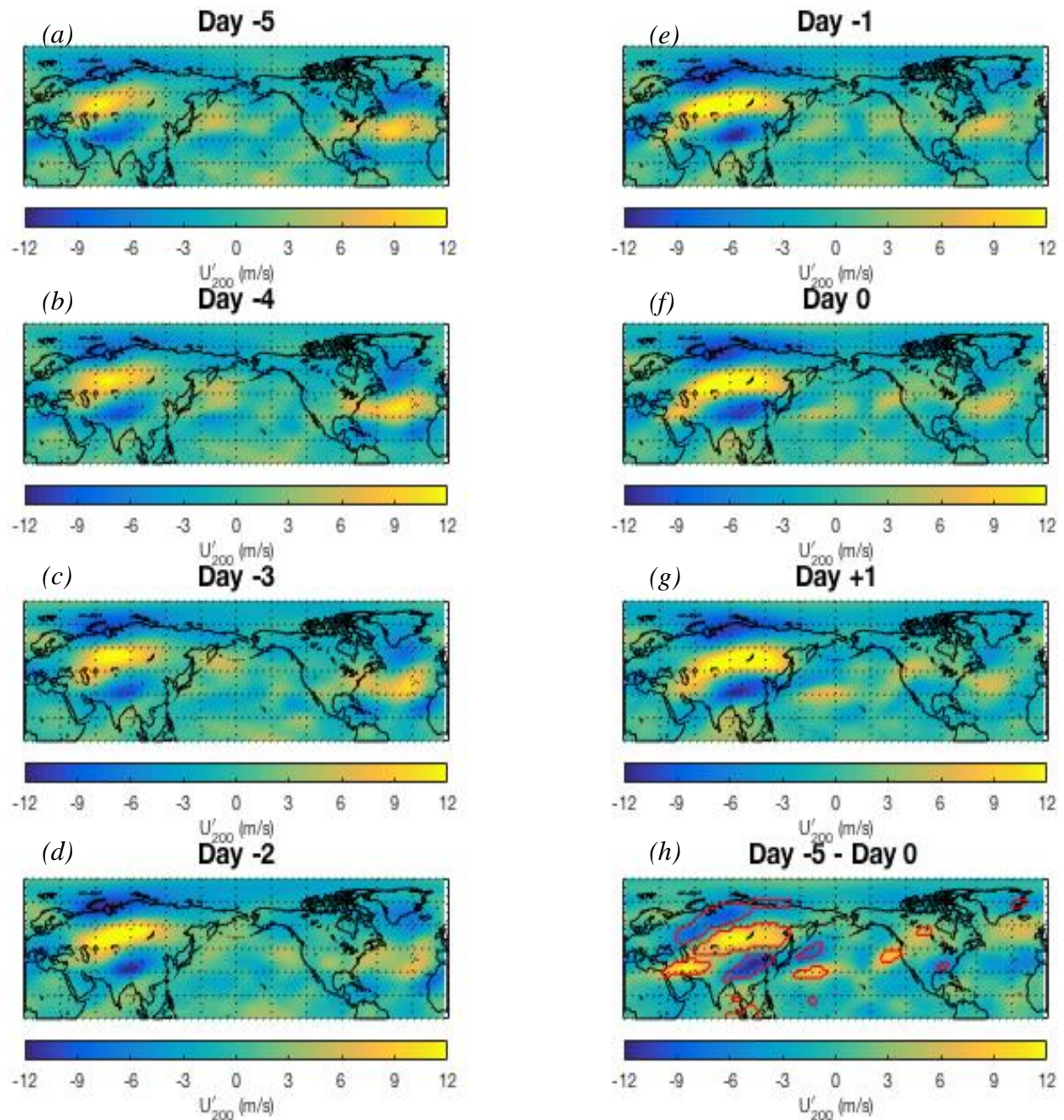


Figure 43: (a-g) Composite of 200-hPa zonal wind anomalies for each day of the onset period of 34 extreme and extended warm events. (h) Change in magnitude of zonal wind anomalies from day -5 to day 0. Red contours represent the 95% confidence level.

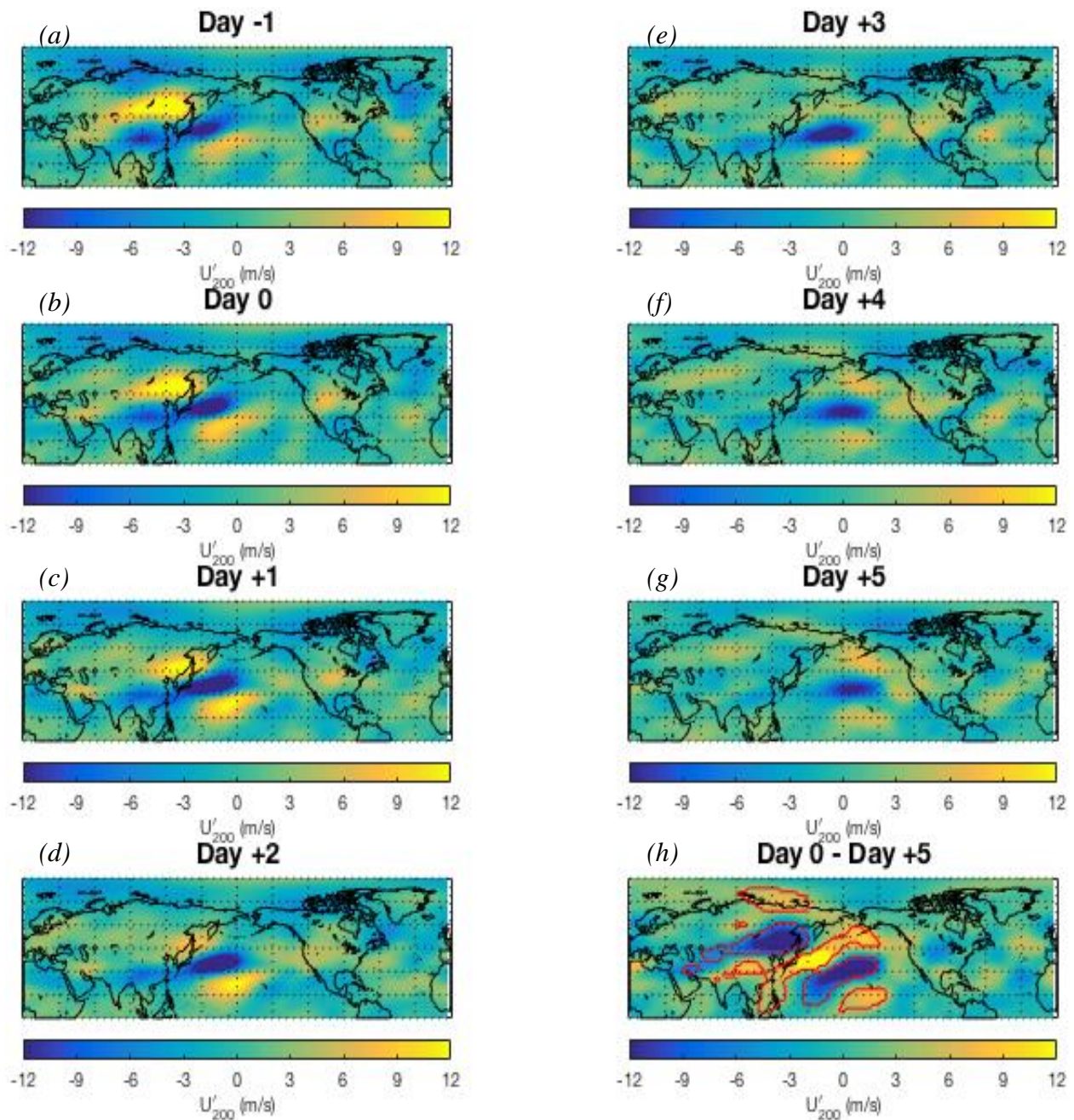


Figure 44: (a-g) Composite of 200-hPa zonal wind anomalies for each day of the decay period of 34 extreme and extended warm events. (h) Change in magnitude of zonal wind anomalies from day 0 to day +5. Red contours represent the 95% confidence level.

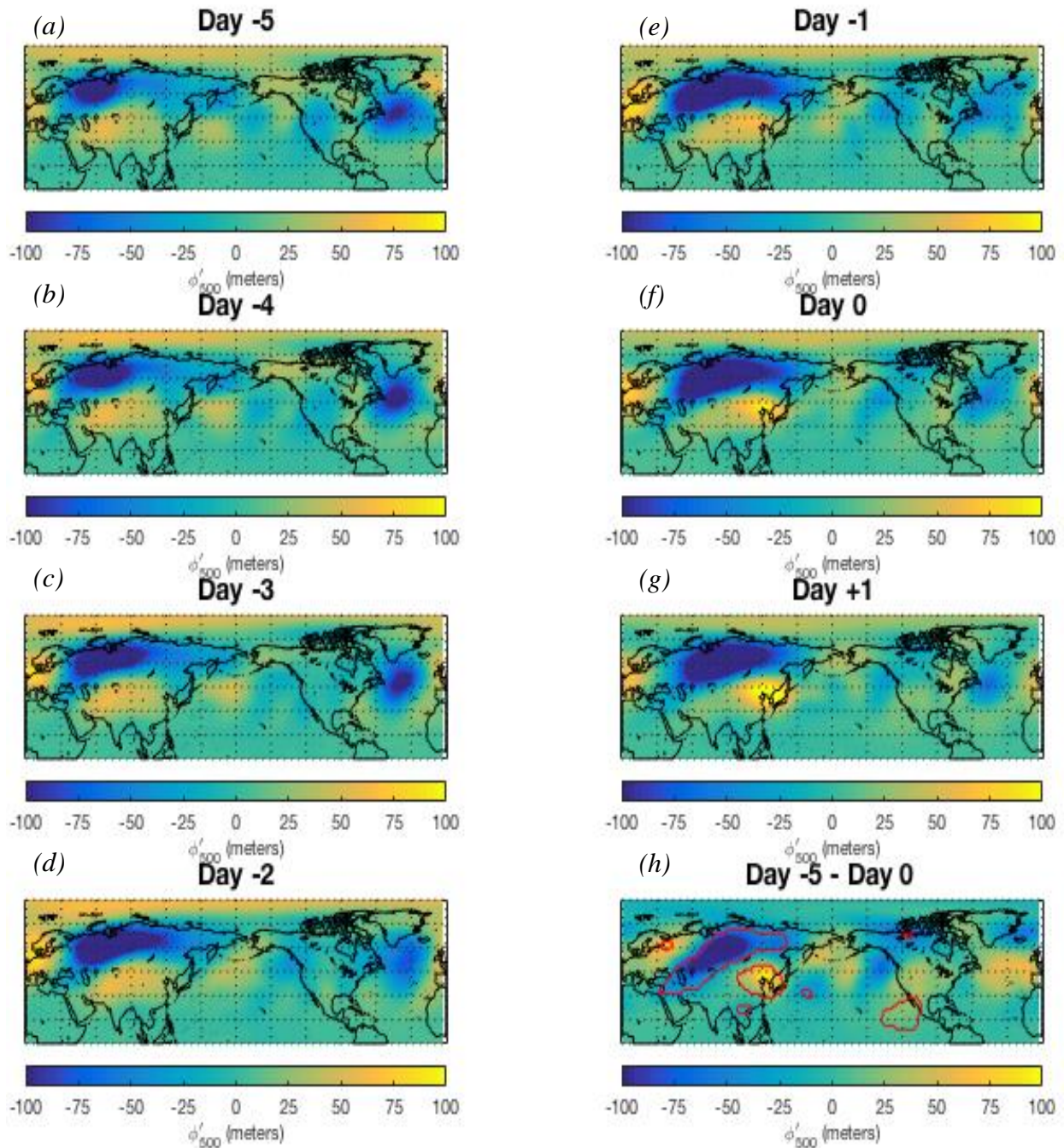


Figure 45: As for Fig. 43, but for composite of 500-hPa height anomalies.

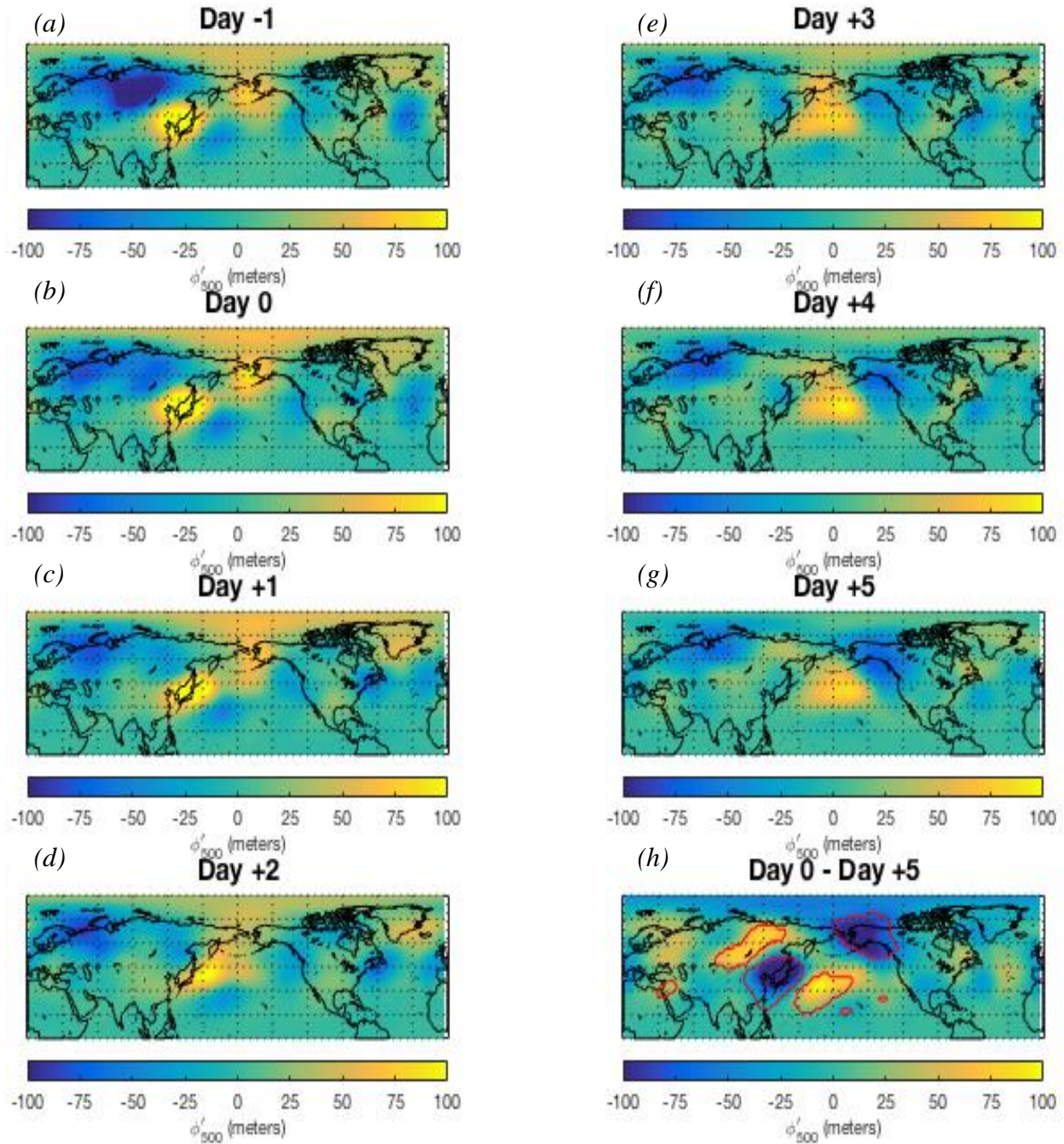


Figure 46: As for Fig. 44, but for composite of 500-hPa height anomalies.

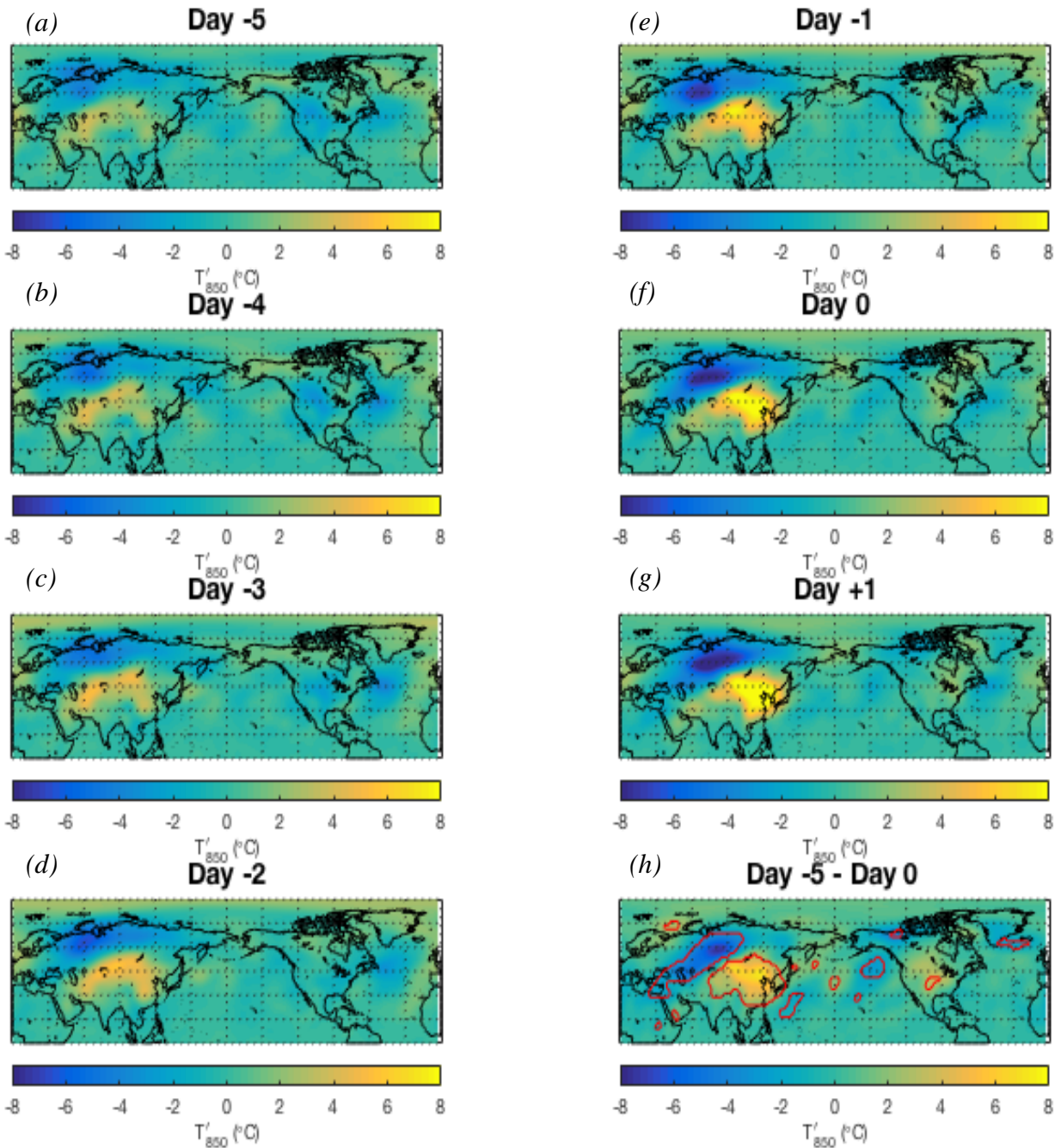


Figure 49: As for Fig. 43, but for composite of 850-hPa temperature anomalies.

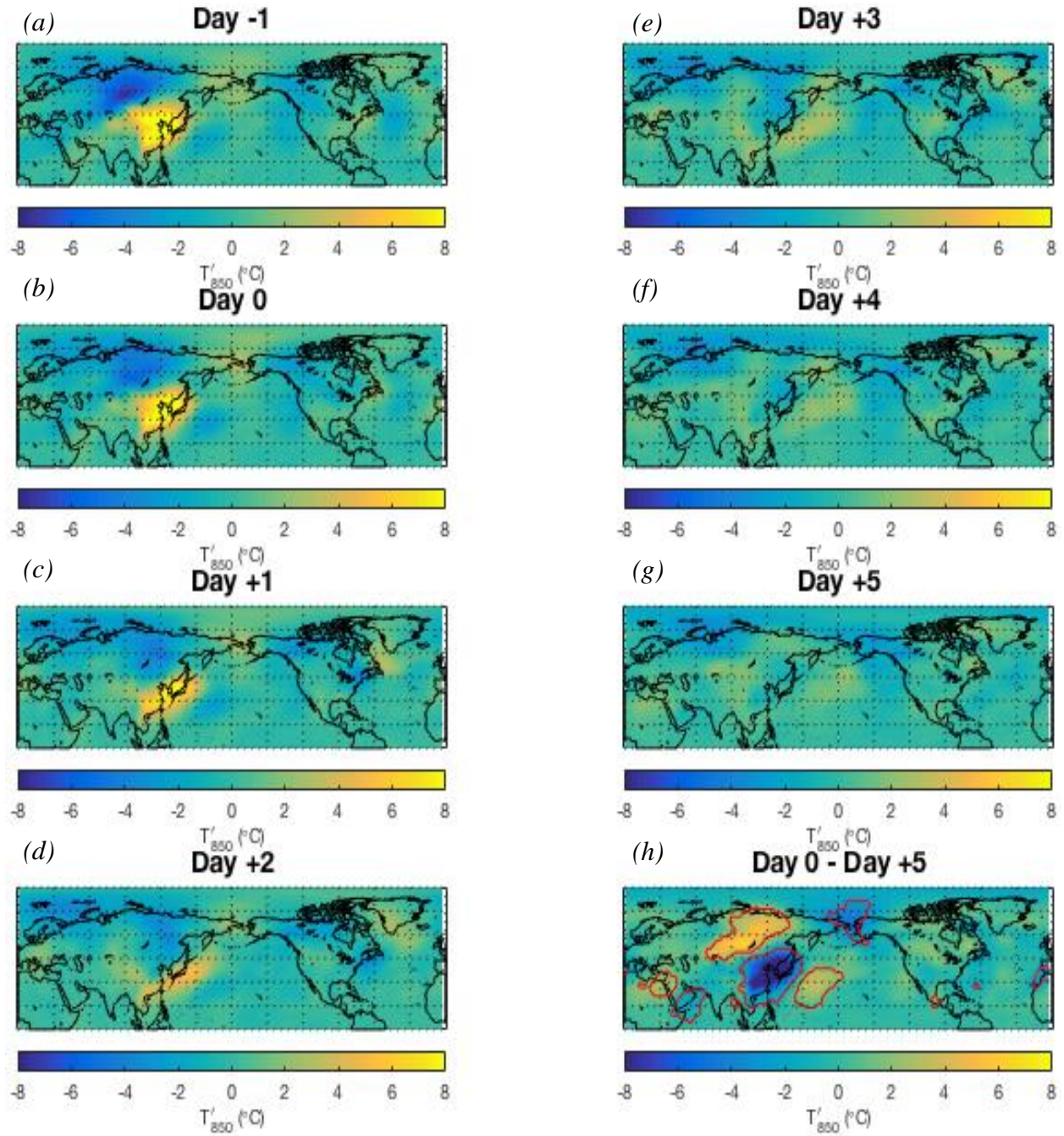


Figure 50: As for Fig. 44, but for composite of 850-hPa temperature anomalies.

	HCP	SMH	CI
Mean	0.0061	0.0024	-1.61x10 ⁻¹²
Max	3.5662	4.6047	3.4148
Min	-3.5228	-1.9500	-4.0965
Range	7.0890	6.5547	7.5114

Table 1: Statistical data distribution of daily standardized anomalies for all three daily indices (HCP, SMH, CI) from Nov. 1948 – Mar. 2013.

	HCP	SMH	CI
Mean	0.008143	0.003768	0.0003952
Max	0.8676	0.7904	0.5448
Min	-1.0080	-0.4536	-0.6994
Range	1.875	1.244	1.244
σ	0.3434	0.2529	0.2689

Table 2: Statistical data distribution of seasonal averaged standardized anomalies for all three daily indices (HCP, SMH, CI) from Nov. 1948 – Mar. 2013 (65 winter seasons).

Expansive HCP	Strong SMH	Cold Seasons	Contracted HCP	Weak SMH	Warm Seasons
50-51	52-53	50-51	98-88	72-73	98-99
56-57	54-55	55-56	01-02	78-79	01-02
74-75	56-57	56-57	06-07	06-07	06-07
76-77	76-77	69-70	08-09		
		76-77			

Table 3: (a) List of extremely strong EAWM (+1.5 σ) seasons for all three indices (HCP, SMH, CI) as seen from the seasonal averaged time series. (b) List of extremely weak EAWM (-1.5 σ) seasons for all three indices (HCP, SMH, CI) as seen from the seasonal averaged time series.

	R
CI & SMH	-0.4164
CI & HCP	-0.5113
SMH & HCP	0.4618

Table 4: Correlation coefficients of daily standardized anomalies for all three indices (HCP, SMH, CI) (significant at the 99% confidence level) from Nov. 1948 – Mar. 2013.

1.5σ Cold Events \geq 4 Days (Date)	Length of Event	Max $\Sigma T'_{850}$
01/09-01/12, 1951	4 days	-808.406
02/28-03/03, 1951	4 days	-1119.172
02/16-02/22, 1952	7 days	-667.261
12/09-12/14, 1954	6 days	-642.524
01/06-01/09, 1956	4 days	-907.83
02/08-02/12, 1957	5 days	-951.638
02/20-02/24, 1964	5 days	-629.676
02/10-02/14, 1967	5 days	-600.051
12/06-12/10, 1967	5 days	-735.069
02/04-02/09, 1968	6 days	-591.109
02/20-02/24, 1969	5 days	-612.277
03/15-03/19, 1970	5 days	-613.255
02/23-02/26, 1974	4 days	-910.781
12/09-12/15, 1975	7 days	-743.064
11/11-11/15, 1976	5 days	-713.956
12/25-12/30, 1976	6 days	-791.353
01/27-01/30, 1977	4 days	-681.462
02/12-02/16, 1978	5 days	-654.046
01/29-02/01, 1980	4 days	-768.669
02/03-02/08, 1980	6 days	-781.475
11/05-11/08, 1981	4 days	-845.409
12/21-12/24, 1984	4 days	-777.81
12/07-12/10, 1985	4 days	-565.79
02/26-03/01, 1986	4 days	-736.657
11/28-12/01, 1987	4 days	-725.236
03/02-03/07, 1988	6 days	-788.962
11/20-11/23, 1993	4 days	-625.147
02/17-02/21, 1996	5 days	-687.151
11/14-11/20, 2009	7 days	-782.365

Table 5: List of 1.5 σ cold events lasting \geq 4 days. First, second, and third column list their date, length of event, and maximum CI index value, respectively. Highlighted in light blue are the events that had the longest duration of 7 days. Highlighted in dark blue is the event that had the most maximum CI index value (coldest day).

Length of 1.5σ Cold Events	Frequency of Events
4 Days	12
5 Days	9
6 Days	5
7 Days	3

Table 6: Frequency of 1.5 σ cold events lasting \geq 4 days.

1.5σ Warm Events \geq 4 days (Date)	Length of Event	Max $\Sigma T'$
01/27-02/02, 1949	7	717.748
01/14-01/18, 1950	5	610.279
02/23-02/26, 1954	4	607.29
03/21-03/24, 1958	4	556.195
03/05-03/10, 1960	6	582.73
12/24-12/27, 1962	4	627.235
02/27-03/03, 1966	5	661.302
01/23-01/27, 1967	5	646.431
11/21-11/25, 1968	5	583.473
12/03-12/09, 1968	7	738.204
01/14-01/17, 1971	4	622.416
02/10-02/13, 1976	4	529.958
01/05-01/09, 1979	5	713.796
11/16-11/19, 1980	4	553.189
02/07-02/10, 1987	4	736.025
12/23-12/28, 1987	6	873.713
01/05-01/08, 1989	4	543.845
11/13-11/18, 1990	6	647.366
12/23-12/30, 1996	8	625.404
03/08-03/12, 1997	5	577.934
02/15-02/19, 1998	5	484.56
11/12-11/15, 1998	4	630.102
12/16-12/22, 1998	7	689.264
01/22-01/25, 1999	4	648.495
02/17-02/21, 2001	5	616.162
01/09-01/15, 2002	7	804.069
02/17-02/20, 2004	4	770.443
02/03-02/08, 2007	6	572.713
02/25-03/02, 2007	6	535.266
01/29-02/13, 2009	16	865.396
03/16-03/21, 2009	6	738.877
02/22-02/27, 2010	6	765.071
01/28-01/31, 2013	4	714.691
03/05-03/08, 2013	4	930.904

Table 7: List of 1.5 σ warm events lasting \geq 4 days. First, second, and third column list their date, length of event, and maximum CI index value, respectively. Highlighted in light red is the event that had the longest duration of 16 days. Highlighted in dark red is the event that had the most maximum CI index value (warmest day).

Length of 1.5σ Warm Events	Frequency of Events
4 Days	13
5 Days	8
6 Days	7
7 Days	4
8 Days	1
16 Days	1

Table 8: Frequency of 1.5 σ warm events lasting \geq 4 days.